



Overview article

# High entropy alloys: A focused review of mechanical properties and deformation mechanisms<sup>☆</sup>



E.P. George<sup>a,b</sup>, W.A. Curtin<sup>c</sup>, C.C. Tasan<sup>d,\*</sup>

<sup>a</sup> Oak Ridge National Laboratory, Materials Science and Technology Division, Oak Ridge, TN 37831-6115, USA

<sup>b</sup> Department of Materials Science and Engineering, University of Tennessee, Knoxville, TN 37996-2100, USA

<sup>c</sup> Laboratory for Multiscale Mechanics Modeling, Ecole Polytechnique Fédérale de Lausanne, Lausanne CH-1015, Switzerland

<sup>d</sup> Department of Materials Science and Engineering, Massachusetts Institute of Technology, 77 Massachusetts Avenue, Cambridge, MA 02139, USA

---

## ARTICLE INFO

### Article history:

Received 20 May 2019

Revised 3 December 2019

Accepted 5 December 2019

Available online 9 December 2019

---

### Keywords:

Solid solution

Solute strengthening

Ductility

Microstructure design

Plasticity mechanisms

## ABSTRACT

The high-entropy alloy (HEA) concept was based on the idea that high mixing entropy can promote formation of stable single-phase microstructures. During the past 15 years, various alloy systems have been explored to identify HEA systems with improved property combinations, leading to an extraordinary growth of this field. In the large pool of alloys with varying characteristics, the first single-phase HEA with good tensile properties, the equiatomic CrMnFeCoNi alloy has become the benchmark material, and it forms the basis of much of our current fundamental understanding of HEA mechanical behavior. As the field is evolving to the more broadly defined complex concentrated alloys (CCAs) and the available data in the literature increase exponentially, a fundamental question remains unchanged: how *special* are these new materials? In the first part of this review, select mechanical properties of HEAs and CCAs are compared with those of conventional engineering alloys. This task is difficult because of the limited tensile data available for HEAs and CCAs. Additionally, the wider suite of mechanical properties needed to assess structural materials is woefully lacking. Nonetheless, our evaluations have not revealed many HEAs or CCAs with properties far exceeding those of conventional engineering alloys, although specific alloys can show notable enhancements in specific properties. Consequently, it is reasonable to first approach the understanding of HEAs and CCAs through the assessment of how the well-established deformation mechanisms in conventional alloys operate or are modified in the presence of the high local complexity of the HEAs and CCAs. The second part of the paper provides a detailed review of the deformation mechanisms of HEAs with the FCC and BCC structures. For the former, we chose the CrMnFeCoNi (Cantor) alloy because it is the alloy on which the most rigorous and thorough investigations have been performed and, for the latter, we chose the TiZrHfNbTa (Senkov) alloy because this is one of the few refractory HEAs that exhibits any tensile ductility at room temperature. As expected, our review shows that the fundamental deformation mechanisms in these systems, and their dependence on basic physical properties, are broadly similar to those of conventional FCC and BCC metals. The third part of this review examines the theoretical and modeling efforts to date that seek to provide either qualitative or quantitative understanding of the mechanical performance of FCC and BCC HEAs. Since experiments reveal no fundamentally new mechanisms of deformation, this section starts with an overview of modeling perspectives and fundamental considerations. The review then turns to the evolution of modeling and predictions as compared to recent experiments, highlighting both successes and limitations. Finally, in spite of some significant successes, important directions for further theory development are discussed. Overall, while the individual deformation mechanisms or properties of the HEAs and CCAs are not, by and large, “special” relative to conventional alloys, the present *HEA rush* remains valuable because the compositional freedom that comes from the multi-element space will allow exploration of whether *multiple* mechanisms can oper-

---

<sup>☆</sup> NOTICE OF COPYRIGHT This manuscript has been co-authored by UT-Battelle, LLC under Contract No. DE-AC05-00OR22725 with the U.S. Department of Energy. The United States Government retains and the publisher, by accepting the article for publication, acknowledges that the United States Government retains a non-exclusive, paid-up, irrevocable, worldwide license to publish or reproduce the published form of this manuscript, or allow others to do so, for United States Government purposes. The Department of Energy will provide public access to these results of federally sponsored research in accordance with the DOE Public Access Plan <http://energy.gov/downloads/doe-public-access-plan>.

\* Corresponding author.

E-mail address: [tasan@mit.edu](mailto:tasan@mit.edu) (C.C. Tasan).

ate sequentially or simultaneously, which may yet lead to the creation of new alloys with a spectrum of mechanical properties that are significantly superior to those of current engineering alloys.

© 2019 Acta Materialia Inc. Published by Elsevier Ltd. All rights reserved.

## 1. Introduction

The HEA concept has created an enormous, worldwide drive for alloy design, one that is unprecedented in the history of metallurgical research. Soon after the introduction of the original concept which proposed that maximizing configurational entropy can favor the formation of stable, single-phase, substitutional solid solutions, research focusing on alloys that violate the founding principles started to appear. Development of non-equiautomatic HEAs, multi-phase HEAs, metastable HEAs, HEAs with interstitial alloying elements, medium-entropy alloys (MEAs) and other variations have led to the broader family of complex concentrated alloys (CCAs). The vast increase in the degrees of freedom arising from the multi-component, alloy-system-independent, and evolving definition of CCAs has led the alloy design community to explore numerous strategies in the search for interesting mechanical properties. At the same time, the large amount of data has made it more difficult to develop broad conclusions regarding the mechanical benefits of increasing compositional complexity. As stated by Miracle and Senkov in a recent review [1]: “*Direct comparison of data is difficult, due to differences in the type and concentration of principal elements, the type and extent of thermo-mechanical processing, and the temperature and duration of post-process thermal treatment*”.

In this focused review, we attempt to carefully study the noisy mechanical property data in the literature to determine if/where HEAs or CCAs exhibit unique property benefits. The assessment of their uniqueness is critical especially for the development of rigorously derived mechanistic theories with strong predictive capabilities. If these alloys are different compared to standard engineering alloys, then we have little theoretical basis on which to build understanding and we have to start from scratch with entirely new ideas. Such a start would benefit from “correlation” approaches that are presently abundant in the literature, which take what can be measured/estimated or observed (e.g., dislocation behavior, atomic displacements, elastic constants, stacking fault energies, twinning) and correlate these features with macroscopic measurements such as strength or ductility. Some of these approaches may lack predictive capability, but can suggest mechanisms, and can be useful for alloy design or for providing guidelines for new theories to be developed. On the other hand, if these alloys are not fundamentally different, and the deformation mechanisms therein are similar to those in existing engineering alloys, then we have the entire edifice of prior metallurgical knowledge to build upon.

## 2. Experimental findings

### 2.1. Mechanical properties

In order to provide a focused, systematic overview of the mechanical response of HEAs and CCAs, first, a comparative assessment of their uniaxial deformation behavior will be presented, with respect to classical structural alloys. Note that if any generic conclusions can be drawn regarding the mechanical response of HEAs and CCAs, it will have to be from the results of uniaxial tension/compression experiments, due to the limited data available for other loading conditions. In fact, only few fracture toughness [2–5] and fatigue resistance [6–9] investigations of HEAs and CCAs have been carried out, focusing on, e.g., CoCrFeMnNi, MoNbTaW,

AlCoCrFeNi alloys. To this end, we collected uniaxial mechanical properties at ambient and elevated temperatures from relevant reports published prior to January 2019 [3–5,10–190,191]. The data for uniaxial tension at room temperature are shown in Fig. 1a, where the strengths plotted are the maximum (ultimate) values and the elongations are total elongations (not uniform elongations). Data for uniaxial compression are shown in Fig. 1b. In both figures, the strengths plotted are the maximum (ultimate) values. Each symbol represents a particular phase or mixture of phases, for which the data were obtained from various references as detailed separately in Supp. Table 1. To carry out more systematic comparisons and identify the outliers, the data in Fig. 1 are further classified based on alloy constituents and compared to competing standard alloys in Fig. 2. Finally, the mechanical behavior of HEAs at higher temperatures is presented in Fig. 3.

In the literature, such strength - ductility plots are often used to compare alloys of similar composition and applications (e.g., automotive steels [192–194]). In the case of HEAs and CCAs, however, besides the aforementioned challenge associated with their broad definition, two characteristics further complicate such comparisons: (i) Due to their compositional complexity, these alloys are likely to exhibit nano-scale intermetallics, precipitates or short-range ordering, which are experimentally challenging to identify, unless systematic transmission electron microscopy or atom probe tomography experiments are carried out. Given the uncertainty rising from the absence of such analyses, it is not always possible to rule out contributions of mechanisms other than compositional complexity, to properties reported in HEAs and CCAs investigations. (ii) In contrast to classical structural metals, extensive microstructural optimization studies (e.g., grain size refinement, fine-tuning of phase fractions, or morphologies) have not been carried out for most HEAs and CCAs. Thus, it is likely that the reported properties represent lower bounds. We note that from a practical perspective, attention should also be paid to the density of these HEAs, which Gorsse et al. have nicely addressed in an earlier review [195].

Despite the limitations stated above, some general observations can be made from Fig. 1a. First, it is difficult based on these data to propose that HEAs and CCAs exhibit tensile strength or ductility that go beyond those of classical structural alloys. The observed mechanical properties are well within those observed in martensitic steels, advanced high strength steels, nickel-based alloys, etc. Of course, considering the limitation (ii) above, it could be that superior properties will be achieved upon further optimization. Second, the HEAs and CCAs cover nearly the entire property spectrum of steels, aluminum, titanium, magnesium and nickel alloys. This point is a demonstration of the scope of this field, and the broadness of the CCA definition. Third, the high ductility low strength side of Fig. 1a is as heavily occupied by HEAs and CCAs as the high strength low ductility side. This observation is important, since at earlier stages of HEA research, low tensile ductility was common and often only compressive properties were reported.

At first glance, the compressive properties in Fig. 1b display a different trend compared to the tensile properties in Fig. 1a. While the majority of the data lies within the ultimate compressive strength of 1000–2300 MPa and strain of 0.1%–15%, many of the surveyed HEAs display significantly improved compressive properties compared with conventional engineering alloys. For example, the  $\text{Al}_{0.3}\text{CoCrFeNi}$  HEA is reported to exhibit compressive strain of 97% and compressive strength of 1378 MPa, which was

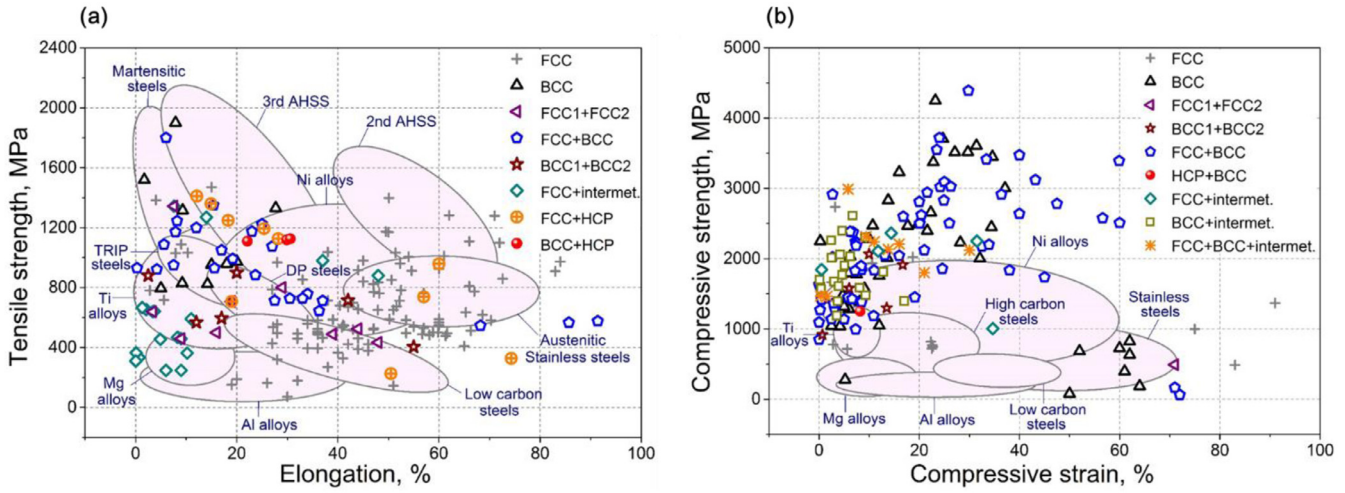


**Fig. 1.** Room-temperature tensile strength vs elongation to fracture (a) and compressive strength vs compressive strain (b) of HEAs and CCAs reported in literature. See Supp. Table 1 for detailed information about data sources. 2nd and 3rd AHSS stand for the two generations of advanced high-strength steels, DP steels for dual-phase steels and TRIP steels for transformation-induced plasticity steels.

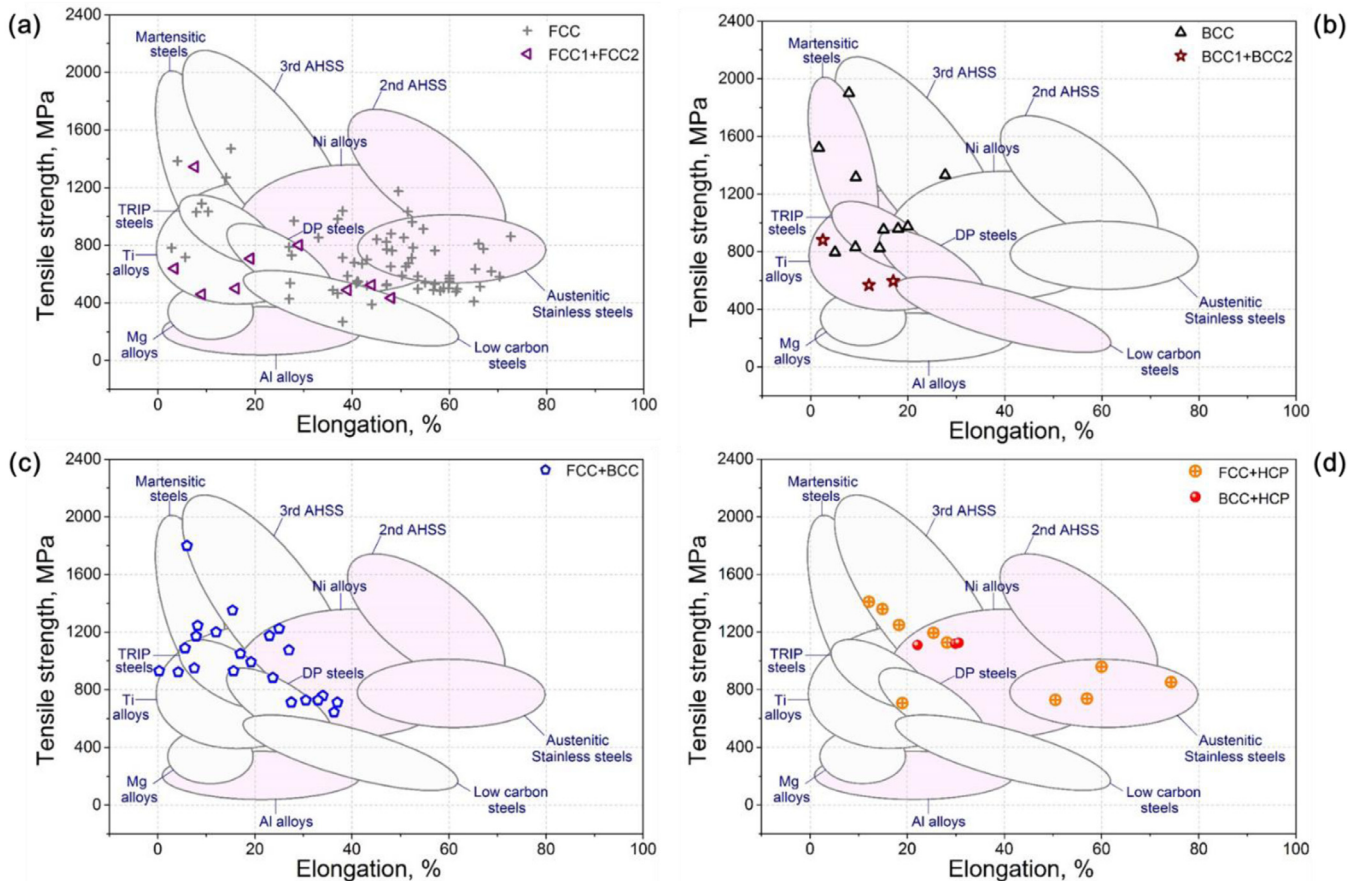


**Fig. 2.** Room-temperature uniaxial tension test data of HEAs and CCAs from Fig. 1a, classified based on phases present in the microstructure: (a) FCC, FCC1+FCC2, (b) BCC, BCC1+BCC2, (c) FCC+BCC, (d) FCC+HCP. 2nd and 3rd AHSS stand for the two generations of advanced high-strength steels.

attributed to the activation of mechanical twinning [49]; and very high compressive strength of 4390 MPa was achieved in a dual phase AlCoCrFeNi HEA at ambient temperature [143]. However, several points are worth keeping in mind when considering data from compression experiments. Compression samples that have initial aspect ratios of 2:1 and are deformed beyond 50% strain will be constrained by the platens, thereby artificially inflating the measured strength (because 45° slip is blocked). While it is pos-

sible to increase the constraint-free strain by increasing the aspect ratio, it needs to stay below the buckling threshold. Barreling due to friction between the sample and platen can also artificially increase the measured strength. Additionally, in many samples (i.e., most FCC alloys), fracture simply cannot be reached in compression tests. In fact, even brittle metals can display significant plastic strain in compression in the absence of a driving force for mode I crack extension. This makes it difficult to evaluate from

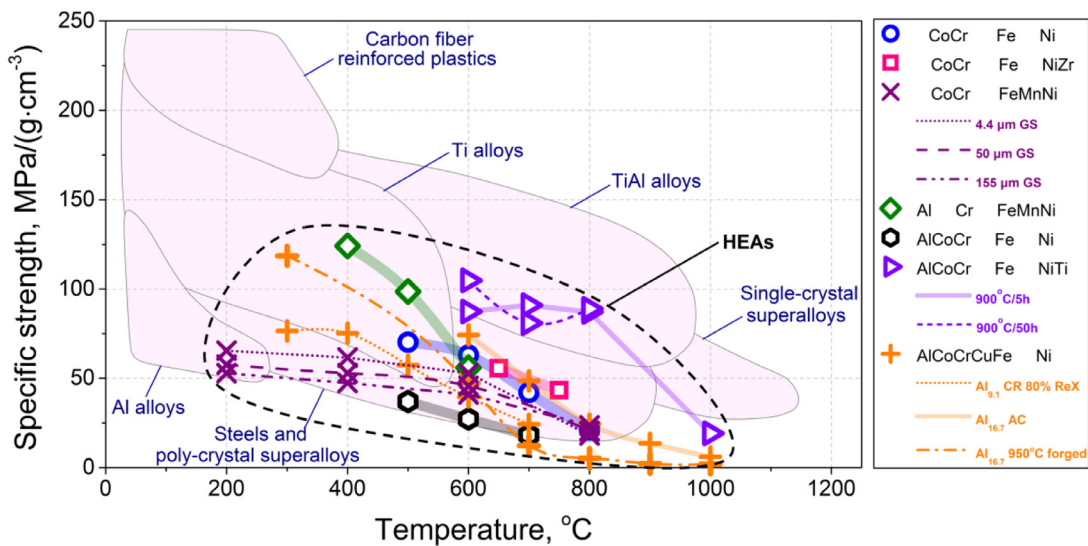


**Fig. 3.** Specific strength vs. temperature of HEA and CCA's reported in literature, shown with respect to conventional high temperature materials.

compression test results (Fig. 1b) whether the classic strength–ductility trade-off will be seen when any given alloy is tested in tension. Finally, we would also like to note that tensile data are typically not provided for these alloys tested in compression. It may thus be speculated that the limitation (i) stated above could be influencing the results here, since the existence of intermetallic compounds within both the single BCC phase and the FCC+BCC dual phase HEAs would explain increases beyond the compressive strengths of standard structural alloys, and absence of tensile ductility. Given these uncertainties, it is difficult to justify the use of data obtained in compression to claim that the properties of HEAs and CCAs are somehow unique.

Comparing tensile properties of HEAs and CCAs with standard alloys of similar phase constitution (Fig. 2) reveals similar tendencies as those presented in Fig. 1a. As can be seen in Fig. 2a most of the *single FCC phase* HEAs show comparable properties to Ni-based alloys or austenitic stainless steels, which typically have similar (3d late transition) alloying elements. Compared to 2nd generation advanced high strength steels (2nd AHSS), most single FCC phase HEAs have lower ultimate tensile strengths. HEAs whose properties are comparable to 2nd AHSS benefit from either twinning-induced plasticity (TWIP) effects or the inclusion of interstitial elements. For example, the equiatomic CoCrNi medium entropy alloy (MEA) shows an ultimate tensile strength of 890 MPa and 73% elongation with the formation of deformation twins [196]. This alloy has significantly large latent hardening effect comparable to conventional TWIP steels. This large hardening effect was suggested to be the consequence of unique nanoscale twin/hcp lamellae introduced during deformation in the CoCrNi MEA [95]. Seol et al. [92] reported the significantly improved tensile properties of FeMnCoCrNi (920 MPa, 52%), FeMnCoCr (880 MPa, 73%) HEAs by doping several tens ppm of B. The improvement is attributed to the segregation of B at the grain boundaries, which results in grain size reduction and interface strengthening. FeMnCoCrNi HEA with C also showed significant increase in the ultimate tensile strength (810 MPa) and elongation (66 %) [102]. It seems that typical effects of interstitial carbon in austenitic steels—interstitial solid solution strengthening, increasing stacking fault energy— are also realized in this HEA.

Next, we consider HEAs and CCAs that develop *BCC based microstructures* (Fig. 2b). The single BCC phase alloys, which mostly consist of refractory elements, exhibit properties similar to TRIP steels and DP steels. Although BCC based HEAs and CCAs are often considered for high-temperature applications, comparisons of their

properties to BCC-containing automotive steels are instructive. For example, as reported by Juan et al. [170], an equiatomic HfNbTaTiZr alloy possess an ultimate tensile strength of 974 MPa while maintaining 20% elongation at ambient temperature. It should be noted that this kind of single BCC phase HEA displayed almost negligible work hardening capability (yield strength: 958 MPa) – a characteristic significantly different from TRIP or DP steels. One obvious difference in the microstructures of the latter is the numerous inter-phase boundaries that impede dislocation motion, which likely accounts for their higher strain hardening capability when compared to the single-phase BCC alloy that has to rely on just Taylor type hardening. An alloy that exhibited clearly outlying properties at room temperature is oxygen doped TiZrHfNb HEA (1300 MPa, 30%) [197]. Strong ordered-oxygen complexes were reported in this alloy, which contributed to the promotion of dislocation multiplication for higher strength and ductility. Typically, interstitial elements in refractory alloys significantly decrease their ductility. However, this work identified an unexpected beneficial effect of interstitial oxygen when present in the form of nanoscale ordered complexes. This may provide an additional mechanism to enhance the strength and ductility of refractory HEAs.

Present *dual-phase* HEAs or CCAs also rarely outperform standard alloys (Fig. 2c). Most of the FCC+BCC dual phase HEAs show properties that are similar to TRIP and DP steels, while Wani et al. [151] reported that by applying cold rolling to an AlCoCeFeNi<sub>2.1</sub> eutectic HEA, its tensile strength can be improved up to 1800 MPa, while preserving an elongation of 6%, which although impressive is comparable to conventional martensitic steels and the 3rd generation AHSS. The strength enhancement was attributed to the refined nano-lamellar microstructure produced by cold rolling. FCC+HCP dual phase HEAs exhibit a wide range of properties (Fig. 2d). The presence of intermetallic compounds divides the properties of FCC HEAs into two group. One group displays relatively low strength and elongation. A typical example is the Al<sub>10</sub>Co<sub>25</sub>Cr<sub>8</sub>Fe<sub>15</sub>Ni<sub>36</sub>Ti<sub>6</sub> HEA heat treated at 700 °C for 5 h which possessed a tensile strength of 365 MPa and an elongation of 0.9% at ambient temperature. By combining thermodynamic calculations and XRD analyzes, Daoud et al. [198] proposed that this sort of embrittlement mostly resulted from the formation of Cr-C-rich intermetallic compounds at grain boundaries. In contrast, the properties of the second group, namely FCC+HCP alloys, range from those of the 3rd generation AHSS to austenitic stainless steels: Stepanov et al. [180] reported that by optimizing the thermo-mechanical

treatment parameters for a 1 at. % C-doped CoCrFeNiMn HEA, broad variation of properties can be achieved. Based on the EBSD and TEM analyzes, it was recognized that the spatial distribution of  $M_{23}C_6$ -type intermetallic compounds played a key role in the corresponding tensile properties. Li et al. [199] developed a  $Fe_{50}Mn_{30}Co_{10}Cr_{10}$  dual-phase HEA where extensive work hardenability was achieved (YS: 328 MPa, UTS: 851 MPa) through the martensitic transformation of the FCC phase upon plastic deformation. Ductility of the HEA is abnormally high (74.3%) for FCC+HCP materials and several studies suggest unique deformation and damage mechanisms of HCP phase in  $Fe_{50}Mn_{30}Co_{10}Cr_{10}$  dual-phase HEA [200,201].

Next we consider temperature effects on the strength of HEAs and CCAs, since many alloy-design efforts target use at high temperatures. Fig. 3 presents the specific strengths at elevated temperatures and compares them to conventional engineering alloys [352,353] (See also Supp. Table 2). A major caveat here is that, HEAs and CCAs having high melting points (e.g., refractory HEAs) are not included. They were recently thoroughly reviewed by Senkov et al. [202]) and have the potential for high temperature applications beyond nickel-base superalloys. The data plotted are thus for Cantor alloy variations, such as CoCrFeNi [110], CoCrFeNiZr [68], CoCrFeMnNi [43], AlCrFeMnNi [67], AlCoCrFeNiTi [115], and AlCoCrCuFeNi [203] alloys. In general, the specific strengths of the surveyed HEAs all drop significantly at temperatures above 600 °C, Fig. 3. The simultaneous alloying of Al and Ti with short-term annealing treatment creates an exception, and gives rise to the best specific strength values, comparable to the high performance steels and polycrystalline superalloys. However, the addition of Al, Cu, and Ni does not contribute to a significant strength enhancement.

To conclude this section, it is worth making a few points about comparisons such as those in Figs. 1 and 2. (i) While the property envelopes of the various conventional alloys are relatively robust, given their long history of development and commercial deployment, the outlines sketched for the HEAs and CCAs should be viewed as mere snapshots in time of a subset of mechanical properties that will undoubtedly evolve as the field progresses. (ii) To generate plots such as these, one has to first choose a classification scheme for the alloys. In the case of conventional alloys, composition (or the principal element) is a natural way to separate, say, Ti alloys from Ni alloys, but in HEAs/CCAs with multiple principal elements, this is not practicable. An alternative approach, which is what we chose here, is to classify based on the crystal structures of the main phases present in the HEAs/CCAs. However, this makes it difficult to discern differences between alloys with the same crystal structure but with different compositions. (iii) Probably the biggest drawback of such plots is that most aspects of 'microstructure' are not accounted for. Strength and ductility are influenced strongly by microstructure and the data reported in the literature for the different alloys are for different microstructural states. Grain size is an influential factor and varies across the different HEAs/CCAs in these figures. The volume fractions, sizes, morphologies and distributions of phases in dual-phase HEAs and precipitate-strengthened CCAs are similarly important and not controlled for in these plots; nor or the interstitial contents and distributions, twin volume fractions and sizes, and strains at which TWIP and TRIP effects are activated. We suspect this unfortunate situation that we find ourselves in will remain so for a while because of its inherent 'chicken and egg' nature. On the one hand there is a need to scan (relatively quickly) the vast compositional space of HEAs to find potentially interesting alloys. On the other hand, to determine whether mechanical properties are truly exceptional requires fairly in-depth studies of a variety of properties (yield strength, ultimate strength, uniform elongation, total elongation, fracture toughness, fatigue limit, fatigue crack growth resistance, etc., which are important to vary-

ing degrees in different applications). However, to motivate such in-depth studies, researchers first need to see that there is the potential for at least some unique properties, which of course requires some in-depth studies where microstructure is carefully controlled. The reported room-temperature strengths and ductilities of HEAs and CCAs are not suggestive of a special, universal effect leading to superior properties compared to standard engineering alloys. The over-performing examples in the literature are those whose properties cannot be attributed merely to 'HEA effects,' namely, lattice distortion and substitutional solid solution strengthening due to the presence of multiple principal elements. Rather, they also benefit from other effects including TRIP, TWIP, short-range ordering, interstitial solid solution strengthening, and precipitation hardening all of which exist to varying degrees in conventional alloys. This, however, should not be taken as a message to demotivate research on HEAs and CCAs. On the contrary, although these effects have been widely utilized in other alloys, HEAs and CCAs provide a unique advantage in that they offer a vast compositional space in which the different mechanisms may be tuned and optimized more effectively (with more degrees of freedom) to develop new alloys with superior properties.

The plots in Figs. 1–3 also ignore behavior at cryogenic temperatures where the CrMnFeCoNi alloy first grabbed the field's attention because it exhibited simultaneous increases in strength and ductility with decreasing temperature [208] combined with exceptional fracture toughness [2]. Consequently, it is now the most extensively investigated and best understood HEA, as will be presently shown. In time, we hope that other HEAs/CCAs will be thoroughly investigated so that the full suite of mechanical properties can be evaluated against those of existing alloys instead of just ultimate strength and total elongation as we have been able to do in this section.

## 2.2. Deformation mechanisms

### 2.2.1. FCC-based HEAs

The assessment carried out in Section 2.1 suggests that mechanical behavior (strength and ductility) of HEAs and CCAs is similar to standard engineering alloys. To further check the validity of this assessment, it is required to zoom-in, and evaluate available experimental data regarding mechanical properties in conjunction with the observations on deformation micro-mechanisms. We first start with FCC-based HEAs, for which there is significantly more data in the literature.

*Yielding behavior. Solid solution effects:* Pure FCC metals show practically no temperature dependence of yield strength between 500 and 77 K [204]. In contrast, as shown in Fig. 4, the FCC Cantor alloy (CrMnFeCoNi) exhibits relatively strong temperature dependence of yield strength with almost a factor of four increase as the temperature is decreased from 500 to 77 K for the coarsest grain size material. While this behavior is different from that of pure FCC metals, it is by no means unique if we consider the broad swath of FCC alloys. The yield strengths of even binary FCC solid solutions [204–208] are known to be temperature dependent to varying degrees, depending on the constituent elements and their concentrations. For example, 70-30 Brass (Cu-Zn) exhibits a similar fourfold strength increase over the same temperature range [209], albeit with lower absolute strengths overall, while less concentrated Cu-Al alloys exhibit a somewhat smaller temperature dependence [210].

An obvious question is whether the temperature dependence of yield strength is caused by an anomalously strong temperature dependence of the shear modulus. At least in the case of the Cantor alloy, that is not the case since its shear modulus shows a fairly weak temperature dependence between 77 and 500 K [213,214]. Similar, weak temperature dependences of shear moduli

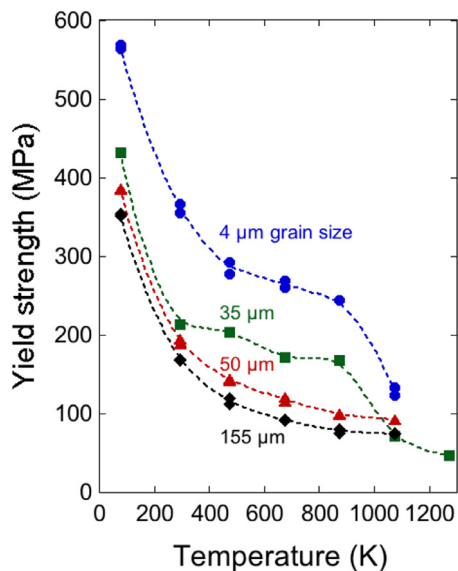


**Fig. 4.** Temperature and grain size dependence of the yield strength of the CrMnFeCoNi high-entropy alloy. Adapted from [211,212].

were also found in several medium-entropy equiatomic subsets of the Cantor alloy [215], several of which nevertheless show strong temperature-dependent yield strengths [43]. In fact, the temperature dependence of yield strength persists even after normalization by the shear modulus [215] indicating that the temperature dependence of the shear modulus is not the major reason for the observed behavior.

Rather, the thermally activated behavior appears to reflect “standard” solid solution strengthening driven by volume misfit [216]. However, unlike in simple solid solutions (e.g., dilute binaries), it is not straightforward to calculate volume misfits in equiatomic high-entropy alloys where there are no solvents or solutes in the traditional sense. In dilute binaries, the increase in lattice parameter with increasing solute concentration has long served as a useful proxy for volume misfit [217]. Alternatively, the Goldschmidt radii of the constituent (pure) elements have been used to estimate the resulting misfits in the alloy [218]. However, in complex (concentrated) solid solutions, including high-entropy alloys, the “effective” radii of the constituent elements in the alloy are significantly different from their pure-element radii [154] and it is not straightforward to convert the lattice parameters of different high-entropy alloys to corresponding differences in volume misfits of the constituent atoms. Therefore, to determine their contributions to solid solution strengthening, first-principles calculations are needed to compute the interaction energies of individual solutes with dislocations [219]. Further details of this approach are provided later.

It is often asserted that high-entropy alloys are expected to be stronger than conventional alloys (or alloys with fewer elements) because of enhanced solid solution strengthening from the large number of constituent elements [220]. Our survey, Figs. 1–3, suggests otherwise, however, it needs to be further tested by examining true single-phase solid solutions, which avoid confounding effects of second phases that can contribute to strength through other mechanisms. In addition, the alloys being compared should all have the same crystal structure and their relevant microstructural features (grain size, stored dislocation density, etc.) should be similar. The first study [211] that met these criteria showed that increasing the number of elements from four in CrFeCoNi to five in CrMnFeCoNi did not change the yield strength significantly. Subsequently, a more detailed study [43] examined all the single-phase FCC subsets (quaternary, ternary, binary, and unary) of the Can-

tor alloy. The alloys were thermomechanically processed to have roughly the same grain size. Fig. 5 shows the temperature dependence of the 0.2% offset yield strengths of these alloys along with that of pure Ni. Clearly, strength does not increase monotonically with the number of alloying elements (i.e., configurational entropy). For example, the ternary alloy CrCoNi has the highest strength, higher than the quinary Cantor alloy (CrMnFeCoNi) and all three quaternary alloys (FeNiCoCr, NiCoCrMn, and FeNiCoMn). Alloys with the same number of elements had significantly different strengths: FeNiCoCr is much stronger than FeNiCoMn, CrCoNi is much stronger than MnFeNi and FeNi is much stronger than NiCo. In other words, strength is not determined by the sheer number of alloying elements; rather the type of element matters. Sometimes higher strength can be obtained by adding fewer, *but the right kind of*, elements.

The obvious question then is: which characteristics of an alloying element matter? Extrapolating from what we know about traditional solid solution theories, the volume misfit of an alloying element is likely to be important. However, as discussed earlier, quantifying this is easier said than done in concentrated equiatomic alloys. One way [219] to treat the problem is to consider an “effective medium” that has all the macroscopic (average) properties of the alloy of interest (elastic modulus, lattice parameter, etc.). The interaction energy between a dislocation and individual solutes placed at various locations in this medium can then be determined from first principles and used to calculate the stress needed to move dislocations (yield stress). This procedure is described in Section 3, and good agreement has been obtained between the theoretical predictions and the experimentally measured yield strengths shown in Fig. 5 without the need for any fitting parameters.

Given the importance of volume misfit, a related question is: how can its effects be measured experimentally? If all the atoms have the same size, their centers will coincide with the ideal lattice points. However, if there are size differences, the atoms will tend to be displaced from the ideal positions. In dilute solid solutions, only the atoms near the solute are significantly displaced; however, in a high-entropy alloy, all atoms are displaced to different degrees. From single crystal X-ray diffraction experiments, a quantity called the atomic displacement parameter (ADP) can be determined [154]. It is the sum of the squares of the constituent atoms from their mean (equilibrium) positions due to both thermal vibrations (resulting in dynamic disorder) and the static displacement of the mean positions from the ideal lattice points (resulting in static disorder, which is related to size misfit). As the temperature is decreased, the ADP is dominated more and more by static disorder. For the Cantor alloy, values for the ADP at 25 and 300 K were found to be approximately 24 and 59 pm<sup>2</sup>, respectively [154]. Given the complexity of the 5-element alloy, displacements of each element could not be determined individually (the above are average values for the whole alloy). However, from first principles calculations [154], the mean square atomic displacement (MSAD) of each element in the Cantor could be individually calculated and averaged to obtain a value of ~25 pm<sup>2</sup> for the MSAD of the alloy, which agreed well with the experimental ADP value of ~24 pm<sup>2</sup>. Similar computations were carried out [154] for the ternary and quaternary FCC subsets of the Cantor alloy and it was found that the degree to which an atom is displaced from its ideal lattice position depends on its neighborhood, that is, on which other elements are present in the alloy. Thus, the MSAD of say, Cr, in the quaternary alloy CrMnFeNi is significantly higher (by ~64%) than in another quaternary alloy CrFeCoNi [154] where the only difference is that Co is present instead of Mn while the remaining three elements are the same. Similar effects are seen in the other single-phase FCC subsets of the Cantor alloy. In general, the atoms with larger effective radii tend to

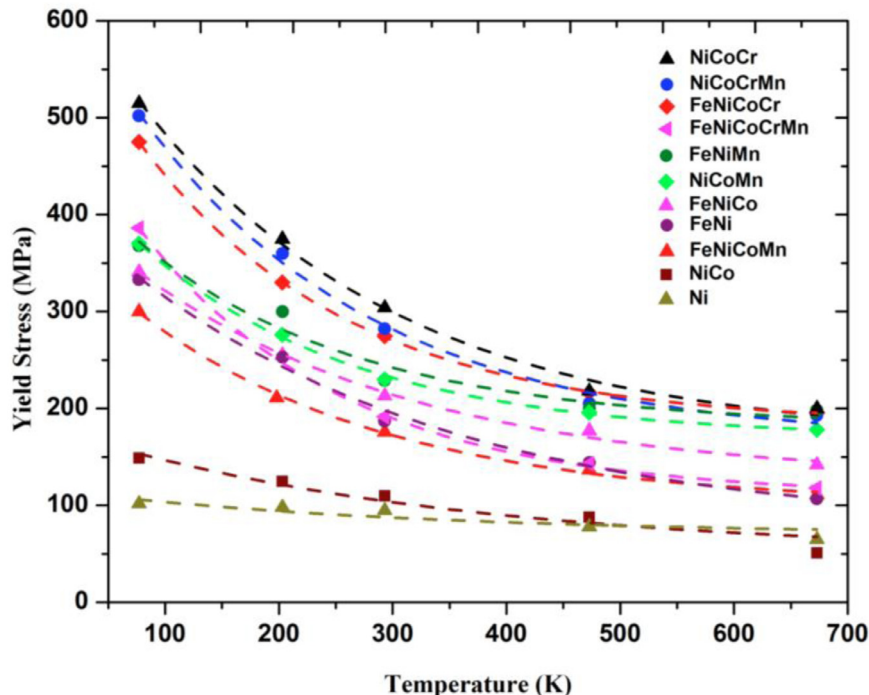


**Fig. 5.** Temperature dependence of the yield strength of the CrMnFeCoNi high-entropy alloy and all its FCC medium-entropy and low-entropy equiatomic subsets [43].

displace the smaller atoms significantly with the latter tending to be distributed among the larger atoms to better accommodate the displacements. These results provide insight into why certain elements (such as Cr with the largest effective radius) have a bigger effect on strengthening and why simply adding more elements may not always be the most effective approach. As will be shown later, the shear-modulus-normalized yield strengths of the Cantor alloy and its MEA subsets correlate well with the square root of the MSAD, which lends credence to the notion that solid solution strengthening scales with the displacements of atoms from their ideal lattice positions, which in turn is expected to depend on their volume misfits in the alloy. However, a deeper insight into the underlying forces arising from these misfits can only be obtained from more detailed first principles calculations, as discussed later.

**Grain size effects:** Initially, the effect of grain refinement (Hall-Petch effect) was investigated by room-temperature Vickers microhardness measurements [221] and the Hall-Petch slope of the Cantor alloy was found to be higher than the upper bound of the Hall-Petch slopes of FCC metals [222], suggesting a possibly higher slip-transfer resistance at grain boundaries in the compositionally complex high-entropy alloy. However, Vickers hardness measurements convolute yield and flow behaviors (up to ~7% plastic strain), which complicates interpretation of the results; additionally, these hardness measurements were made only at room temperature and information about other temperatures was lacking. Tensile tests were subsequently performed to study the Hall-Petch behavior of the yield stress of the Cantor alloy as a function of temperature for grain sizes of ~4–155  $\mu\text{m}$  [212]. Those Hall-Petch slopes were found to range from ~530 to ~420 MPa  $\mu\text{m}^{-1/2}$  for temperatures of 77 to 873 K (i.e., decreasing by about 20% with increasing temperature in this range). At room temperature, the Hall-Petch slope of the Cantor alloy was determined to be 494 MPa  $\mu\text{m}^{-1/2}$ , which is higher than that of pure FCC metals, namely, 90–230 MPa  $\mu\text{m}^{-1/2}$  [222]. Recently, these Hall-Petch data were extended to smaller grain sizes (~0.5–89  $\mu\text{m}$ ) using yield strengths measured in tension at room temperature [71] and the Hall-Petch slope was found to be 490 MPa  $\mu\text{m}^{-1/2}$ , which is

essentially identical to the value measured in the earlier study [212]. Subsequent hardness measurements made on the quaternary and lower-order FCC subsets of the Cantor alloy showed that their Hall-Petch slopes were lower than that of the Cantor alloy [223], but additional data from tensile tests are needed to clarify the effects of alloy composition and number of alloying elements on grain-boundary strengthening. Small additions (as little as 30 ppm) of an interstitial element, boron, to the Cantor alloy (as well as its non-equiatomic quaternary subset) were found to both retard grain growth and increase strength for a given grain size [92]. It accomplished this by segregating to the grain boundaries. Based on the limited data available to date, it appears that the bulk alloy composition and grain-boundary segregation can affect slip-transfer resistance; however, additional work is warranted to improve understanding of the underlying mechanisms.

**Critical resolved shear stress:** Single-crystal yield stresses have become available only within the last two to three years. For the Cantor alloy, the first compression tests on bulk single crystals [224] yielded a value for the critical resolved shear stress (CRSS) of 70 MPa at room temperature and 175 MPa at 77 K. These values are significantly higher than those (~51 and 117 MPa, respectively) deduced from the polycrystalline yield stresses of large-grained material [212] divided by the Taylor factor (~3). Since the bulk single crystals were produced by the Bridgman technique, possible reasons for the higher CRSS include deviation from the equiatomic composition [225] and impurity contamination from the crucible used for crystal growth. Subsequently, single-crystal micropillars were machined by focused ion beam milling from individual grains of a polycrystalline sheet and compressed using a nanoindenter [154]. Two different orientations,  $[\bar{1}26]$  and  $[\bar{1}23]$ , were tested using several pillars in the size range 1–10  $\mu\text{m}$ . There was no orientation dependence of the CRSS (i.e., Schmid law was valid), but a “smaller is stronger” size effect was seen with a power-law exponent near the lower bound for FCC metals indicative of a high friction stress (similar to the reasoning behind why FCC metals in general have larger exponents than BCC metals [226]). By extrapolating the yield stress curves of the small (1–10  $\mu\text{m}$ ) pillars to

**Table 1**

Critical resolved shear stress (CRSS) for slip nucleation in single crystals of single-phase HEAs with the FCC structure.

Alloy	Loading	Temperature	CRSS (MPa)	Reference
CrMnFeCoNi	Tension	RT	53–60	[227]
CrMnFeCoNi	Tension	RT	63	[228]
CrMnFeCoNi	Tension	RT	70	[224]
CrMnFeCoNi	Tension	RT	78–82	[225]
CrMnFeCoNi	Tension	RT	82	[229]
CrMnFeCoNi	Compression <sup>1</sup>	RT	33–43	[154]
CrMnFeCoNi	Tension	77 K	135	[228]
CrMnFeCoNi	Tension	77 K	155	[229]
CrMnFeCoNi	Tension	77 K	145–172	[227]
CrMnFeCoNi	Tension	77 K	175	[224]
CrMnFeCoNi	Tension	203 K	103	[229]
CrMnFeCoNi	Tension	243 K	92	[229]
CrMnFeCoNi	Tension	423 K	59	[229]
CrFeCoNi	Tension	RT	42	[226]
CrFeCoNi	Compression	RT	39–43	[226]
CrFeCoNi	Tension	77 K	99	[226]
CrFeCoNi	Compression	77 K	89–98	[226]
CrFeCoNi	Tension	77 K	141	[230]
CrCoNi	Tension	RT	69	[231]
CrFeCoNiAl <sub>0.3</sub>	Tension	RT	76	[232]
CrFeCoNiAl <sub>0.3</sub>	Tension	RT	80	[233]
CrFeCoNiAl <sub>0.3</sub>	Compression	RT	54	[234]
CrFeCoNiAl <sub>0.3</sub>	Tension	77 K	170	[233]
CrFeCoNiAl <sub>0.3</sub>	Compression	93 K	129	[234]

larger sizes (20–30  $\mu\text{m}$ ), a “bulk” CRSS of 33–43 MPa was estimated for the Cantor alloy [154], which is in line with what can be inferred from the polycrystalline yield stress [212] divided by the Taylor factor. More recently, Bridgeman single crystals having orientations of [001], [123], and [111] were tested in tension at room temperature [225]. As in the case of the earlier micropillar compression specimens, there was no orientation dependence of the CRSS, which was determined to be ~80 MPa. This value of CRSS is similar to that determined previously from compression tests on a bulk Bridgeman single crystal [224], indicating a lack of tension-compression asymmetry in addition to a lack of orientation dependence.

A bulk single crystal of a quaternary alloy, CrFeCoNi, which is an FCC subset of the Cantor alloy, was grown by floating zone directional solidification and its CRSS was determined to be ~41 and ~96 MPa at room temperature and 77 K, respectively [226]. Similar to the Cantor alloy, this quaternary, too, did not exhibit any orientation dependence or tension-compression asymmetry. Furthermore, the CRSS of the quaternary alloy CrFeCoNi [226] is similar to that of the quinary alloy CrMnFeCoNi [154], consistent with their similar polycrystalline yield stresses [211]. Therefore, the significantly higher CRSS values of the Cantor alloy in [224,225,229] may well be the result of inadvertent deviations from the target composition as mentioned earlier. Table 1 summarizes CRSS values for the FCC high- and medium-entropy alloys that have been determined to date.

RT: Room temperature. <sup>1</sup>From micropillar data extrapolated to large (20–30  $\mu\text{m}$ ) pillar sizes to estimate “bulk” CRSS.

Compared to pure FCC Ni, whose CRSS at room temperature is 3–4 MPa [235], the CRSS of the Cantor alloy is at least an order of magnitude higher. Such a relatively high solid solution strengthening has been rationalized as follows [154]. Assuming that the “solvent” is the atom with the largest calculated effective radius and the “solute” the one with smallest radius, the maximum pair-wise difference between the constituent elements of the Cantor alloy is found to be ~4% between Cr and Co (or Fe, which has a similar effective radius as Co). Then, using the Labusch model [236], a hypothetical equiatomic binary with this size difference was found to have a shear-modulus-normalized critical resolved shear stress

(CRSS) that is comparable to the lower bound of the experimentally measured CRSS [154]. A more fundamental theory of solid solution strengthening, discussed in the next section, is in fact able to account for the strengthening observed in not just the Cantor alloy but also in all its lower-order FCC subsets.

**Activation volumes:** The activation volume of the Cantor alloy at yielding, measured in load relaxation tests [100], is  $\sim 60 b^3$  at 77 K and  $\sim 360 b^3$  at room temperature. These values are higher than those of individual point defects ( $\sim b^3$ ) but lower than those due to collective solute fluctuations in dilute solid solutions ( $\sim 1000 b^3$ ), where  $b$  is the magnitude of the Burgers vector. As discussed in the next section, the measured activation volumes are in reasonably good agreement with those calculated using a recent theory of solid solution strengthening [237], especially at low temperatures, suggesting that this is the mechanism responsible for initial yielding, similar to the behavior of more dilute FCC solid solutions.

**Strain rate effects:** At quasi-static strain rates ( $10^{-1}$ – $10^{-5} \text{ s}^{-1}$ ), there is a relatively weak effect of strain rate on the tensile yield strength of the Cantor alloy for grain sizes of  $\sim 35 \mu\text{m}$  [211] (or, for that matter, on the subsequent flow behavior). This is typical of FCC metals and alloys [209] and consistent with the larger room-temperature activation volumes associated with solid solution hardening effects (few hundreds of  $b^3$ ) than with kink-pair formation on screws (few tens of  $b^3$ ); the related dislocation core effects then lead to strong strain rate effects in this regime in BCC metals [209]. At a higher (intermediate) strain rate of  $100 \text{ s}^{-1}$ , a recent study has shown that both yield and flow stresses are significantly enhanced. For Cantor alloy specimens with a grain size of  $\sim 10 \mu\text{m}$ , the tensile yield strength increased by ~35% from 484 to 650 MPa when the strain rate was increased from  $10^{-3}$  to  $100 \text{ s}^{-1}$  with a corresponding increase of the ultimate tensile strength from 853 to 968 MPa [238]. Additionally, the total elongation was higher at the higher strain rate, but the uniform elongation was lower. Investigations at still higher (dynamic) strain rates approaching  $\sim 5000 \text{ s}^{-1}$  have only been performed in compression using the split Hopkinson bar technique. For the Cantor alloy at room temperature, yield strength increased by ~85% from  $\sim 325$  to 360 MPa at strain rates of  $10^{-4}$  to  $10^{-2} \text{ s}^{-1}$  to  $\sim 590$ –680 MPa at strain rates of 3000–4700  $\text{s}^{-1}$  [239]. The strong rate dependence under dynamic conditions has been ascribed to viscous phonon drag effects [239], which contrasts with the modest rate dependence observed under quasi-static conditions resulting from solid solution hardening [211]. Other studies on CrMnFeCoNi [161], CrFeCoNi [240], Al<sub>0.1</sub>CrFeCoNi [241], and Al<sub>0.3</sub>CrFeCoNi [242] under dynamic conditions have also reported increases in the yield strength at high strain rates.

**Flow behavior. Polycrystalline alloys:** Representative engineering stress-strain curves of the CrMnFeCoNi alloy in tension at different temperatures are shown in Fig. 6 for 50  $\mu\text{m}$  grain size. When the grain size is varied, the flow stresses increase with decreasing grain size ( $\sim 150$ –5  $\mu\text{m}$ ) except at high temperatures (e.g., 800 °C) where the small (~5  $\mu\text{m}$ ) grain size material exhibits strain softening shortly after yield, presumably due to grain-boundary deformation mechanisms as in other materials. The yield stress, flow stress and uniform elongation all increase as the temperature is decreased down to liquid nitrogen temperature (Fig. 6). The increase in ductility with decreasing temperature (despite the increasing yield strength) is due to postponement of the onset of necking instability, which in turn is due to high, steady, work hardening that persists to higher strains at lower temperatures [211].

The early stage of plastic deformation in CrMnFeCoNi is characterized by planar slip of  $\frac{1}{2}\langle 110 \rangle$  dislocations on {111} planes at temperatures in the range 77–873 K [212]. After deformation, foils cut parallel to the activated {111} planes and examined by transmission electron microscopy (TEM), showed long, smoothly curved dislocation with no discernible preferred orientation [154].

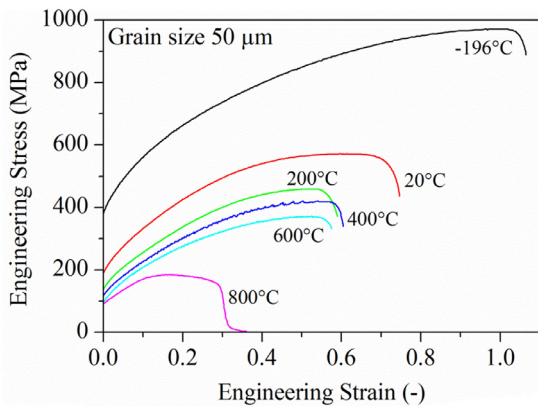


**Fig. 6.** Representative stress–strain curves of the CrMnFeCoNi high-entropy alloy [212].

This suggests that there is likely no major difference in the mobilities of edge and screw segments, consistent with the previously mentioned lack of both orientation dependence of CRSS and tension-compression asymmetry. Extended pile-ups of the dislocations against grain boundaries are often seen [212]. Some of the dislocations are split into  $1/6<112>$  Shockley partials bounding stacking faults [154,243] while others remain as full (undissociated)  $1/2<110>$  dislocations [212].

In situ observations in a TEM straining stage [244] suggest that the mobility of the full dislocations is low and their motion extremely sluggish; the partials in contrast move very quickly but are arrested when they intersect a band of slow-moving full dislocations. These observations must be treated with caution because the shear stress acting on the dislocations during in situ straining is not known, that is, any apparent differences in mobility might be due to differences in the local stress driving dislocation motion. From the separation of the Shockley partials imaged using weak-beam dark-field TEM, the stacking fault energy of the Cantor alloy was estimated to be  $\sim 30 \text{ mJ m}^{-2}$  [154]. On the other hand, from experimentally determined x-ray stacking fault probabilities, stacking fault energies of  $18\text{--}27 \text{ mJ m}^{-2}$  were estimated for the Cantor alloy, which are somewhat lower than the value obtained from the partial separations [136]. First principles calculations of the stacking fault energy taking into account chemical, magnetic and strain contributions yielded a value of  $21 \text{ mJ m}^{-2}$  for the Cantor alloy at room temperature [245]. Given the experimental errors of the TEM and x-ray measurements and the approximations required for the calculations, these values may be considered in reasonably good agreement. High-resolution TEM observations show that the separation between partials in the Cantor alloy is highly variable (by a factor of two) at different points along the dislocation [246]. Calculations suggest that this may be due to variations in the local composition, which affects the local stacking fault energy and thus the partial separation [246]. However, it must be noted that large local variations in partial separations have also been seen in pure metals and dilute alloys [247–249], so it is unclear to what extent HEAs are unique. In principle such local variations can affect the behavior of dislocations (e.g., by changing the activation barrier for cross-slip), but additional work is needed to determine how the overall alloy composition affects such local behavior and how such local fluctuations can be integrated into a theory that can calculate alloying effects on strength.

First principles calculations of stacking fault energy have also been performed as a function of temperature and it was found that, for the Cantor alloy, it decreases dramatically to  $\sim 3.4 \text{ mJ m}^{-2}$  at 0 K [245]; a later investigation reported that it actually becomes negative at 0 K [250]. Since lower stacking fault energies enhance

twinability [251,252], these results are consistent with the experimental observation (discussed later) that the Cantor alloy tends to twin more readily as the temperature is decreased. Furthermore, since the introduction of a stacking fault changes the local stacking sequence from FCC to HCP, the calculations suggest that the Cantor alloy might undergo a phase transformation from FCC to HCP at low temperatures. Consistent with such an expectation, an FCC to HCP transformation was predicted below room temperature [253] in another first principles study of the Cantor alloy. To date, there has been no confirmation of a thermally induced HCP transformation in the Cantor alloy; however, a pressure-induced FCC to HCP transformation has been reported [254,255].

Shockley partial separations in a related FCC alloy, FeCoNiCrAl<sub>0.1</sub>, have been measured by TEM and a stacking fault energy of  $\sim 30 \text{ mJ m}^{-2}$  was estimated [56], although a later study [89] reported a much lower stacking fault energy of  $\sim 12 \text{ mJ m}^{-2}$  for the same alloy. The reason for this discrepancy is not clear and further studies are warranted. Table 2 summarizes the stacking fault energies of various FCC high-and medium-entropy alloys.

Considering all the evidence available to date, it can be concluded that the yield and (early stage) flow behavior of various single-phase, FCC, high- and medium-entropy alloys are similar to those of FCC metals and alloys. Planar slip occurs by the movement of  $1/2<110>$  dislocations on {111} planes. Dissociation of these dislocations into the usual  $1/6<112>$  Shockley partials is often observed. The CRSS for yielding does not depend on crystal orientation and is the same in tension and as in compression (i.e., Schmid's law is valid). Consistent with this, the dislocations lying within the {111} planes are long and smoothly curved without any preference for screw or edge character. The degree of solid solution strengthening depends on the type of element added, not how many elements are added. This is because different elements produce different volume misfits, which depend not just on the element being added but also on which other elements are present in the alloy. Consequently, pure-element radii cannot be used to predict lattice distortions (displacements). In the literature, “severe” lattice distortion is often invoked as the reason for the strong solid solution strengthening in HEAs, without quantifying what “severe” means (as discussed above, the average atomic displacement in the Cantor alloy is less than 5 picometers). A proper accounting of the effects of different alloying elements requires a quantitative theory of solid solution hardening, which is discussed later. We now address the later stages of flow and the different mechanisms of strain hardening that can be activated and their effects on strength and ductility.

**Twinning-induced plasticity (TWIP):** In metals that exhibit hardening only due to dislocation-dislocation interactions (e.g., Taylor hardening), the strain hardening rate generally decreases continuously until the Considère criterion is reached and necking instability sets in followed in short order by fracture. Fig. 7 shows an example of this for the Cantor alloy at room temperature (red curve). To remove the effects of the temperature dependence of the shear modulus, the strain hardening rates at the two temperatures have been normalized by the shear modulus.

Examination by TEM of specimens extracted from tensile tests interrupted after different amounts of strain [212,243] showed that the dislocation substructure evolves from planar slip at small strains to cross-slipped tangled dislocations at intermediate strains and cell structures at high strains (Fig. 8), similar to the microstructure evolution seen in most FCC metals. The increase in dislocation density with strain was measured by TEM and the results are shown in Fig. 9. As seen in this figure, the increase in dislocation density is essentially the same at 77 K as it is at room temperature, consistent with the temperature-independent work hardening rate of FCC metals at low strains [209]. This means that

**Table 2**

Experimentally determined stacking fault energy (SFE) in single-phase HEAs with the FCC structure.

Alloy	Method	SFE (mJ m <sup>-2</sup> )	Reference
CrMnFeCoNi	X-ray diffraction line broadening	18–27	[106]
CrMnFeCoNi	Partial separations by TEM	25–35	[154]
CrFeCoNi	X-ray diffraction line broadening	17–32	[106]
CrFeCoNi	Partial separations by TEM	23–31	[256]
CrCoNi	Partial separations by TEM	18–26	[257]
CrCoNi	Partial separations by TEM	14–22	[256]
CrFeCoNiAl <sub>0.1</sub>	Partial separations by TEM	26–34	[56]

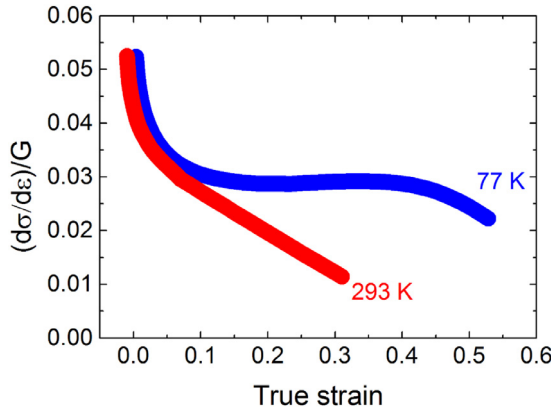


**Fig. 7.** Shear modulus normalized true strain hardening rate as a function of true strain for the CrMnFeCoNi high-entropy alloy [243]. (For interpretation of the references to color in this figure, the reader is referred to the web version of this article.)

if Taylor hardening is the only operative mechanism, the shear-modulus-normalized work hardening rate as a function of strain should be identical at both these temperatures (since it depends only on the square-root of dislocation density and a couple of other constants that are independent of strain). However, the work hardening rates at room temperature and 77 K are distinctly different (Fig. 7), with a clear divergence beyond ~6% plastic strain. Therefore, another mechanism must be operating at 77 K besides simple dislocation hardening.

That mechanism is deformation-induced twinning, which starts to appear sporadically, in some grains, after about 6% strain (Fig. 10) and consistently in all grains examined, after about 9% strain (Fig. 11). The nanoscale twins are of the normal kind seen in FCC metals [212,258] and contribute to hardening as previously reported in other materials [259,260]. With increasing strain, their

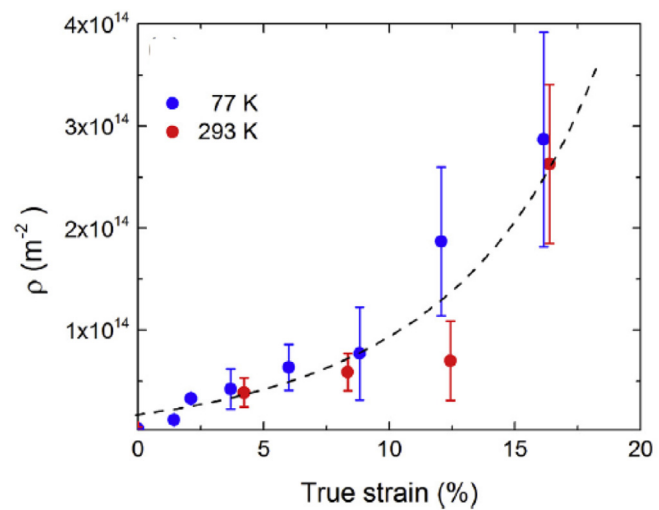


**Fig. 9.** Increase in dislocation density with strain in the CrMnFeCoNi high-entropy alloy at 77 K and room temperature [243].

thickness and volume fraction increase [243]. It has been suggested [261–263] that mechanical twins contribute to strengthening by dividing the grains into progressively smaller grains (the so-called dynamic Hall-Petch effect). This deformation-induced twinning provides a source of high, sustained work hardening that postpones the onset of necking instability to higher strains [211,212]. As a result, the TWIP effect is able to increase both strength and ductility simultaneously. Certain twin boundaries act as barriers to dislocation motion, while others allow partial dislocations to glide along the twin-matrix interfaces [264] thereby presumably relieving some of the accumulated stresses and enabling further deformation.

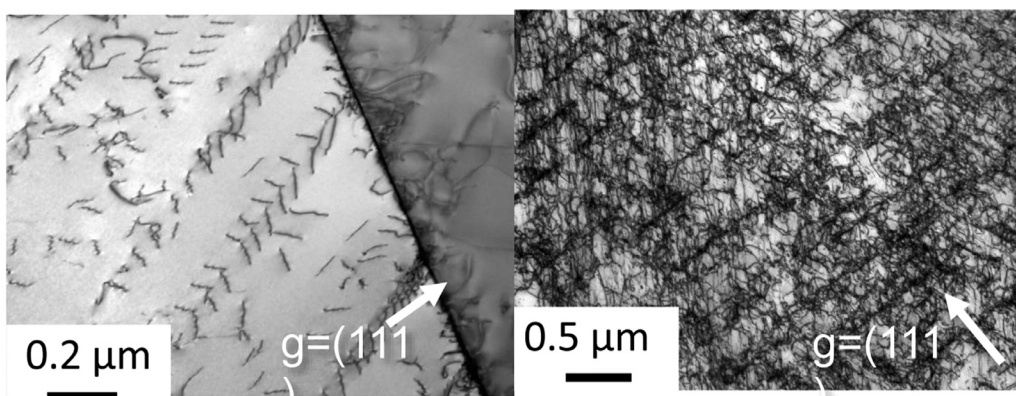


**Fig. 8.** Planar dislocation arrays on {111} planes in the CrMnFeCoNi high-entropy alloy at low strains, ~5% true strain at 77 K (left) and tangled dislocations forming cell structures at high strains, ~22% true strain at room temperature (right) [243].

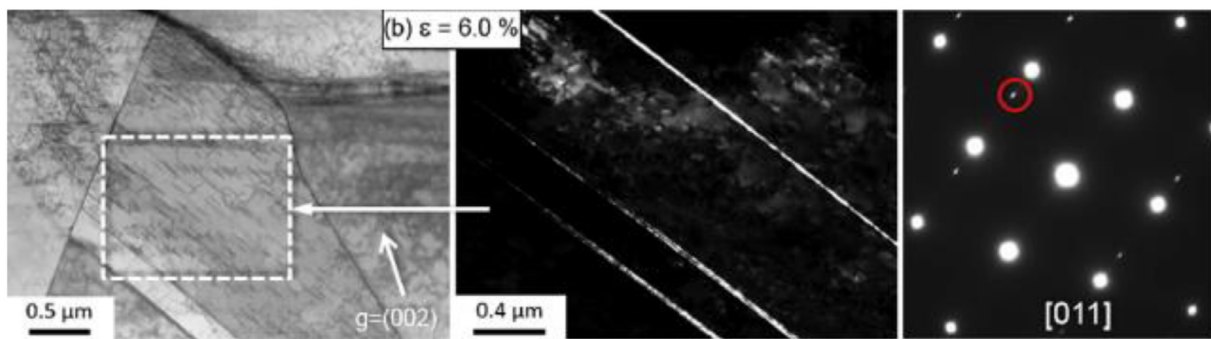


**Fig. 10.** Bright field TEM image (left) dark field image (middle) and selected area diffraction pattern (right) showing sporadic twining in a CrMnFeCoNi high-entropy alloy strained to 6% at 77 K [243].

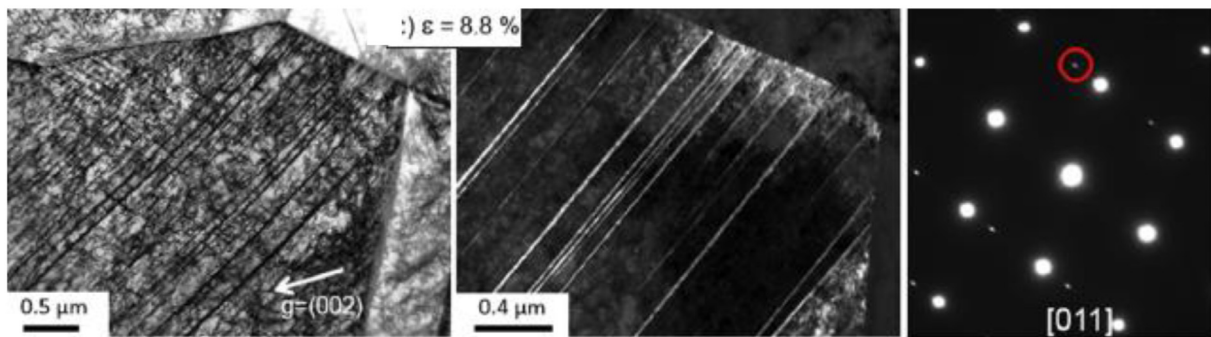


**Fig. 11.** Bright field TEM image (left) dark field image (middle) and selected area diffraction pattern (right) showing profuse twining in a CrMnFeCoNi high-entropy alloy strained to ~9% at 77 K [243].

A critical stress for twinning is thought to exist in FCC metals, which depends weakly, if at all, on temperature [265]. Assuming that is the case in the Cantor alloy, one would also expect twinning at room temperature if the internal stress is able to rise sufficiently. The axial stress at which twins appear at 77 K is ~720 MPa [243]. At room temperature such a high stress is reached only close to fracture. Specimens subjected to axial stresses of 680 and 820 MPa were examined by TEM. The former showed no evidence of twinning while twins were clearly visible in the latter [243]. In other studies, room-temperature twinning has been observed in the Cantor alloy after rolling [266] and high-pressure torsion [101], both of which are expected to produce high internal stresses, although their magnitudes are not known. Taken together, these results are consistent with the view that there is a critical stress for twinning that is roughly temperature independent. Another factor that is known to affect twinning is grain size: the likelihood of deformation induced twinning is reduced as the grain size is decreased [265,267]. This has been confirmed in the Cantor alloy where twinning was found to occur at grain sizes above about 3 μm but not at an ultrafine grain size of ~500 nm [268]. Consistent with this, twinning was observed during in situ straining in a TEM at room temperature, in the crack-bridging ligaments behind the crack-tip [244], presumably because of the lack of constraint in this very thin electron-transparent section of the foil.

Another factor that is known to affect “twinability” is stacking fault energy [251,252]. The experimentally determined stacking fault energy of the ternary equiatomic alloy CrCoNi is ~22 mJ m<sup>-2</sup> [257], which is approximately 25% lower than that (~30 mJ m<sup>-2</sup>) measured for CrMnFeCoNi [219]. Consistent with this, the former twins more easily both at room temperature and at 77 K [257]. Partly as a result of this, the CrCoNi alloy exhibits better strength and ductility [43] as well as fracture toughness [2] than the CrMnFeCoNi alloy [2,211,212]. However, not the entire difference can be

ascribed to stacking fault energy because the CrCoNi alloy also has a higher yield strength, which allows it to reach the critical twinning stress earlier (during straining) compared to the CrMnFeCoNi alloy [257].

**Single-crystal alloys:** The flow behavior of HEA single crystals has only recently begun to be investigated. Within the last two years, a few studies of the quinary CrMnFeCoNi alloy [224,225,227–229,269] have been published. Limited work has also been performed on Al0.3CoCrFeNi [232,234] and the quaternary alloy CrFeCoNi [226]. Nevertheless, our current basic understanding of flow behavior relies almost exclusively on the results of the CrMnFeCoNi alloy, and that is what we will focus on here. Abuzaid and Sehitoglu [227] performed tensile tests at room temperature and 77 K on <111>, <149>, <122> and <123> oriented single crystals of the CrMnFeCoNi alloy grown by the Bridgman technique. Digital image correlation (DIC) was used to measure surface strains and identify slip traces; electron back scattered diffraction (EBSD) was used to determine crystal orientations. Reference images were taken before loading and compared with images taken after different amounts of applied strain. Since both DIC and EBSD require relatively damage-free surfaces, the tensile tests had to be periodically stopped and the specimens re-polished before the tests could be continued. This produced some artifacts where the unloading-reloading segments had to be stitched together (because of changes in specimen geometry), but they are not expected to significantly affect the broad conclusions of that study.

Fig. 12 shows the stress-strain curve of a <111> specimen tested at room temperature, along with DIC contour plots as insets where slip traces (bands) parallel to  $(\bar{1}11)$  can be seen. The first appearance of these bands was at an axial stress of 170 MPa, from which the authors calculated a CRSS of 53 MPa, assuming that slip occurred on the slip system,  $(\bar{1}11)[\bar{1}\bar{1}0]$ , with the highest Schmid factor. This CRSS is comparable to that mentioned earlier in the

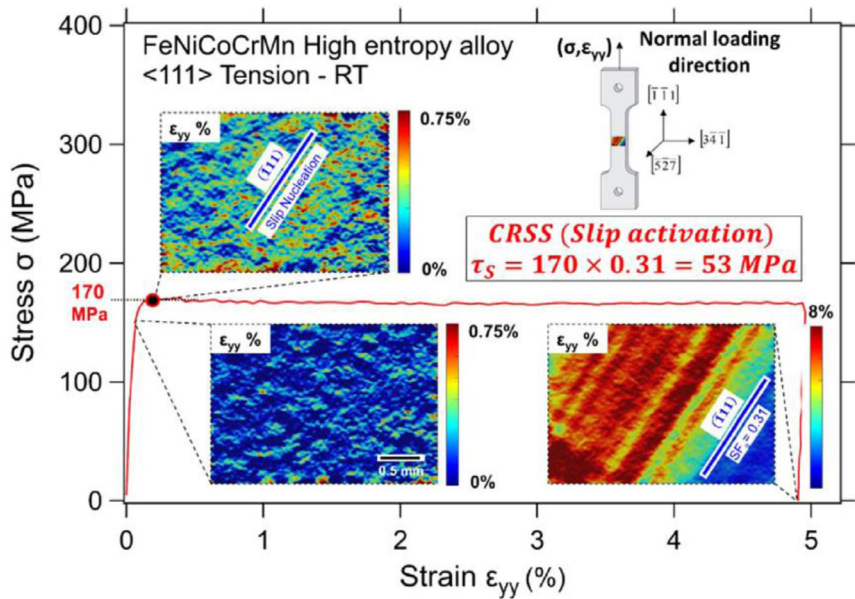


**Fig. 12.** Tensile stress–strain response at room temperature of <111> single crystal of CrMnFeCoNi alloy [227]. Insets show normal strains obtained *in situ* during loading as DIC contour plots.

section on polycrystalline yield strengths, but is lower than that measured in some other single crystal studies [224,225] where it was speculated that deviations from the aim composition may be responsible for the higher CRSS [225]. After yielding, plastic flow continued on the primary system by easy glide with very low work hardening until strains of ~20% (this corresponds to stage I in typical FCC metals). Subsequently, multiple slip was activated (stage II) with traces parallel to (111) appearing on the specimen surface. Slip on these intersecting planes likely produced dislocation interactions and cross-slip that resulted in some of the slip traces becoming curved. Because of these slip interactions, the work hardening rate ( $\frac{\partial \sigma}{\partial \epsilon}$ ) in stage II increased substantially. As in most other FCC single crystals, the extent of stage I is drastically curtailed (sometimes to the point of extinction) when multiple slip systems are activated early on in the deformation process [225,229]. Correspondingly, TEM images showed extensive planar dislocation arrays and pile-ups in specimens deforming principally by single slip and dislocation tangles when multiple slip systems were activated [225].

At room temperature, even after applied strains of ~40% where the axial stresses reached ~720 MPa, Abuzaid and Sehitoglu [227] found no indication of twinning, at least as discernable by EBSD or DIC, possibly because these techniques lack the resolution needed to detect small volume fractions of twins. Another study [225] of the same CrMnFeCoNi alloy utilized TEM instead and found clear evidence of twinning, consistent with the notion that higher resolution techniques are needed for their detection. In a tensile specimen oriented for multiple slip, twins appeared after a strain of about 5% and their density increased with increasing deformation, whereas in a specimen oriented initially for single slip significantly more dislocation activity had to occur before twinning commenced at a strain of about 27%. In yet another multiple-slip orientation, [001], twinning was not observed, likely because the stress on the twinning system never reached a high enough value. The measured work hardening rates were consistent with how the microstructure (dislocations and twins) evolved with strain. In general, the activation of twinning led to noticeably increased work hardening rates, similar to that seen in polycrystalline CrMnFeCoNi [243]. From their single crystal experiments, Kireeva et al. [225] estimated a CRSS for twinning of ~110–140 MPa at room tempera-

ture. This value is significantly lower than the value (~235 MPa) estimated from the polycrystalline twinning stress divided by the Taylor factor [243]. There are several possible reasons for this discrepancy. Twinning in polycrystalline HEAs is known to depend on the orientations of the grains relative to the loading axis [270], because of the different resolved shear stresses in the different grains. Given the small sample size of the thinned region of a TEM foil and because only some of the grains in the gage section twin, it would be easy to miss the twinned grains (at least in the early stage). Twinning is also known to become more difficult as the grain size decreases [265] which may account for its occurrence at lower stresses in single crystals than in polycrystals. Finally, Kireeva et al. [225] speculated that, since the composition of their single crystal deviated slightly from the target (equiatomic) composition, and composition is known to affect stacking fault energies, it is possible that their alloy twins more readily than the polycrystalline alloy [243].

For comparison with the above room-temperature results, Fig. 13 shows the stress–strain curve of a <111> orientated specimen at 77 K. Shortly after yielding, clear stress drops can be seen in this figure and the authors also heard clicking sounds during the tests, both of which they attributed to twinning. Consistent with this, a DIC contour plot from the specimen surface after approximately 4% strain shows evidence of both slip and twinning (Fig. 14). From the first stress drop, which occurred at 450 MPa, and the trace analysis which led them to surmise activation of the (111)[121] twin system with the highest Schmid factor (0.34), they calculated a CRSS for twinning of ~153 MPa. This is again lower than the value estimated from the polycrystalline twinning stress [243], possibly due to some of the reasons outlined above. Interestingly, other studies [228,229] of [001]- and [111]-oriented single crystals of the CrMnFeCoNi alloy concluded that the CRSS for twinning was ~210 and ~170 MPa, respectively. These studies employed TEM to identify the onset of twinning, which is presumably more sensitive than the EBSD and DIC techniques employed by [227], yet the former studies yielded a higher twinning stress. Additional research is needed to resolve these discrepancies, both between different single-crystal studies and between single and polycrystal studies. In general, the twinning stress is believed to be relatively insensitive to temperature [265] and experiments on

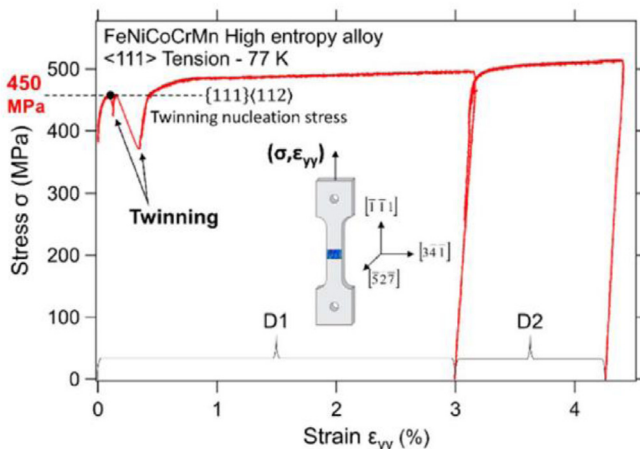


**Fig. 13.** Tensile stress-strain response at 77 K of <111> single crystal of CrMnFe-CoNi alloy. The first load drop indicates the onset of twinning at an axial stress of 450 MPa. After a strain of ~3%, the specimen was unloaded, polished and re-loaded so that EBSD and DIC characterization could be performed [227].

polycrystalline CrMnFeCoNi seem to bear this out [243]. Results within one research group, for example [227], seem to be self-consistent in that Schmid's law is valid and makes correct predictions for both slip and twinning. Similarly, the results of Kireeva et al. [225,229] are internally self-consistent and in line with what one would expect for single-slip versus multiple slip, twinning from intrinsic versus extrinsic stacking faults, etc. Additionally, all the evidence seems to suggest that some dislocation plasticity is needed before twinning is activated. Unlike in polycrystals where there is dislocation induced work hardening before twinning, in certain single crystal orientations there is little to no hardening associated with this initial plasticity suggesting that its role may not be primarily to raise the internal stresses to the CRSS for twinning but rather to assist twin nucleation by the motion of partials.

#### 2.2.2. BCC-based HEAs

It has been suggested that the ductility of BCC refractory alloys can be controlled by tuning the valence electron concentration

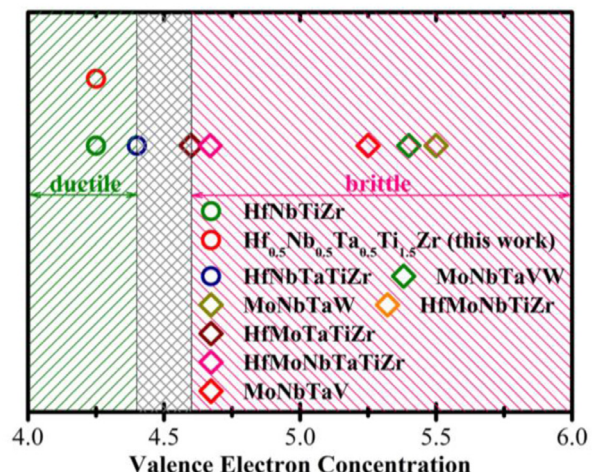


**Fig. 15.** Ductile and brittle behavior of BCC-based HEAs depending on the valence electron concentration [275].

(VEC), which affects the relative magnitudes of the ideal cleavage and shear strengths [271]. The basic idea is that in order for a material to be intrinsically ductile, dislocation nucleation, which relates to ideal shear and tensile strengths of the material, should be activated before the initiation of crack [272]. By calculating the band structure during deformation, Qi et al. showed that the decreasing the number of valence electrons in Mo and Nb alloys lowers the ideal shear strength [258], which in turn suggests that alloys with lower values of VEC would deform more easily and be more ductile. Senkov et al. developed MoNbTaV and MoNbTaVW refractory BCC-based HEAs with high yield strength and low ductility [273]. These alloys have large VEC, up to 5. On the other hand, HEAs that were discovered later (e.g., HfNbTaTiZr) have low yield strength and high ductility with smaller VEC, below 4.5 [144,274]. Sheikh et al. summarized this behavior using the concept of VEC as shown in Fig. 15 [275] and concluded that ductile behavior during tensile deformation occurs in BCC-based HEAs when the VEC is lower than 4.5. In these alloys, yield strengths are usually low over the whole temperature range. It appears that the intrinsic strength

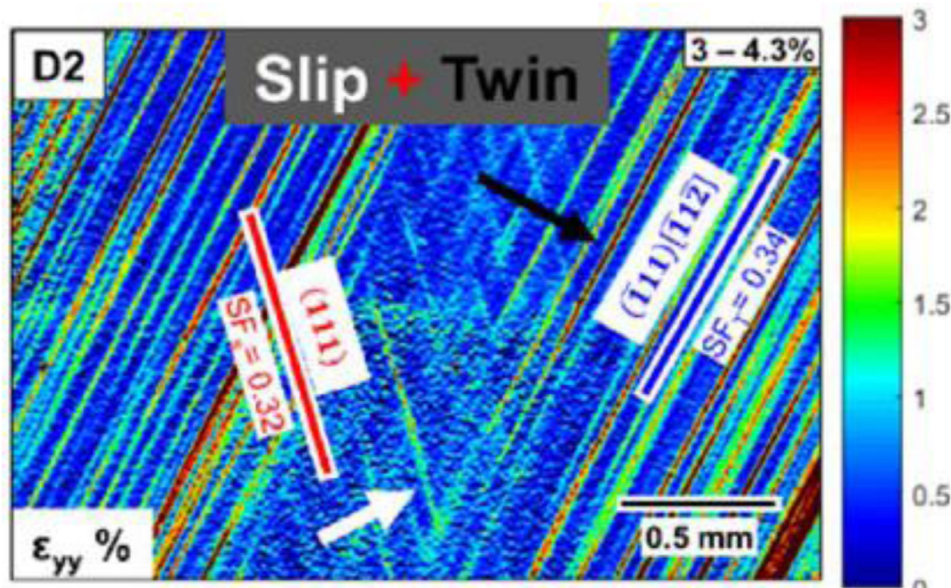


**Fig. 14.** DIC contour plot showing the normal strains associated with slip and twin bands after strains of 3~4% [229].

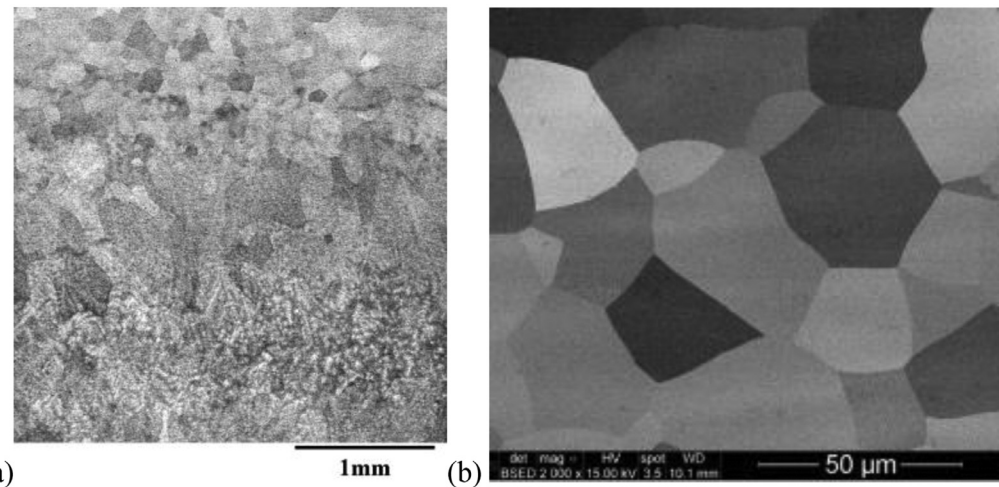


**Fig. 16.** (a) Microstructure of TiZrNbHfTa high-entropy alloy after casting and hot isostatic pressing [277] (left). (b) SEM backscattered image of TiZrNbHfTa high-entropy alloy after cold rolling (65% thickness reduction) and annealing at 1000°C for 2 h [138] (right).

and ductility of BCC-based HEAs are also affected by the VEC as in conventional refractory alloys.

**Solid solution effects:** Compared to the FCC alloys discussed earlier considerably less information is available on the detailed deformation behavior of BCC high-entropy alloys, probably because most of them are brittle at low homologous temperatures. Thus, of the several single-phase BCC high-entropy alloys that have been investigated, including NbMoTaW [114], VNbMoTaW [114], TiVZrNbHf [276] and TiZrNbHfTa [277], only TiZrNbHfTa is known to be ductile in tension. This alloy is very malleable and can be rolled heavily at room temperature (> 80% reduction in thickness) [278]. Consequently, its cast structure can be broken down and a fully recrystallized microstructure can be systematically investigated as a function of grain size. Since the first report of tensile properties in 2015 [278], it has received increasing interest and is currently the best understood BCC high-entropy alloy in terms of fundamental mechanisms. It is therefore our main focus here.

After arc melting and hot isostatic pressing (1473 K, 207 MPa, 3 h), the TiZrNbHfTa high-entropy alloy showed some remnants of a dendritic microstructure (see bottom half of Fig. 16a). They disappear after thermomechanical processing (cold rolling and recrystallization for 2 h 1000°C), and the microstructure becomes single-phase with a uniform grain size and homogeneous chemical composition (Fig. 16b). There were no preferred grain orientations in the transverse plane of the sheet.

Fig. 17 shows tensile true stress-strain curves of the TiZrNbHfTa high-entropy alloy in three conditions [138]. In the as-rolled state, the alloy exhibited intermediate strength with limited ductility and strain softening shortly after yielding. After the 800°C anneal, the yield strength increased but was accompanied by a noticeable decrease in ductility. Microstructural analysis revealed that partial recrystallization had occurred after this heat treatment, but that the original single-phase BCC structure [277] decomposed into two BCC phases with different lattice parameters [138]. After the 1000 °C anneal, the microstructure was fully recrystallized and consisted of a single BCC phase with the best combination of mechanical properties: yield strength of 1145 MPa, ultimate tensile strength of 1262 MPa, and elongation to fracture of ~8%. The fracture surface exhibited both ductile (transgranular) and brittle (intergranular) regions. Senkov and Semiatin [138] speculated that brittle second-phase films may be present on the grain boundaries that may have contributed to the observed intergranular fracture. It would be interesting to confirm this using, say, TEM or atom probe tomography. If confirmed, the next step would be to find ways to

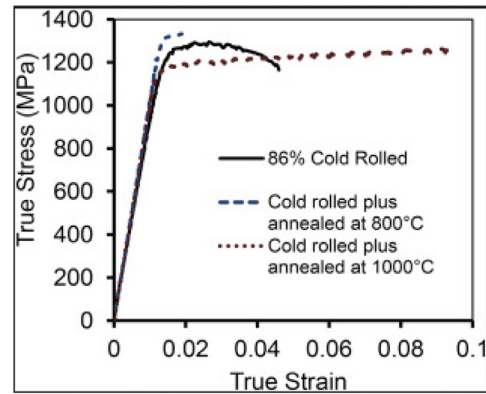


**Fig. 17.** True stress-strain curves of the TiZrNbHfTa high-entropy alloy in three different microstructural states [138].

eliminate it, thereby possibly improving ductility even further. Although the Young's modulus was estimated to be 100 GPa from the tensile tests, it would be useful to determine the elastic constants of this alloy using ultrasonic measurements.

TEM analyzes of deformed specimens to evaluate the micromechanisms of deformation have been performed only after compression and not yet on tensile tested specimens. Furthermore, they have been performed on as-cast specimens exhibiting compositional gradients reflective of dendritic segregation [112,279], which may influence the results. In compression [112], the work hardening rate initially shows a steep decline to ~3% true strain (stage I), then remains roughly flat up to strains of about 11% (stage II), followed by a weak decline at higher strains (stage III). Accordingly, Couzinié et al. [112] interrupted compression tests after 0.85, 2.3, and 10% plastic strains, which represent stage I, end of stage I, and end of stage II, respectively, and extracted samples from the gage sections for examination by TEM. Fig. 18a shows the typical substructure after 0.85% strain, which consists predominantly of  $\frac{1}{2}\langle 111 \rangle$  screw dislocations (the usual kind seen in BCC metals and alloys) arranged heterogeneously in distinct bands; dislocations of opposite signs and dipoles were present in the bands. Long, straight screw segments, as well as jogged sections and loops, were also found (Fig. 18b), which are easier to discern in the relatively dislocation-free regions between the bands. The dislocation structure remains heterogeneous through 2.3% plastic strain with numerous bands still present, similar to those shown in Fig. 8,

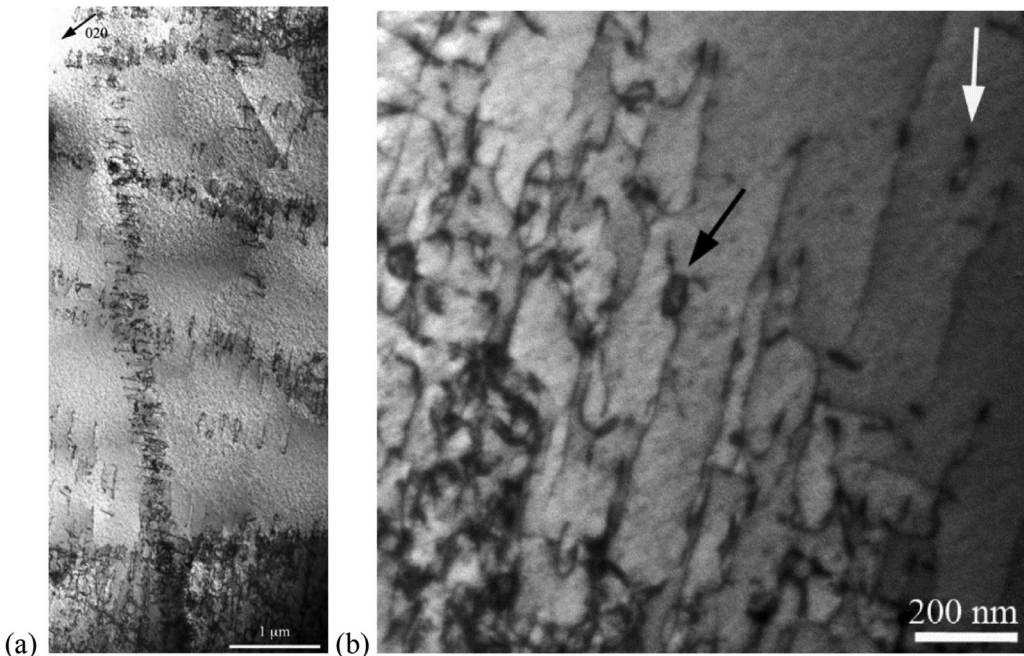


**Fig. 18.** (a) Bright-field TEM image of dislocation substructure in the TiZrNbHfTa high-entropy alloy after 0.85% plastic strain at room temperature [112]. (b) Long straight screw dislocations in the TiZrNbHfTa high-entropy alloy after 0.85% plastic strain at room temperature along with jogged sections and dislocation loops [112].

except at a higher density. In addition to the loops and dipoles mentioned above, dense dislocation tangles appeared in the bands [112]. Dislocation activity was not confined to the bands: screw dislocations were also present in the soft zones between bands (albeit at a lower density). At the end of stage II (10% strain), the dislocation distribution is much denser and more homogeneous, with the banding seen at lower strains having almost disappeared [112]. X-ray line profile analyzes confirmed the increase in dislocation density with strain, reaching a value of  $15 \times 10^{14} \text{ m}^{-2}$  at a plastic strain of ~20% in the TiZrHfNbTa alloy [113]. The analyzes also showed that the dislocation character became increasingly screw as the strain increased. The above TEM and X-ray results both point to a lower mobility of screw dislocations compared to edge dislocations, similar to what is typically observed in BCC metals and alloys. This contrasts with the observation of smoothly curved dislocations with no preference for edge or screw character in the FCC high-entropy alloy CrMnFeCoNi [154], which was indicative of similar mobilities of edge and screw dislocations as in other FCC metals and alloys.

Unlike in the FCC high-entropy alloy discussed earlier (CrMnFeCoNi), the strain hardening rate of the BCC TiZrHfNbTa alloy is relatively modest (see, e.g., Fig. 17). The hardening was fitted [113] to a simple Taylor hardening model,  $\Delta\tau = \alpha G b \sqrt{\rho}$ , where the increase in strength with strain (and, thus, dislocation density) depends on the hardening parameter,  $\alpha$ . Using the measured dislocation densities [113], it was concluded that  $\alpha$  for the TiZrHfNbTa alloy was low, 0.16 (similar to that of BCC metals), indicating that high Peierls stress is the main determinant of overall strength (through the high yield strength) with only a minor contribution from subsequent forest hardening. For comparison,  $\alpha = 0.4$  was estimated for the FCC high-entropy alloy CrMnFeCoNi [243] whose yield strength is relatively low but then undergoes significant forest hardening (similar to, say, Cu whose  $\alpha = 0.5$ ).

**Grain size effects:** Effects of grain size on the tensile properties of TiZrNbHfTa were investigated in a later study and yield strength was found to be roughly the same (~950 MPa) for grain sizes of 38, 81 and 128  $\mu\text{m}$  [155]. This value is substantially lower than the yield strength mentioned above (1145 MPa), which was for a

grain size of 22  $\mu\text{m}$  [138] and cannot be rationalized as a Hall-Petch effect. Precipitation of second phases is known to occur in certain temperature ranges in this alloy system [101,138,142,280], which can affect mechanical properties. Depending on the relative cooling rates used (15 K/min in [138], unknown in [155]), it may be possible that fine precipitates are present that may be visible only by TEM (not performed in either study). Another factor that may come into play is texture which depends strongly on thermomechanical processing [138]. Finally, interstitial elements, whether present as impurities or intentionally added, have long been known to affect the strength and ductility of refractory metals, for example O in Mo [281,282] and Nb [282]. Segregation to the grain boundaries has been implicated in some cases [282]. Therefore, care has to be exercised in interpreting Hall-Petch data since impurities can affect the slip-transfer resistance of grain boundaries. In the refractory HEA literature, detailed chemical compositions are rarely reported (especially, impurities that might be present in trace amounts). Future studies should measure the actual chemical compositions of the investigated alloys.

**Activation volumes:** Apparent activation volumes at room temperature have been measured using the load relaxation technique and determined to be ~40–50  $b^3$  in stage I of strain hardening (up to ~1% plastic strain) and decreased to ~30  $b^3$  toward the end of stage II (~10% strain) and into stage III [112]. The authors [112] concluded that these low values were similar to those measured in other BCC metals and alloys and indicative of a strong Peierls barrier and a mechanism involving kink-pair formation on screws as the operative unit event of deformation. Furthermore, the weak dependence of the apparent activation volume on plastic strain suggests that forest hardening contributes only modestly to the flow stress, consistent with the low value of the Taylor hardening parameter ( $\alpha$ ) discussed earlier. Another study on a non-equiautomic alloy comprising the same constituent elements ( $\text{Ti}_{17.7}\text{Zr}_{12.7}\text{Nb}_{30.8}\text{Hf}_{8.0}\text{Ta}_{30.8}$ ) found similar activation volumes [107].

**Elevated-temperature compressive behavior:** The elevated-temperature flow behavior of the TiZrNbHfTa high-entropy alloy has been investigated only in compression [155,283]. Representa-

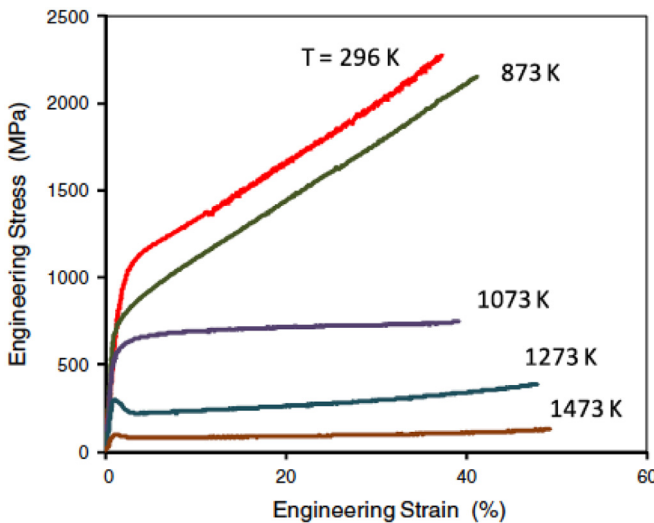


**Fig. 19.** Compressive stress-strain curves of the TiZrNbHfTa high-entropy alloy at a strain rate of  $\sim 10\text{--}3 \text{ s}^{-1}$  and various temperatures [283].

tive stress-strain curves at a strain rate of  $10^{-3} \text{ s}^{-1}$  are shown in Fig. 19. This alloy was prepared by vacuum arc melting, following which the button was hot isostatically pressed (1473 K, 207 MPa, 1 h) and then annealed in vacuum for 24 h at 1473 K [283]. Back-scattered electron images taken in a SEM [283] showed a non-uniform grain size (likely due to the non-uniform cooling rate of the arc-melted button) and a non-homogeneous composition across the grains (likely a remnant of dendritic segregation). Only X-ray diffraction and SEM analyses were performed on this material; therefore, information about its fine scale structure is lacking. The other study mentioned above [155] tested the TiZrNbHfTa alloy in the as-cast state; no information was provided about its microstructure, but some compositional segregation was likely present.

At relatively low homologous temperatures ( $\leq 873 \text{ K}$ ), there is significant work hardening after yielding and the rates appear to be roughly independent of temperature (Fig. 19). At higher temperatures, the alloy exhibits either steady-state flow (at 1073 K), or a drop in the flow stress after yielding followed by weak to practically no hardening (at 1273 and 1473 K). Associated with the steady state flow at 1073 K was grain boundary cavitation, dynamic recrystallization, and the formation of (unknown) nanoparticles in specimens observed by SEM after 50% compression [283]. Strain rate (as is usually the case in most materials) had the inverse effect of temperature [283]: for example, at 1073 K, the stress-strain curves at higher strain rates ( $10^2$  and  $10^{-1} \text{ s}^{-1}$ ) exhibited clear strain hardening (as opposed to the flat curve seen in Fig. 19 at 1073 K), whereas the lower strain rate curves looked like the higher temperature (1273 K) curve in Fig. 19. Examination of specimens compressed 50% at room temperature revealed no signs of strain localization at low magnification and elongated grains along the deformation direction and fine lamella inside the grains at high magnification which the authors speculated might be distorted deformation twins and shear bands [283]. However, a later TEM study [179] did not find evidence for deformation twinning at room temperature in the TiZrNbHfTa high-entropy alloy.

As discussed in Section 2.1, property improvements realized in BCC HEAs and CCAs may benefit from effects other than solid solution strengthening, such as metastability, interstitial-hardening, or short-range ordering. For example, it was shown that the ordered-oxygen complexes can be formed in oxygen doped refractory TiZrHfNb HEA with the body-centered cubic (BCC) crystal structure, while the nitrogen atoms are randomly dissolved in the ma-

trix [96]. The oxygen complexes are large (several nm scale) and strong, and thus dislocations cannot destroy and bypass the complexes. As a result, the authors propose that the strong pinning effects of oxygen complexes reduce slip planarity, promoting dislocation multiplication for higher strength and ductility. It could thus be proposed that dislocation multiplication and overcoming of strength-ductility trade-off in BCC-based HEAs can be achieved by extremely strong pinning effects of interstitial SRO. Doping interstitial elements to refractory alloys has been known to significantly decrease the ductility. The unexpected benefits of SRO for overcoming the previous limitations in property enhancements, motivate systematic studies on the effects of interstitial SRO size and strength.

### 3. Theory, modeling, and simulation of mechanical properties of HEAs

In this section, we try to present a holistic overview of the modeling of mechanical behavior in HEAs, starting with basic modeling concepts and methods that are not limited to HEAs and then examining specific work on HEAs. The discussion expands on topics and issues mentioned in Sections 1 and 2, but focusing in more detail on theory, modeling, and simulation aspects.

#### 3.1. General overview

The principal goal of theory, modeling, and/or simulation is to relate fundamental material properties to macroscopic material behavior. Fig. 20 schematically illustrates the conceptual thought process: fundamental properties are connected to specific nanoscale mechanisms of deformation, which then collectively give rise to the various macroscopic properties. The modeling strategy to achieve this is schematically illustrated in Fig. 21. The central feature in Fig. 21 is the role of “mechanistic predictive theory” of “deformation mechanisms” so as to relate computable “material properties” to measurable “mechanical behavior”. “Deformation mechanisms” involve the motion and interaction of defects in the crystalline lattice. The primary defects are dislocations, which are the carriers of plastic displacement giving rise to plastic strain. Other important defects are grain boundaries, which interact with or create dislocations to give rise to Hall-Petch strengthening effects widely observed in HEAs, and vacancies, which mediate diffusion of elemental species, and thus creep, segregation, and other elevated-temperature properties. Deformation mechanisms such as stress-induced phase transformations and twinning are also connected to the macroscopic properties. The “mechanistic theory” for HEAs should thus be primarily focused on the study of how defects behave in the random alloy.

Experimental observations clearly show the existence and motion of dislocations on the expected slip systems in both FCC and BCC crystals. The observations show some randomness; for instance, the partial dislocation separation in FCC CoCrFeMnNi varies somewhat around an average value [246]. But this involves only the behavior of the dislocations and not their fundamental existence. The stress-strain curves for this FCC alloy [100] versus temperature can also be fit to a standard form that involves a grain-size-dependent Hall-Petch contribution, a rate- and temperature-dependent solute-strengthening contribution following standard theory [284], and a rate- and temperature-dependent forest-hardening contribution following standard theory [285–287],

$$\sigma(T, \dot{\varepsilon}, \varepsilon_p, d) = \sigma_{HP}(d) + \sigma_{ss}(T, \dot{\varepsilon}) + \sigma_f(T, \dot{\varepsilon}, \varepsilon_p) \quad (1)$$

as shown in Fig. 22; this form neglects any strength associated with a fundamental Peierls stress because this contribution is usually very small in FCC elements. The details of the fitting are not

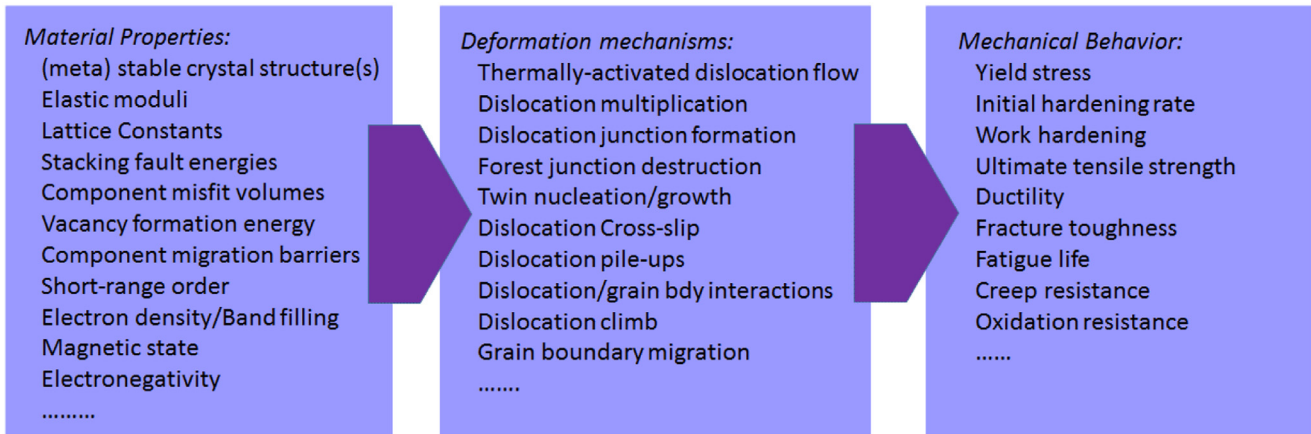


**Fig. 20.** Connection of fundamental materials properties to specific mechanisms of deformation, leading to observed macroscopic mechanical behavior.

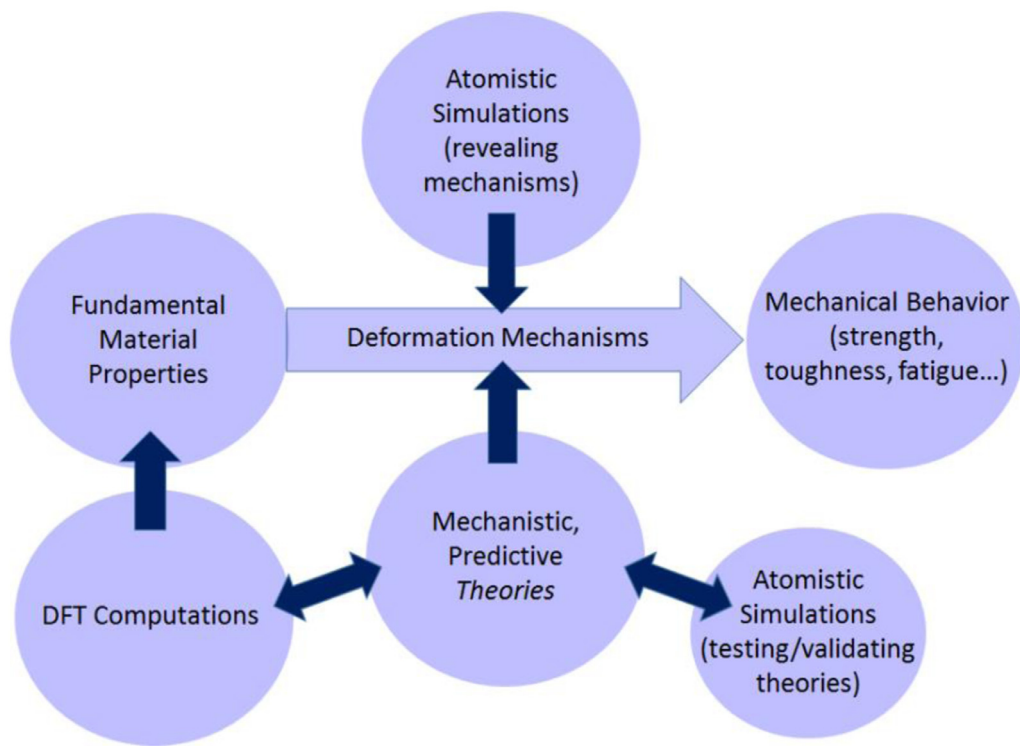


**Fig. 21.** General modeling strategy wherein mechanistic predictive theories provide the link between material properties and mechanical performance, with first-principles computations providing chemical input and atomistic simulations serving to independently reveal possible mechanisms and to test and validate the theories.

important – there are a few strength and energy barrier parameters for solute and forest strengthening – the point is that the entire behavior can be accounted for by standard dislocation-based mechanics concepts.

Examining the macroscopic behavior further, perhaps the most comprehensive single representation of thermally-activated dislocation-based plastic flow comes from the Haasen plot of inverse activation volume  $V$  versus flow stress minus initial yield stress,  $\sigma - \sigma_y$  [288]. When the strain rate is expressed as an Arrhenius law with a stress-dependent activation barrier as  $\dot{\epsilon} = \dot{\epsilon}_0 \exp(-\frac{\Delta G(\tau)}{kT})$  then activation volume is defined as

$$V = -\frac{\partial(\Delta G(\tau))}{\partial \tau}|_T = -M \frac{\partial(\Delta G(\sigma))}{\partial \sigma}|_T = MkT \frac{\partial \ln(\dot{\epsilon})}{\partial \sigma}|_T \quad (2)$$

where  $k$  is Boltzmann's constant,  $T$  is the temperature, and  $M$  is the Taylor factor relating shear and uniaxial stresses in a polycrystalline material,  $\sigma = M\tau$ . A standard Haasen plot of  $MkT/V$  ver-

sus  $\sigma - \sigma_y$  shows two main features. At the yield stress  $\sigma - \sigma_y = 0$ , there is an initial activation volume attributed to solute strengthening that reveals the activation area ( $A = V/b$ ) swept by a dislocation in overcoming the barriers created by collective solute fluctuations [284]. Above yield, there is then a linear increase in the inverse activation volume that demonstrates the Cottrell-Stokes law for forest strengthening, where the forest activation area scales as  $1/\sqrt{\rho}$  and the flow stress scales as  $\sqrt{\rho}$ . Fig. 23 shows the Haasen plots for the canonical FCC CoCrFeMnNi alloy [100] and the BCC TiZrHfNbTa alloy [279]. Both HEA materials follow the expected behavior. The magnitude of the initial FCC activation area reveals a material length scale  $A \sim 100 b^2$  or, if not a dislocation process,  $V \sim 300 b^3$ . This magnitude is comparable to moderate-concentration binary solute-strengthened alloys. Furthermore, this large scale would be difficult to rationalize via other mechanisms. There is therefore no need to invoke special new mechanisms to explain the basic rate- and temperature-dependent deformation in ei-

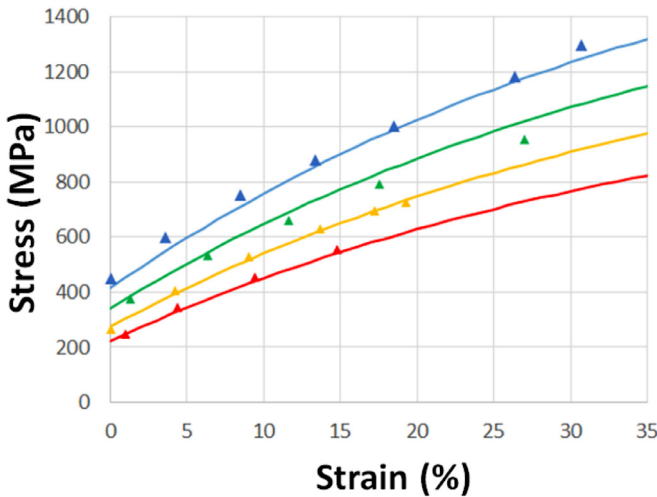


**Fig. 22.** Stress-(plastic) strain curves for the FCC CoCrFeMnNi HEA, as measured (symbols) and as predicted by standard modeling (lines) at temperatures  $T=77$  K (blue, upper), 173 K (green), 293 K (yellow), and 423 K (red, lower). Data taken from [100]. (For interpretation of the references to color in this figure legend, the reader is referred to the web version of this article.)

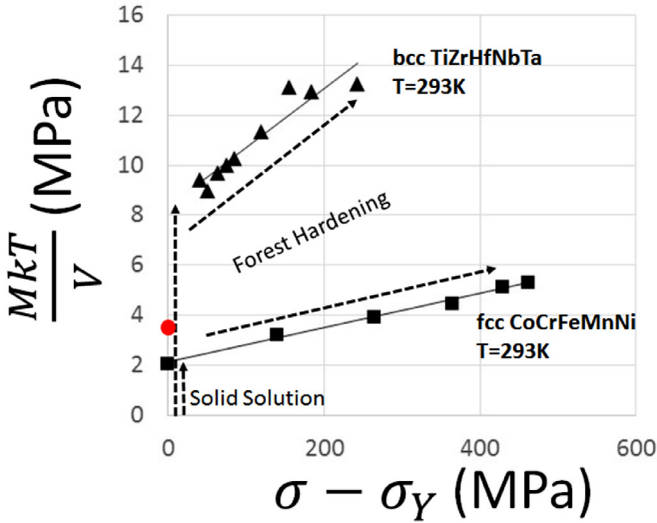


**Fig. 23.** Haasen plot of scaled inverse activation volume  $V$  versus stress beyond initial yielding, as measured for two different HEAs at  $T = 293$  K. Also shown by the red circle is the parameter-free prediction using the theory of Varvenne et al. [237]. Data on BCC TiZrHfNbTa replotted from [279]; data on FCC CoCrFeMnNi replotted from [100]. (For interpretation of the references to color in this figure, the reader is referred to the web version of this article.)

ther FCC or BCC HEAs. This does not rule out the existence of other as-yet unknown mechanisms, but such mechanisms are not essential based on existing data. Most importantly, a solid theoretical understanding of HEAs can begin by building on the vast detailed understanding of deformation mechanisms in non-HEAs.

If we can build on existing knowledge, then we know what fundamental material properties to compute. First-principles methods (mainly density functional theory DFT) provide the material properties, which then serve as input to “mechanistic theory”. DFT can be, and has been, used to compute the fundamental material properties such as lattice constants, elastic constants, stacking fault energies and Gamma surfaces, vacancy formation energies and migration barriers, and cohesive energies as a function of composition and crystal structure. Performing such calculations in systems with magnetic elements remains difficult, and various approaches

are being developed [289]. Stacking fault energies pose a particular challenge, and results to date vary considerably for some important systems [42,290], as discussed later. It is noted at this point that standard spin-polarized DFT using standard exchange-correlation potentials is well-known to differ from experiments in some important quantities. For instance, atomic volumes of the elements often deviate from experiments by modest amounts. This can lead to errors in computations of solute misfit volumes, atom-atom spacings, and other quantities such as stacking fault energies. Alternative functionals can give different volumes, but consistent errors remain across elements. Elastic constants can also be inaccurate, with the most glaring error being the prediction of the shear modulus  $C_{44}$  in the BCC elements; this will introduce unknown errors when computing other mechanics-related properties or defects. Thus, while first-principles methods provide the best route toward chemically-accurate atomic-scale energies, the quantitative results from computationally-feasible methods such as DFT must always be considered carefully.

From DFT-computed material properties, when sufficiently accurate, it is then possible to determine dislocation Burgers vectors and apply elasticity theory to dislocation-related processes. For instance, elasticity, Burgers vector, and stable stacking fault energy together enable prediction of the partial dislocation separation in FCC metals. In fact, experimental measurements of partial dislocation separation have been used to estimate the stacking fault energy in both CoCrFeMnNi and CoCrNi. This is not yet a mechanical property. However, knowledge of the stable stacking fault energy can be used to estimate the twinning stress, assuming the material behaves like an elemental alloy and relying on the accuracy of twinning theories (see below). The DFT-computed lattice constant as a function of elemental concentrations  $\{c_n\}$  ( $n=1,\dots,N$  in an N-component alloy) can be used to compute the misfit volumes  $\{\Delta V_n\}$  of the individual elements in the alloy (see below). Again, this alone is not a mechanical property, but enters solute strengthening theories. If the underlying atomic disorder is ignored, and the material is considered as consisting of continuum dislocations, then knowledge of elastic constants and Burgers vectors can be used to predict forest junction strengths as if the material were an elemental alloy. A typical scaling of strength as  $\sigma = \alpha \mu b^2 / \sqrt{\rho}$  would then be expected. DFT studies have also revealed picometer scale atomic deviations of atom positions (ADP; see Section 2) from the underlying perfect FCC lattice. These DFT studies and experimental measurements of the distortion have been then correlated with the full measured yield stress (normalized by the shear modulus) as in Fig. 30 below, although the reasons for such a correlation remain unknown (see below). Thus, some progress can be made based on DFT-computed properties and basic dislocation mechanisms and/or correlations.

In parallel with DFT simulations, atomistic simulations (molecular dynamics or statics; denoted here collectively as MD) can provide insights into the operative deformation mechanisms in alloys including HEAs. The most powerful use of MD is probably in testing mechanistic theories. Atomistic simulations provide a precise laboratory where all material quantities are known/calculable, and complex interactions of dislocations with other defects can be studied in detail. While the simulations are rarely precise for any real material, due to the limitations of the underlying semi-empirical interatomic potentials typically used, the simulated materials can be very suitable model materials for testing the inevitable approximations/assumptions that arise in a theory. As long as the interatomic potentials do not have pathologies, i.e., unphysical behavior, they can be used to test theories. An example is the use of the ternary Cr-Fe-Ni potential for FCC structures by Bonny et al. [355] This potential is not quantitative for any Cr-Fe-Ni materials but is not pathological and so was used to test a theory for solute strengthening in FCC HEAs [237].

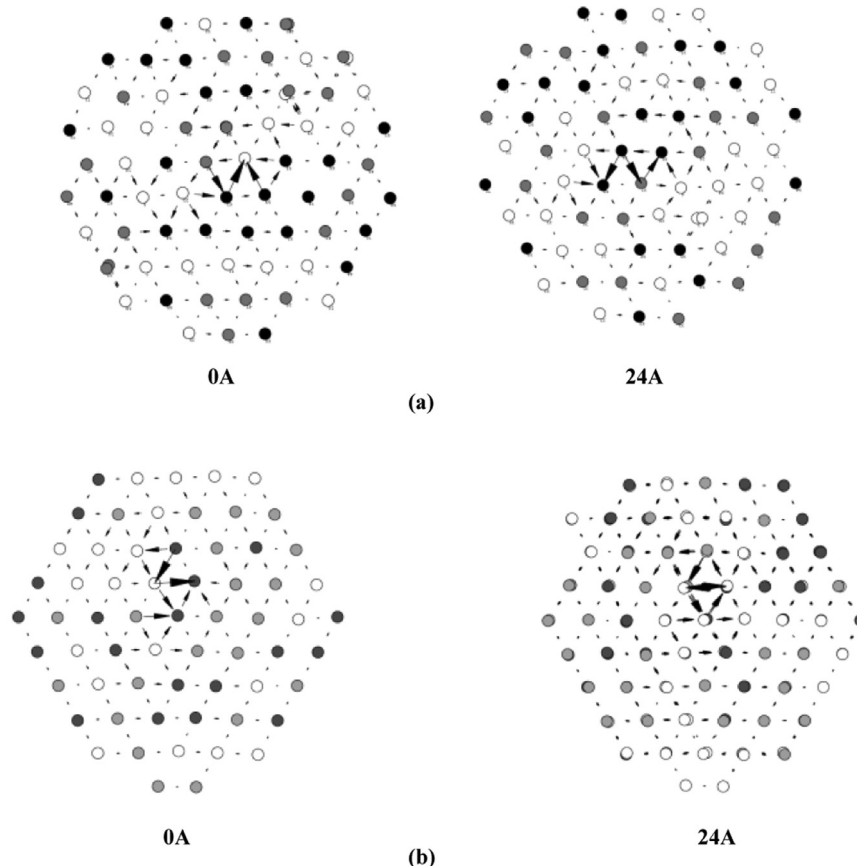


**Fig. 24.** Differential displacement maps of the screws dislocation core structures in TiZrNb as predicted by (a) the Zhou et al. interatomic potentials and (b) DFT using flexible-boundary conditions, for two different sections of width  $2b$  along the screw dislocation line. Data reproduced from [293].

MD simulations can also be applied without any underlying theory to reveal possible mechanisms or gain some semi-quantitative understanding of behavior. Such work has been executed by Rao et al. for both model FCC and BCC alloys [291]. As hinted above, the major problem with MD simulations on alloys is that reliable artifact-free interatomic potentials for multi-component alloys generally do not exist. Even for binary alloys, high-quality potentials are limited to a few FCC cases. For HEAs, there is a broad class of EAM-type potentials by Zhou and co-workers, that can be combined to create complex alloy potentials [292]. These thus have some utility but with unknown quantitative accuracy. For BCC crystals, and the study of screw dislocations at low temperatures, the Zhou et al. potentials are broadly inadequate because they do not yield the correct non-polarized cores for all elements and have a local metastable minimum energy in the so-called split-core configuration. These are common flaws of EAM-type potentials. Thus, some reported phenomena in the BCC MD study by Rao et al. may be unphysical. However, the general conclusion that the high local disorder in BCC HEAs generates complex variations of core structure along the line of a single screw dislocation is plausible and supported by new work by Rao et al. on the Ti-Zr-Nb family of HEAs [293]. They have studied screw dislocation cores computed via both DFT methods and the Zhou et al. potentials and have shown similar types of distortions of the core structure (Fig. 24). More advanced potentials, such as the Bond-Order Potentials (BOP), are far better for BCC screw dislocations and are being developed for alloys [294,295]. This will enable more-realistic simulations for BCC HEAs.

Due to the limited time scales of MD simulations ( $\sim 1$  ns and usually much shorter), true rate- and temperature-dependent plas-

ticity behavior at realistic rates and temperatures is not computationally feasible. A back-of-the-envelope assessment shows that the typical energy barriers that can be overcome in a 1 ns MD simulation at room temperature are only  $\Delta E \sim 0.15\text{eV}$ . To accumulate a representative number of thermally activated events requires application of high stresses to lower the energy barriers further, which could lead to dynamic instabilities/overshoot. In contrast, from an Arrhenius law for the plastic strain rate,  $\dot{\epsilon} = \dot{\epsilon}_0 \exp(-\frac{\Delta G(\tau)}{kT})$  where  $\dot{\epsilon}_0 \sim 10^4 - 10^5/\text{s}$  is a reference strain rate the barriers controlling plastic flow at a typical experimental strain rate of  $\dot{\epsilon} = 10^{-4}/\text{s}$  and room temperature are around  $\Delta G \sim 0.5\text{eV}$ . Barriers of this magnitude are simply not accessible in direct MD simulations.

Simulations are also often executed using a constant strain rate applied to the MD sample. Such a test often has no direct relationship to the plastic strain rate in experiments. Experimentally, the plastic strain rate is generated by many dislocations at some density  $\rho$  moving via thermal activation through the crystal. In an MD sample containing one dislocation, the plastic strain rate is the area swept by the single dislocation multiplied by the Burgers vector and divided by the sample cross-sectional area perpendicular to the dislocation line direction. In MD, this “strain rate” is then sample-size-dependent, and independent of the applied strain rate imposed on the sample boundaries. A better approach to obtaining the plastic strain rate is to hold the specimen at a fixed load for a specified time and then measure the distance moved by the dislocation. This provides the plastic displacement rate per dislocation, which can be converted into a bulk plastic strain rate with knowledge of the dislocation density in the real material of interest.

To partially overcome the general time scale issue in MD, there are two prevailing strategies: accelerated MD methods [296,297] and transition-state methods [298,299]. The latter are powerful and direct, enabling computation of the saddle-point barriers between an initial state and a final state. Methods such as the Nudged Elastic Band method and the String method are widely available, and have been applied to study the barriers to dislocation nucleation and motion in various problems including alloys [300,301]. These methods are computationally costly and may be difficult to converge, making their application in sufficiently large dislocation problems having high atomistic complexity daunting. This has limited their application to HEAs at the present time, although these methods hold exceptional promise.

It can also be difficult to mechanistically interpret MD simulations of dislocation structure or motion in the complex HEA systems. The simulation cannot separate out the effects due to the extreme local disorder from the effects of the underlying average material properties. Computations on large samples (many thousands of atoms) can be performed to extract average bulk properties (lattice constants, elastic constants, stacking fault energies, surface energies, solute misfit volumes) but these are not directly connected to the behavior of the dislocation in the true random alloy. Progress to circumvent this barrier was made by Varvenne et al. [302] who revitalized an old but under-exploited idea wherein EAM interatomic potentials can be formally homogenized, for any number of alloy components and compositions, to create a single new “average atom”. The “average atom” potential enables the creation of a crystalline material that has (very nearly) the bulk average properties of the true random alloy (lattice constants, elastic constants, surface energies, stacking fault energies, surface energies, etc.), *but does not have the local disorder*. Varvenne et al. [302] further showed that the properties of individual elements, considered as solutes in the average alloy, could be accurately computed by inserting them into the average alloy matrix. The concept of the homogenized matrix, and the properties of the constituent elements as solutes in that matrix, is an essential insight for understanding a number of aspects of HEA plastic flow behavior, as discussed below. Use of this method enables direct comparisons between simulations performed on a true random alloy and on the homogeneous “average atom” alloy, revealing which properties are controlled by “average” material properties and which properties are controlled by the atomic-scale disorder. Such a study reveals, not surprisingly, that an “average atom” FCC HEA alloy always has a very low  $T=0$  K Peierls stress ( $< 10$  MPa) just as found in simulations of elemental metals like Al, Cu, and Ni. The true random alloy at the same composition has a much higher initial  $T=0$  K yield stress (100 s of MPa) [302], directly implicating the interaction of the dislocation with the atomic disorder as the source of the strengthening.

With this general background, we next proceed to discuss basic concepts related to HEA strengthening, recent correlations, basic mechanistic models, and predictive mechanistic models that have been recently developed to capture deformation phenomena in HEAs. The most-studied property is initial yield stress, and so this will dominate the discussion. The most-studied material is the FCC 5-component CoCrFeMnNi Cantor alloy, and its variants, and so this will also dominate the discussion.

### 3.2. Basic concepts

Since HEA strengthening occurs via dislocation motion through the alloy, there are a number of classic basic concepts related to strengthening of metals that have been revisited for possible relevance to HEAs.

Early HEA literature attempted to apply a basic Peierls models for elemental alloys to HEAs. In elemental FCC alloys, the Peierls

stress is controlled by the dislocation overcoming the atomic scale Peierls barrier associated with the unstable stacking fault energy. Simple elastic models then lead to a dependence of the Peierls stress on the spreading, or width, of the dislocation core. Such simple models are not quantitative in the FCC elemental models, but were nonetheless considered for HEAs. Specifically, the high initial flow stress was attributed to the (average) Peierls barrier of the alloy with no explicit treatment of the atomic-scale disorder [43]. This concept is still invoked in recent work [303] but is simply not valid, as demonstrated by the study of Varvenne et al. mentioned above on true random and averaged-alloy (no randomness) alloys of the same composition [302] and same core width. The strengthening in HEAs, occurring due to the randomness at the atomic scale, has also often been termed as “the friction stress”. The term friction stress should normally be limited to the fundamental Peierls stress, which is very small in FCC metals, and so this terminology is misleading. The strengthening in the HEA, while at scales well below the typical scales of forest dislocation and precipitate strengthening, is not a friction stress in the traditional sense of the Peierls stress [302]. As indicated by Eq. 1, the “friction stress” interpreted as “any strengthening aside from the Hall-Petch contribution”, is “solute strengthening” and should probably be referred to as such. This point is further reinforced by the measured activation volume in the Cantor alloy of  $\sim 70$   $b^3$  at  $T=77$  K [100], which demonstrates that the strengthening is not controlled by phenomena at the atomic scale.

Classical understanding of alloy behavior has also been framed in terms of a collective size-misfit parameter, the  $\delta$  parameter that appears in the Hume-Rothery rules. The  $\delta$  parameter has been frequently assessed using atomic lattice spacings between local pairs of atoms or atomic radii. It is often implicitly assumed that these local atomic spacings are related directly to the misfit strains (e.g., a misfit volume for substitutional solutes in a cubic crystal). The conceptual picture is based on a continuum analogy: the solute atom is treated like a continuum inclusion having a different size and modulus as compared to the matrix material. This analogy is not precise and can be misleading. When an atomic solute is introduced into a matrix crystal, the solute misfit volume is not equal to the local volume of the solute atom as computed, for instance, by a Voronoi construction using the (displaced) positions of the surrounding host atoms. That is, the “misfit volume” is not, in general, local to the solute atom nor related to the distance between the solute and its host neighbors. An example to establish this point quantitatively is Cr in Al. The Al atomic volume is  $16\text{\AA}^3$  and the Cr misfit volume in Al is  $-11\text{\AA}^3$  as computed reliably in DFT [304]. If interpreted entirely locally, the volume immediately surrounding a Cr atom would be only  $5\text{\AA}^3$ , which is certainly not observed. Further calculations in complex non-dilute model alloys reinforce this result [Varvenne and Curtin, unpublished]. The local volume change at the solute atom is thus not closely related to the macroscopic misfit volume of the solute. There is one analysis in which the misfit volume is computed by considering the initial volume to have a radius equal to the atomic diameter rather than the atomic radius. This ad-hoc definition, which we are not able to rationalize, introduces a large additional factor that leads to a reasonably good correlation of “misfit” volume and change in atomic spacing for solutes in Al, see [305] and references therein.

Furthermore, it is not easy to separate the classic so-called “elastic” and “misfit” contributions of an individual solute – atoms are not balls connected by near-neighbor springs. Introducing a solute into a matrix leads to surrounding distortions and a global volume change equal to the net misfit volume including hypothetical “elastic” and “misfit” contributions simultaneously. The “elastic” misfit can only be strictly identified by examining the total energy changes of the system under an applied load. The contri-

bution to the energy from the misfit strain is  $\sim \sigma_{ij} \epsilon_{ij}^{misfit} V_0$  where  $V_0$  is the host atomic volume, and only the deviations from that energy change would indicate an additional “elastic misfit” contribution. To our knowledge, such energy changes are generally found to be small, indicating that real “elastic” contributions to the misfit volume are probably negligible. In the non-dilute limit, there is an average alloy matrix with average atomic volume and average elastic constants determined by the constituent atom properties. The misfit volume of any one solute in that non-dilute alloy is then different than in the dilute limit and cannot be easily decomposed into “elastic” and “misfit” contributions.

In the context of strengthening, what matters is the interaction energy of a solute with a dislocation. In elasticity and for a substitutional solute in a cubic crystal, this interaction is usually most-directly computed as the product of the dislocation pressure field at the position of the solute and the solute misfit volume. This suggests that the local picture of the misfit volume is correct, but this is again misleading. The interaction energy is the work done by the distortions caused by the solute acting against the dislocation pressure field; the distortions are non-local but reduce to a local result when the gradients in the pressure field are small. Both atomistic and first-principles studies show that the accuracy of the elasticity approximation is surprisingly good, even in the core region of the dislocation. Thus, a primary contribution to the solute/dislocation interaction energy is due to the solute misfit volume in the alloy.

The solute misfit volumes in any random alloy are also not ambiguous and can be established by macroscopic considerations. At a given random alloy composition  $\{c_i\}$  ( $i=1,\dots,N$ ), for which the average atomic volume is  $V$ , the addition of an infinitesimal concentration  $dc_i$  of element  $i$  replacing, at random, other solutes, so that  $dc_j = -c_j dc_i / (1 - c_i)$  ( $j \neq i$ ), leads to a change in average atomic volume of  $dV_i$ . The misfit volume of element  $i$  at the composition  $\{c_i\}$  is then  $\Delta V_i = (1 - c_i) \left( \frac{dV_i}{dc_i} \right)$ . This is exact and macroscopic, relying in no way on any precise local distortions created by the change in composition. A similar construction can be performed in terms of the alloy lattice constant  $a$  instead of the atomic volume. Such misfit volumes are closely related to the quantity  $\delta_i = \frac{1}{a} \frac{da}{dc_i}$  that appears in solute-strengthening models, as noted in the HEA context by Toda-Caballero et al. [306]. The issue in a complex alloy is how to determine the average alloy lattice parameter  $a$  or volume  $V$  as a function of the alloy composition  $\{c_n\}$  so that the derivative may be computed. Experimentally, it is painstaking to obtain atomic volumes at the fine scale of composition resolution needed to determine the misfit volumes accurately. However, the procedure above can be executed computationally in random alloys using interatomic potentials [302] or first-principles DFT [307]. A simple classical approximation is Vegard’s law, which is a linear rule-of-mixtures formula. For elements that all crystallize in the same structure, we denote the elemental volumes as  $\{V_{0i}\}$  ( $i=1,\dots,N$ ). Vegard’s law then approximates the average atomic volume of the alloy as  $V = \sum_i c_i V_{0i}$ , from which the misfit volume of solute  $i$  is then determined as  $\Delta V_i = V_{0i} - V$ . Vegard’s law has a long history, and has been found to be quite accurate in many binary alloys and so has been used for a number of HEAs.

Another basic issue that is crucial for interpreting experiments in the context of theories or models is the relationship between hardness and yield strength. Hardness is easy to measure but generally correlates with the strength at around 10% plastic strain and so depends on the work hardening rate of the alloy. Thus, hardness is not directly related to the initial yield stress unless the material shows very low work hardening. Many HEAs, especially the FCC HEAs, show high work hardening, invalidating any quantitative comparison of hardness and initial yield strength. Numerical simulations of the hardness for Berkovich and Vickers indentation have been performed for many systems, and recent work shows

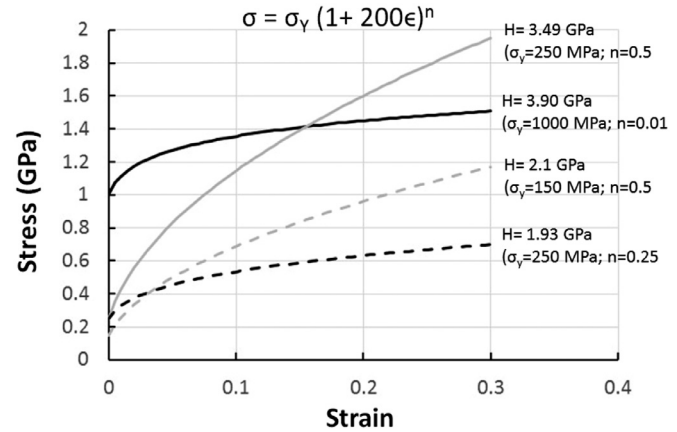


**Fig. 25.** Stress vs. strain for several model power-law plastic materials, with the corresponding numerically-derived hardness values for each alloy [308]. Alloys denoted by the solid lines have comparable hardness values but very different initial yield strengths and work-hardening parameters. Alloys denoted by the dashed lines also have comparable hardness by very different underlying material parameters. Hardness tends to correlate with the flow stress at approximately 10% plastic strain.

result for varying initial yield strengths and work hardening rates [308]. We have selected two sets of results to illustrate the problem. Fig. 25 shows the stress-strain curves for four materials with different yield stresses and work hardening exponents in a power-law hardening model. Two of the materials have similar hardness values around  $H=3.5$  GPa, but with initial yield stresses differing by a factor of 4. The two other materials have similar hardness values around  $H=2.0$  GPa but with initial yield stresses differing by a factor of 1.65. In all cases,  $\sigma(\epsilon_p = 0.1) \approx H/3$  holds with modest accuracy. These examples show that hardness can be used to compare different materials, but that materials with the same hardness may have very different initial yield stresses. Theories for initial yield stress therefore should not generally be compared to measured hardness values without additional knowledge of the work hardening rates. Complicating matters further is the fact that plastic flow is also strain-rate-dependent and the hardness measurement does not have a unique strain rate. However, experimental correlations of hardness and yield stress can be made to validate a relationship  $\sigma_y \approx H/\beta$  with  $\beta \sim 3$  for low-hardening systems. This has been done in some systems such as BCC HEAs where the work hardening rate is low relative to the yield stress [46].

In the following sections, we now address theory and modeling progress on mechanical behavior of HEAs with more specific detail.

### 3.2. Yielding behavior

#### 3.3.1. FCC alloys

The initial yield strength has been the most widely examined property, presumably because the onset of plastic flow is related to fundamental individual dislocation motion at low dislocation densities where contributions due to forest hardening are minimal and can be neglected. However, the FCC HEAs exhibit non-negligible Hall-Petch strengthening  $\sigma_{HP}(d)$  that is not associated with the underlying motion of a dislocation through the random alloy. Thus, the measured initial flow stress is presumably  $\sigma_y(T, \dot{\epsilon}, d) = \sigma_{HP}(d) + \sigma_{ss}(T, \dot{\epsilon})$ , which requires independent theories for  $\sigma_{HP}(d)$  and  $\sigma_{ss}(T, \dot{\epsilon})$ , where we leave the subscript “ss” as justified from Figs. 22 and 23, and discuss solute strengthening below. Unfortunately, there is no rigorous theory for the Hall-Petch scaling [309], much less its dependence on alloy chemistry. In light of the very strong HP effects in FCC HEAs, this is a topic that merits much more theoretical attention.

On the other hand, solute strengthening in dilute alloys has a long history dating back to work by Fleischer, Labusch, and others [235,310]. In these works, the general structure of the theories was established but the inability to capture solute/dislocation interactions at the atomic scale, the use of singular theories for the dislocation fields, and some issues of convergence necessitating arbitrary cut-offs, all made the models non-predictive. However, the general structure of the models, including strain rate and temperature dependence, was robust and could be used to rationalize experiments across a wide range of materials [311]. The theoretical issues were largely overcome in work by Leyson et al. [284,304,312], which achieved good parameter-free predictions of solute strengthening across a range of alloys and temperatures. A recent article summarizes the history and recent developments [313].

Building on the framework of the early solute strengthening theories, Toda-Caraballo et al. [306] adopted the general scaling of the Labusch model. The general form for the strength due to a single solute type  $i$  at concentration  $c_i$  was taken as

$$\sigma_{ss}(T=0) = 3Z\mu(\eta'_i + \alpha^2\delta_i^2)^{2/3}c_i^{2/3} \quad (3)$$

where  $Z$  is a constant,  $\mu$  is the shear modulus,  $\eta'_i = \frac{1}{\mu}\frac{d\mu}{dc_i}$  is the “modulus misfit” parameter  $3 < \alpha < 16$  is another constant, and  $\delta_i = \frac{1}{a}\frac{da}{dc_i}$  is the “size misfit” parameter. A temperature dependence (but not strain-rate dependence) was added based on other literature work, so that

$$\sigma_{ss}(T) = 3Z\mu(\eta'_i + \alpha^2\delta_i^2)^{2/3}c_i^{2/3}e^{-mKT/W_0} \quad (4)$$

with  $m=25$  and  $W_0$  an energy associated with a solute/edge-dislocation binding energy. For a multicomponent HEA system, these authors further adopted the strength “mixture rule” derived by Labusch to yield

$$\sigma_{ss}(T=0) = 3Z\mu\left(\sum_i c_i(\eta'_i + \alpha^2\delta_i^2)\right)^{2/3} \quad (5)$$

Various approximations were then used to estimate the modulus and size misfit parameters. In the HEAs, the average atom spacing  $s$  was assumed to be of the form  $s = \sum_{ij} s_{ij} c_i c_j$  with coefficient  $s_{ij}$  the spacing between atoms of type  $i$  and  $j$  obtained by fitting to alloy lattice constants  $a$  versus composition. The meanings of  $m$  and  $W_0$  in the context of HEAs were not clearly elucidated. The authors then applied the model to the few FCC materials where Hall-Petch scaling had been measured and could be subtracted. The shear modulus was obtained from the rule-of-mixtures using the elemental shear moduli, evidently without regard for the elemental crystal structures. They studied one temperature and thus the temperature-dependent term in Eq. 4 could be absorbed into the fitting parameter  $Z$ , while  $\alpha=16$  was assumed. The results are shown in Fig. 26. The general trend of the data is captured well. However, the predictions are usually too low with typical deviations in the range of 25%. The authors then proceeded to make additional predictions for other FCC and BCC systems, noting that (i) the contribution from the Hall-Petch effect are not included in the prediction and (ii) converting measured hardness to yield stress by dividing by a factor of 3 is not valid when there is significant work-hardening (see above), as observed in the FCC alloys. In general, the deviations between model and experiment in these cases were rather larger, which is not surprising given the additional factors contributing to strength. The model also does not address the well-established temperature- and strain-rate dependence of the strength.

A solute strengthening theory for HEAs was then rigorously derived by Varvenne et al. [237], building upon the predictive dilute-solution model of Leyson et al. [284]. The key insight in moving

from dilute to concentrated solutions came from the concept of the homogenized alloy, i.e., the existence of a hypothetical average matrix material. The theory considers the dislocation in the average matrix material, and considers each elemental addition of the alloy to be a solute addition into the average matrix. The solute/dislocation interaction energies that enter the theory are then those of the solute/dislocation interaction in the average matrix. The structure of the dislocation in the homogeneous matrix material is thus preserved, e.g., dissociation into two partial dislocations separated by a stacking fault in an FCC alloy, and the dilute theory needs to be generalized only to properly include the random statistics at higher concentrations. Because full solute/dislocation interaction energies are difficult to determine in real materials (as compared to simulations), Varvenne et al. then also simplified the theory by treating only the elastic interaction between the solute and edge dislocation, dominated by the solute misfit volumes in the alloy. They were then able to reduce the full theory to an analytical form. Furthermore, they were able to demonstrate that, for the FCC case, the partial dislocation spacing  $d$  had no effect on the strengthening for  $d>7b$ , which holds in most FCC metals and alloys (Al is an exception). The core spreading of the individual partial dislocations has some effect, but Varvenne et al. showed that this spreading was expected to be relatively constant across different materials. The resulting analytic theory is

$$\sigma_{ss}(T, \dot{\epsilon}) = \sigma_{y0} \left[ 1 - \left( \frac{kT}{\Delta E_{b0}} \ln \frac{\dot{\epsilon}_0}{\dot{\epsilon}} \right)^{2/3} \right] \quad (7a)$$

$$\sigma_{y0} = 0.051\alpha^{-1/3}\mu(T) \left( \frac{1+\nu}{1-\nu} \right)^{4/3} \left( \sum_i \frac{c_i \Delta V_i^2}{b^6} \right)^{2/3} \quad (7b)$$

$$\Delta E_{b0} = 0.274\alpha^{1/3}\mu(T) \left( \frac{1+\nu}{1-\nu} \right)^{2/3} \left( \sum_i \frac{c_i \Delta V_i^2}{b^6} \right)^{1/3} \quad (7c)$$

where  $\alpha = 1/8$  is a coefficient related to the dislocation line tension  $\Gamma = \alpha \mu b^2$ ,  $\mu(T)$  is the alloy shear modulus at temperature  $T$ ,  $\nu = \nu(T)$  is the Poisson ratio, and all the numerical factors are entirely derived. The reference strain rate  $\dot{\epsilon}_0$  in Eq. 7a can be estimated,  $\dot{\epsilon}_0 \approx 10^4 - 10^5$ /s and only enters in the logarithmic term. There are thus no parameters in this model, only material properties, although this analytic version assumes elastic solute/dislocation interactions.

The form of the derived Eq. 7b is now seen to rationalize the ad-hoc Eq. 5. The misfit terms are similar because  $\frac{\Delta V_i}{b^3} \propto \delta_i$ , the elastic moduli correspond to those of the “average” matrix, and there is some numerical prefactor that is connected to the underlying dislocation structure. But Eq. 7 provide the full temperature- and rate-dependence with no fitting parameters, and all numerical constants are outcomes of the model or are material properties. The derivation further reveals that Eqs. 7 are applicable only when (i) elasticity interactions dominate, (ii) the dissociation distance of the partials is sufficiently large, and (iii) the local variations of the misfit volumes and possible local deviatoric misfit strains that give rise to additional fluctuations can be ignored. The full theory accounts for all of these factors but it is difficult to measure the required material inputs (solute/stacking fault interactions in the random alloy; distribution of misfit strain tensors, etc.) in the true random alloy. Thus Eq. 7 are useful for general assessment of strengthening but may not be quantitatively accurate in all applications. Eq. 7 apply independent of concentrations and numbers of components and so are not specific to HEAs. HEA strengthening is thus distinguished from solute strengthening in standard alloys in that HEAs are 100% solute strengthened (every atom is a solute type in the alloy) but with relatively small misfit volumes while standard alloys typically consist of a low concentration of solutes

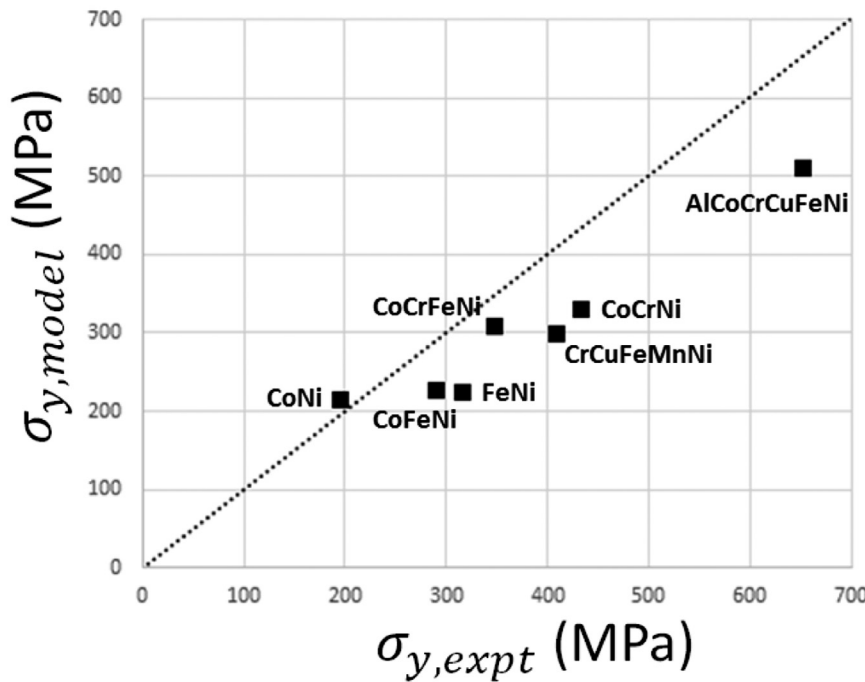


**Fig. 26.** Initial yield strength, prediction vs. experiment, for the alloys shown. Data replotted from [306].

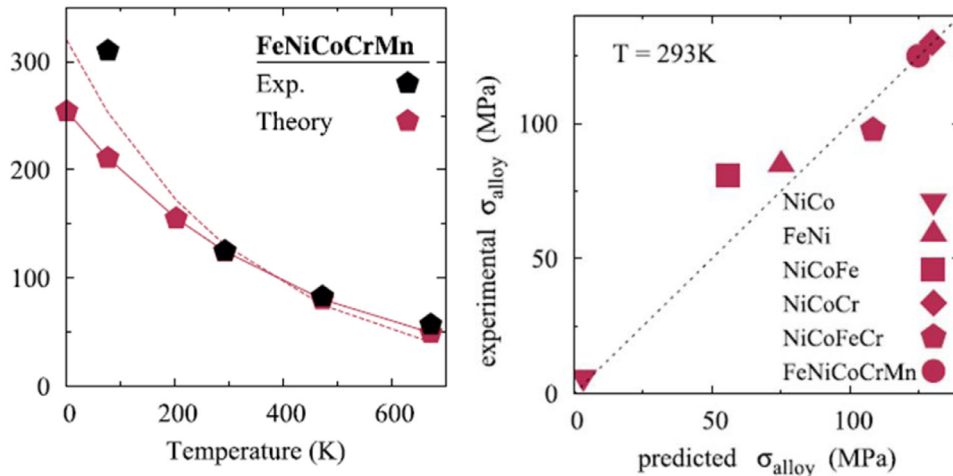


**Fig. 27.** (a) Solid-solution (non-Hall-Petch) contribution to initial yield strength vs. temperature for the FCC CoCrFeMnNi HEA, as predicted (red symbols) and as measured (black symbols); the dashed line indicates predictions using a slightly different value of the dislocation line tension. (b) Non-Hall-Petch contribution to the initial yield strength, experimental versus predicted, for a range of equicomposition alloys in the Co-Cr-Fe-Mn-Ni family at  $T = 293\text{ K}$ . Reproduced from [237]. (For interpretation of the references to color in this figure legend, the reader is referred to the web version of this article.)

(non-matrix atoms) but with relatively larger misfit volumes in the matrix.

Applications of the Varvenne et al. elasticity model (Eq. 7) to date show that this parameter-free analytic model captures the strength magnitudes and trends across alloys of the solid-solution contribution to yield strength in FCC HEAs. Using measured elastic constants and misfit volumes derived from Vegard's law applied to the Ni-X ( $X=\text{Cr, Co, Fe}$ ) binary alloys and Mn-containing HEAs, predictions for the solid-solution contribution to the strength in the Co-Cr-Fe-Mn-Ni family of FCC alloys were made as shown in Fig. 27a,b. Extending the model to the Co-Cr-Fe-Mn-Ni-Al family, with the Al misfit volume obtained from alloy atomic volumes and the elastic constants obtained by scaling Ni-Al elastic constants, the additional strength due to Al additions was predicted to be in good agreement with experiments [314]. The full model was used to predict the  $T=0\text{ K}$  strengths measured in atomistic sim-

ulations of the model Cr-Fe-Ni system, again with good agreement across a range of alloys [237]. The model was most recently applied to the RhIrPtPdCuNi noble metal HEA using Vegard's law for the misfit volumes (all elements crystallize in FCC) and a rule-of-mixtures for the elastic constants [85] leading to a predicted yield strength at  $T=300\text{ K}$  and strain rate  $10^{-4}/\text{s}$  of 520–580 MPa as compared to the single reported value of 526 MPa [315]. To demonstrate a fully-computational prediction with no experimental input, full DFT computations of the misfit volumes, elastic constants, and stacking fault energy for RhIrPtPdCuNi were computed, and the fully-predicted yield strength for this elastically anisotropic material is 583 MPa [307] again in very good agreement with experiment, although more experiments are needed.

Finally, recent experiments have demonstrated that the intrinsic solid-solution strengthening at room temperature and standard strain rate of the 3-component NiCoV alloy is far stronger,

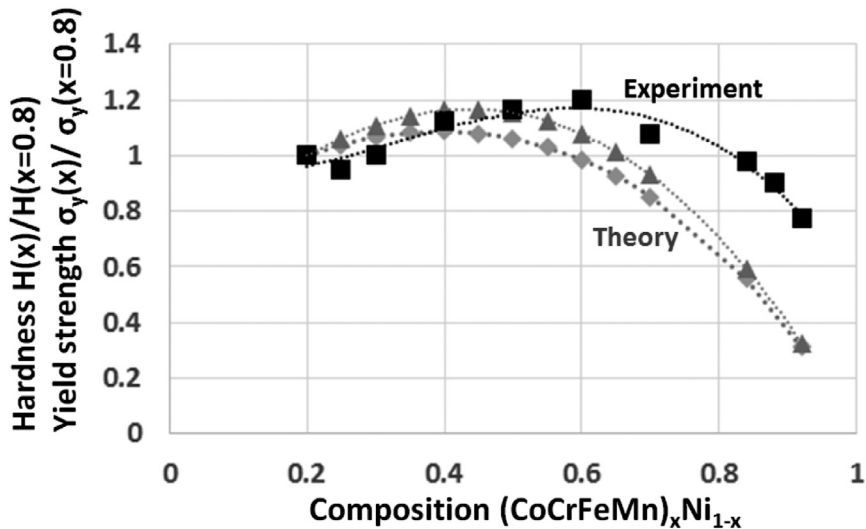


**Fig. 28.** Normalized yield strength and normalized hardness versus composition in  $(\text{CoCrFeMn})_x \text{Ni}_{1-x}$ , as measured (black squares), as predicted by the theory of Varvenne et al. (gray diamonds), and as predicted by the theory with the estimated changes in alloy elastic moduli (gray triangles). Data taken from [316].

383 MPa, than any previous alloys in the Cantor-alloy-type Co-Cr-Fe-Mn-Ni family including NiCoCr [303]. Application of the Varvenne model using (i) the atomic volumes of Ni and Co given in Varvenne et al., (ii) the effective FCC V atomic volume of  $13.72 \text{ \AA}^3$  determined from the DFT-computed misfit volume of V in NiV, and (iii) the reported isotropic elastic constants  $\mu=72 \text{ GPa}$  and  $v=0.334$ , immediately leads to a predicted strength of 393 MPa, in very good agreement with the experiments [354]. There is no need to invoke the notion of a Peierls friction stress due to a narrow dislocation core nor the vague notion of “lattice distortions” associated with varying atom spacings observed in DFT computations of NiCoV, neither of which provides any actual prediction. Here, it is seen that the strength derives directly from the high misfit volume of V in the FCC crystal structure.

Laurent-Brocq et al. fabricated and tested the  $(\text{CoCrFeMn})_{1-x} \text{Ni}_x$  alloys for  $0.2 < x < 0.96$  [316]. Importantly, they first showed that Vegard’s law is not accurately followed over the full range of  $x$ . Measuring hardness, they then showed that there is a maximum hardness at  $x=0.4$ , away from the equiatomic composition. They applied the Varvenne et al. model with the original elemental volumes, Vegard’s law, and the  $x=0.2$  elastic modulus to compute the normalized strength  $\sigma_y(x)/\sigma_y(x=0.2)$  versus  $x$ . The predictions roughly matched the measured normalized hardness  $H(x)/H(x=0.2)$  (see Fig. 28). We recall that the comparison with hardness implicitly assumes that the work hardening is similar for all  $x$ , which may not hold. Using the estimated small trends in elastic moduli, which suggest that  $x=0.4$  has the highest modulus, leads to slightly modified predictions that are in slightly better agreement with the normalized hardness (Fig. 28). The agreement between theory and experiment is encouraging. However, the uncertainties in misfit volumes, since Vegard’s law was shown not applicable, remains a significant issue for application of the Varvenne et al. theory while the comparisons of hardness and yield strength make further study essential. Laurent-Brocq and coworkers have extended this type of study to all of the  $(\text{ABCD})_{1-x} \text{Ex}$  combinations in the Cantor alloy family, demonstrating broad agreement in the correlation between measured hardness and predicted strength [317].

Recall our assertion that the experimental Haasen plot, and associated activation volume for plastic flow, reveals that operation of relatively standard dislocation-based plasticity mechanisms. Any successful model or theory should thus predict the activation vol-

ume and its evolution with plastic strain. Above, we analyzed models and a theory for the initial yield stress only, and therefore we can only investigate the initial activation volume. The only result above that is temperature- and rate-dependent is the theory of Varvenne et al. [237]. Fortunately, the activation volume is defined by Eq. 2 and requires no additional theory or inputs, merely manipulation of the strength versus temperature and strain rate (Eqs. 7). Using the same inputs as those for the strength predictions in Fig. 27, the predicted value of  $MkT/V$  for the CoCrFeMnNi Cantor alloy at temperature  $T=293 \text{ K}$  is shown in Fig. 23 as the red circle. The value differs from experiments by approximately 1.7, but such a deviation is comparable to those obtained for standard dilute alloys using the same underlying theory [304,318]. In the Varvenne et al. theory, the activation volume is related to the product of two underlying length scales of the dislocation in the random HEA alloy, a wavelength and amplitude describing the typical dislocation configuration in the random alloy. The agreement between theory and experiment for the Cantor alloy indicates that the length scales predicted by the theory of Varvenne et al. are those pertinent to the thermal activation of dislocations in the real alloy. The activation volume has not been measured in other FCC alloys. Thus, this is the only comparison possible at the present time. Future theories should aim at predicting the activation volume at initial yield as a means of further validation of the theories.

Contemporaneous with the development of a predictive theory for yield strength, some workers sought correlations between strength and other measurable or computable quantities. As discussed in Section 2, individual atoms do not sit exactly at the lattice sites of the underlying crystal structure. Since these distortions can be viewed as “defects” relative to the perfect lattice, it is theoretically feasible to envision that a dislocation, which is strictly defined with respect to the perfect lattice structure, will interact with such atomic-scale distortions in some manner. This suggests a correlation between atomic-scale distortions and yield stress, although no theory exists for such a direct connection.

The above idea was pursued primarily by Okamoto et al. [319] and Oh et al. [320]. Okamoto et al. painstakingly measured the picometer-scale atomic distortions in the Cantor alloy and computed via DFT the atomic distortions in various other equicomposition alloys in the Co-Cr-Fe-Mn-Ni family. They then presented a correlation between the estimated/extrapolated  $T=0 \text{ K}$  initial

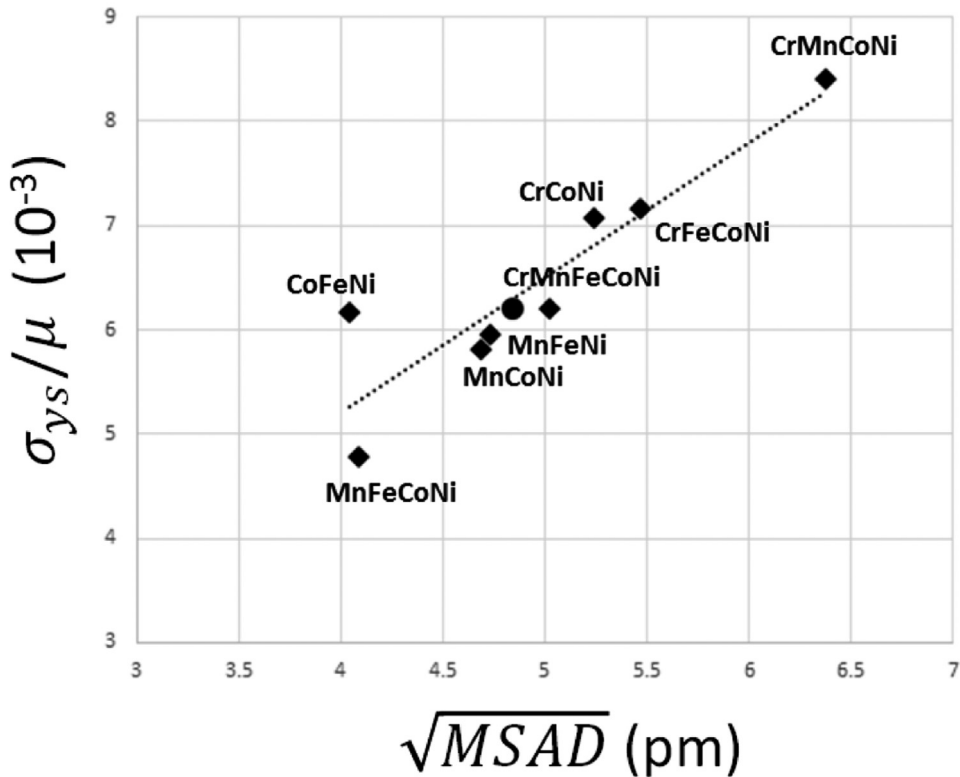


**Fig. 29.** Measured normalized initial yield strength (extrapolated to  $T = 0$  K) versus root mean square atomic displacement, as measured experiment (black circle, for CoCrFeMnNi) or as predicted by DFT (black triangles). Data replotted from [319].

yield stress, extrapolated from the measured temperature dependence, and the square root of the overall mean-square atomistic distortion (measured or computed). The authors speculated that, along the lines of solute strengthening, the alloy strength might be related to both alloy modulus and the misfit/distortion measure, and so the correlation was made using the dimensionless quantity (yield strength)/(alloy shear modulus) as shown in Fig. 29. The yield strength used in the comparison included a contribution from the Hall-Petch strengthening (see Eq. 1), which should have been subtracted in principle but is not known accurately for all the alloys. However, this deviation may not be quite as crucially important at  $T=0$  K as at higher  $T$ . For instance, the HP contribution is  $\sim 140$  MPa for the Cantor alloy while the extrapolated  $T=0$  K yield stress is  $\sim 589$  MPa, so the HP contribution is 25% of the total strength and the correlation may thus remain reasonable. In general, the correlation in Fig. 29 is encouraging. The correlation was recently extended with the addition of the NiCoV alloy [303]. However, the lack of a connection to a specific mechanism and theory remain a concern. Furthermore, all of the non-HP contributions to these alloy strengths can be predicted well with the theory of Varvenne et al. Finally, the measured activation area in the Cantor alloy of  $\sim 70 b^2$  at  $T=77$  K [100] indicates that the strengthening is not controlled by the individual atomic-scale fluctuations but rather some collective fluctuations, a key feature of the Varvenne et al. theory.

In an attempt to understand the correlation in Fig. 29, Noehring et al. [321] postulated that the root mean square (RMS) magnitude of the microdistortions is correlated with the misfit volume parameter entering the simplified Varvenne et al. theory; this would explain the correlation between micro-distortions and yield strength. The idea is that each atomic solute creates a distortion field around it, due to its misfit within the average alloy. Focusing on a given lattice point, the distortion at that lattice point is

the vector sum of the misfit distortions at that point caused by all the surrounding solutes at all other lattice points. The average distortion must be zero, but there is a distribution and the RMS distortion is the microdistortion. Analyzing this mathematically and then computing the required quantities from simulations on the model Cr-Fe-Ni ternary family, Noehring et al. found the ratio

$$\frac{\text{RMSmicrodistortion}}{b} = 1.2 \pm 0.2, \text{ i.e., within } \pm 15\%, \text{ over a wide range}$$

$$\left( \sum_i \frac{c_i A V_i^2}{b^6} \right)^{\frac{1}{2}}$$

of composition space. A similar result was obtained for a model Nb-Ta-V BCC alloy. This analysis provides one mechanistic rationalization of the correlation in Fig. 29.

In summary, it is now understood that the yield strength in FCC HEAs arises mainly from a combination of solute strengthening and Hall-Petch grain size effects. Historical solute strengthening models were first adapted to the HEA case, and a full theory then developed. The full theory when reduced to elasticity has the form of the previous adapted models, but without fitting parameters. Applications of the reduced theory to date have shown good quantitative agreement with experiments. However, simple methods to estimate misfit volumes may fail in some alloys, and so this is a possible limitation of the reduced theory. All theories and models to date neglect the additional complicating factors of specific solute-solute interactions (even in the random alloy) and short-range order (driven by any solute-solute interactions). If these exist in an alloy, the existing theories and models will be less accurate. These issues are important, and require further theoretical attention, as discussed below.

### 3.3.2. BCC alloys

We now turn to strengthening in BCC HEAs. A Labusch-type solute strengthening model was also applied to interpret initial yield strengths in BCC HEAs [46,322,323]. Translated into the notation of

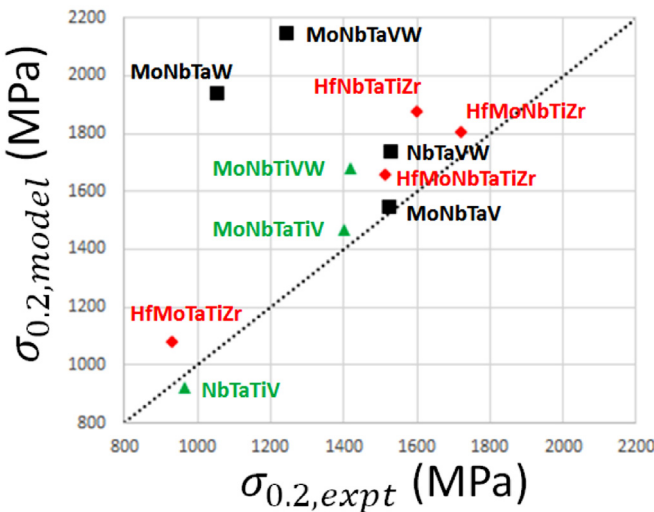


**Fig. 30.** Initial yield stress, prediction vs. theory, for a range of BCC HEAs. Data obtained from [46,322,323].

Section 3.3.1, the model for the BCC alloys was taken to be

$$\sigma_{ss} = \sigma_0 + 3Z\mu \left( \sum_i (\eta'_i + \alpha^2 \delta_i^2) c_i \right)^{2/3} \quad (8)$$

where  $\sigma_0 = \sum_i c_i \sigma_{0,i}$  was added as a rule-of-mixtures “Peierls stress” contribution using the measured elemental yield stresses  $\{\sigma_{0,i}\}$  because the elemental BCC Peierls stresses are large. The modulus and misfit parameters were taken as rule-of-mixtures-type values associated with pairs of elements, and the parameters  $3Z \approx 0.04$  and  $\alpha=9$  were used, stated as a balance between screw and edge dislocation contributions. Both tensile yield stress and Vickers Hardness were measured experimentally, and a ratio of  $\frac{H}{\sigma_{ss}} \approx 3 - 3.3$  was demonstrated, as mentioned above, consistent with the high initial yield stresses relative to the work-hardening rate in these BCC HEAs. The predictions for yield stress versus experiments performed at room temperature on as-cast microstructures (primary dendrites of  $\sim 200 \mu\text{m}$  and arm spacings of  $\sim 30 \mu\text{m}$ ) are shown in Fig. 30. Generally quite good agreement is obtained, with the model typically 0–18% too large. However, there are several significant deviations where the model is much too high by  $\sim 900 \text{ MPa}$ , or  $\sim 80\%-90\%$ . These are also predicted to be by far the strongest alloys yet in fact are among the weakest. The use of this model for design may thus be questionable.

The contribution of  $\{\sigma_{0,i}\}$  in Eq. 8 varies from  $\sim 270$ – $400 \text{ MPa}$  for the Mo-Nb-Ta-Ti-V-W family shown, so the solute strengthening contribution generally dominates. This term, the Peierls stress of the pure element, arises physically in the elemental metal due to double-kink nucleation along screw dislocations, but screw control would normally imply a much lower value of  $\alpha=2$ . More importantly, in the classic model of flow in BCC alloys [324], it is understood that the double-kink nucleation ceases to be the controlling factor. Hence, this term in Eq. 8 should probably not appear. If this term is not included, then the deviations with experiment across this set of alloys would range from  $-33\%$  to  $+46\%$ . The model does not directly address any influence of the as-cast microstructure, nor established temperature- and strain-rate dependence of the flow stress. Since these certainly differ from alloy to alloy, this may account for the deviations between model and experiment. The authors further report that upon annealing, the strength of the HfNbMoTiZr alloy decreases from  $1719 \text{ MPa}$  to  $1575 \text{ MPa}$ , while the model prediction remains at  $1804 \text{ MPa}$ . On the other hand, the authors also applied the model to the

HfMo<sub>x</sub>NbTaTiZr alloy and found agreement to within 15% across a range of  $x$ ; this is impressive. Overall, the success of this solute-strengthening-type model based on misfit volumes is somewhat surprising. As noted earlier, BCC yield strengths in dilute alloys at this temperature are universally believed to be controlled by the effects of solutes in impeding kink glide of screw dislocation [324,325], for instance Mo-Pt and Mo-Re [326], whereas Labusch-type solute strengthening is typically controlled by non-screw dislocations. Nonetheless, the success is intriguing.

Although based on a simple model and with some arbitrary parameters and rule-of-mixtures assumptions, the reasonable success (albeit with some notable failures) of the solute-strengthening model for these BCC HEAs suggests that they are somewhat different than BCC dilute alloys in that dominance of the screw dislocation strengthening may be lost. Such a radical concept is supported by the MD simulations of Rao et al. on a model BCC Co<sub>16.67</sub>Fe<sub>36.67</sub>Ni<sub>16.67</sub>Ti<sub>30</sub> alloy [327]. They compared the behavior of screw and edge dislocations in the true random alloy to their counterparts in the “average atom” alloy. At  $T=0 \text{ K}$ , the screw dislocation in the random alloy is strengthened by a factor of  $\sim 2x$  relative to the “average atom” alloy whereas the edge dislocation is strengthened by a factor of  $\sim 50x$ . Most importantly, the ratio of screw to edge strength in the random alloy is only  $\sim 2.5$ . Since the screw strength in the simulation of a random alloy may be enhanced by unphysical restructuring of the core due to inadequacies of the interatomic potential, an issue not relevant for edge simulations, the similarity of edge and screw strengths suggests the possible applicability of solute strengthening concepts based on the edge dislocation in BCC alloys.

Courty et al. recently presented a model for strengthening versus temperature that has the general structure of Eq. 8 [328]. With the common experimental observation that BCC HEAs shows a plateau in strength starting around  $600\text{C}$ , they postulated that the strength was the sum of (i) an athermal contribution of a form similar to the second term in Eq. 8, but with a generalized misfit quantity following the form of Toda-Caraballo [306] and (ii) a thermal contribution attributed to double-kink nucleation typical of elemental and dilute BCC alloys that replaces the  $\sigma_0$  in Eq. 8. The thermal contribution was fit to the data for each individual alloy. Parameters for the athermal contribution were fit to the plateau data across a range of HEAs. With such extensive fitting, good agreement with experiments could be achieved. However, adding strengths that are usually separately associated with screw and edge dislocations, respectively, and assuming an athermal stress related to solute mechanisms but without any estimate of the activation barrier, are not well-justified. The alloy-specific fitting of the thermal contribution also seems to prevent predictions on new alloys. Thus, pursuing more mechanically-based models is needed for a robust and reliable predictive capability.

Toward that goal, and retaining the classical view that screw strengthening in BCC metals is the dominant factor, Rao et al. [293,329] adapted the Suzuki model [324,325] to the HEA case. The dominant strengthening in the Suzuki model is the inhibition of the glide of kink along a screw dislocation by the solutes. Rao et al. computed the strength of each individual solute type embedded in the average alloy matrix using the Suzuki model and then combined the results for each solute into an overall strength of the HEA. Because the Suzuki model typically predicts that strength is linear in solute concentration, except at low temperatures, the prediction of Rao et al. reduces almost to a rule-of-mixtures model. Rao et al. obtained the solute/screw dislocation interaction energies for the Suzuki model by using the Zhou et al. interatomic potentials, inserting each solute into the atomic site at very core of the screw dislocation predicted by the average alloy potential. The predictions of yield strength at  $T=300 \text{ K}$  across a range of BCC HEAs were compared with experimental values deduced from

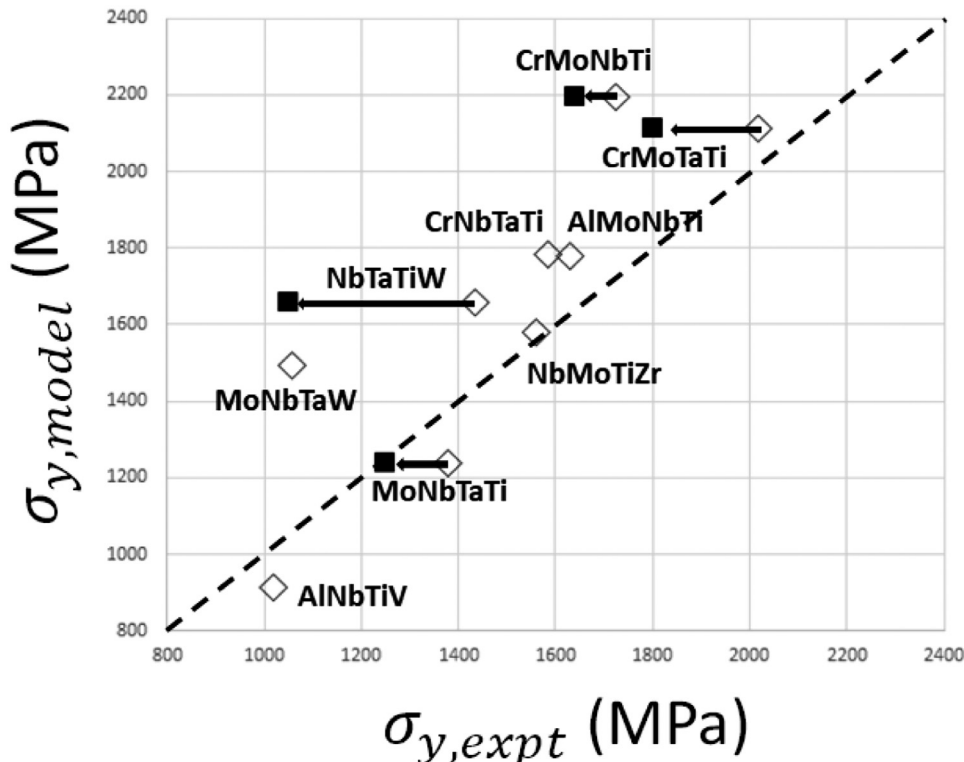


**Fig 31.** Predicted versus experimental yields stress at  $T = 300$  K for various BCC HEAs. Predictions are made using the model in [329]. Experiments shown as open diamonds were converted from measured hardness values as  $\sigma_y = H/\beta$  with  $\beta=3.2$ . Experiments shown as solid squares were obtained from uniaxial compression tests on annealed single-phase alloys [328], and are uniformly lower than the values estimated from the hardness data. Dashed line indicates one-to-one correspondence. Adapted from [329] and augmented.

measured hardness, and the results are shown in Fig. 31 [329]. The agreement is generally very good. However, subsequent compression tests on those composition that remain single phase after annealing were recently reported [328], and are much lower than extrapolated from the previously-reported hardness. The corrected comparison for these alloys is also shown in Fig. 31, and shows that the theory prediction is systematically rather higher than experiments. The same model was also applied to the TiNbZr alloy, however, and showed good agreement with uniaxial compression tests at  $T=300$  K [293].

One issue with the Suzuki model is that, while it includes strengthening due to jog formation, the temperature dependence of the jog mechanism scales with the temperature dependence of the kink glide motion. Kink glide motion then always dominates the predicted strengthening at all temperatures. Experiments in BCC alloys, and especially at higher concentrations and higher temperatures, identify the strengthening as dominated by the jog formation. As a consequence, the Rao et al. model does not accurately capture the high strength retention of TiNbZr at 873 K. Rao et al. proposed that additional strengthening due to interstitial elements might be contributing. A new model for screw motion in BCC HEAs has been developed by Maresca and Curtin [330] that incorporates the same screw-strengthening mechanisms but in an entirely different analysis that yields high-temperature strengthening as controlled by the jogs. Application of that model to traditional non-dilute Nb-Mo binary alloys shows good agreement with experiments over a range of concentrations and temperatures. Approximate application to the Ti-Nb-Zr family showed good agreement up to 900 K. However, at even higher temperatures (1073K–1273 K), the measured strength of TiNbZr decreases dramatically. The mechanisms for this decrease are presumably related to vacancy-mediated processes that defeat the jog strengthening starting at some characteristic homologous tempera-

ture  $T/T_m$ ; while well-established in other metals, this process has been recently studied by [331]. It is unclear how this mechanism would be accurately reflected within the context of the Suzuki model, where kink glide strengthening is always dominant, but it could be combined with the new screw dislocation model of Maresca and Curtin [332].

Deviating from the traditional perspective of screw dominance in BCC alloys, Maresca et al. [332] have recently considered the strengthening of edge dislocations in BCC HEAs as a possible reason for the high-temperature strength in BCC HEAs. The analysis is conceptually similar to that of Varvenne et al. although differing in detail. For instance, the edge dislocations in BCC are not dissociated into partials, but are spread along the glide plane. However, strengthening remains dominated by the interaction of the edge dislocation with the misfit volumes of the solutes. By examining many different alloys in the Mo-Nb-Ta-V-W family using a detailed theory, they found that an analytic theory, similar to that of Eqs. 7 for FCC alloys, agreed well with the predictions of the full theory across many model BCC HEAs alloys. The final analytic results could be reduced to

$$\sigma_{y0} = 0.0407\alpha^{-1/3}\mu(T)\left(\frac{1+\nu}{1-\nu}\right)^{4/3}\left(\sum_i \frac{c_i \Delta V_i^2}{b^6}\right)^{2/3} \quad (9a)$$

$$\Delta E_{b0} = 2.00\alpha^{1/3}\mu(T)\left(\frac{1+\nu}{1-\nu}\right)^{2/3}\left(\sum_i \frac{c_i \Delta V_i^2}{b^6}\right)^{1/3} \quad (9b)$$

with the accuracy of the coefficients being  $\pm 10\%$  relative to results from the full model and with  $\alpha = 1/12$  a line tension parameter. The finite-T, finite-strain rate strength is accurately captured by a single fitted formula that captures the precise low-T and high-T

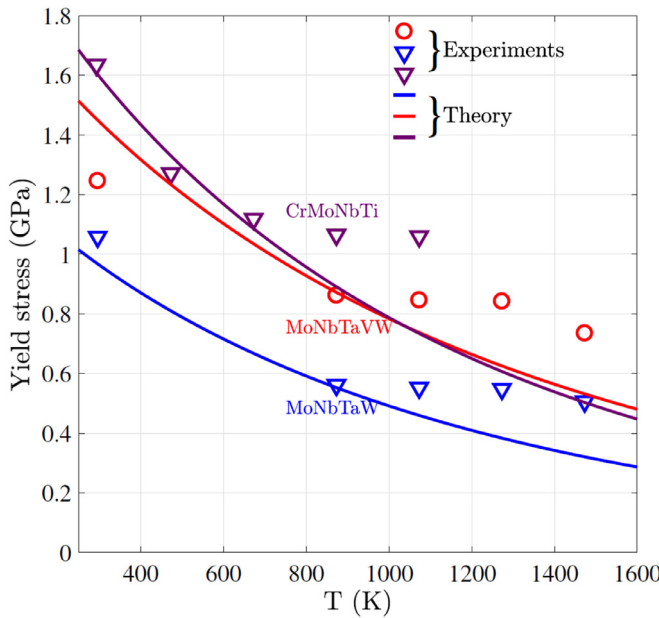


**Fig. 32.** Yield strength versus temperature as predicted by the parameter-free edge dislocation model of Maresca and Curtin [332] for three BCC HEAs. The theory captures the overall magnitude of strengthening versus alloy composition, although does not predict the plateau in strength in the range 900–1200 K that is typically observed in this class of alloys.

limits derived by Leyson et al. [318] as

$$\sigma_{ss}(T, \dot{\varepsilon}) = \sigma_{y0} \exp \left[ -\frac{1}{0.55} \left( \frac{kT}{\Delta E_{b0}} \ln \frac{\dot{\varepsilon}_0}{\dot{\varepsilon}} \right)^{\frac{1}{11}} \right] \quad (9c)$$

Involving only elastic constants and misfit volumes, the edge theory avoids the many complications that are involved in modeling screw dislocations in BCC alloys. Furthermore, the relevant properties can be computed or estimated with very good accuracy, especially since Vegard's law is a very good approximation in this family of alloys. As for the FCC case, Eqs. 9 rationalize the model of Eq. 8 without the questionable addition of the  $\sigma_0$ Peierls stress term.

The predictions of Eqs. 9 for the MoNbTaW and MoNbTaVW alloys [10] up to  $T=1600$  C and the CrNbTaTi alloy [328] up to 800 C are shown in Fig. 32. The agreement, with no adjustable parameters, is fairly good over the entire range, although the theory does not capture the "plateau" in flow stress around 900–1200 K and so is generally lower than experiments at higher  $T$ . Of note is the prediction that the V-containing MoNbTaVW alloy is much stronger than the MoNbTaW alloy, which is attributed to the rather smaller atomic volume of V as compared to Mo, Nb, Ta, and W. Furthermore, the CrNbTaTi alloy is even stronger due to the even smaller atomic volume of Cr as compared to V although the loss of high-modulus W reduces the strength. Application of the full model to two other alloys in the Mo-Nb-Ta-V-W family studied by Gao et al. at  $T=300$  K was also good. Experimental evidence for the dominance of edge dislocations, as assumed in this theory, has not yet been obtained. However, mechanistically, it seems unlikely that screw dislocations can sustain the high strengths at high temperature found for these alloys. If the control of strength in BCC HEAs by edge dislocations can be further established, this would be one case where the HEA behavior differs entirely from that of dilute alloys.

### 3.4. Additional strengthening mechanisms

#### 3.4.1. Variations in local stacking fault energy

Early atomistic calculations of dislocations in model random FCC alloys observed that the partial dislocation spacing varied considerably (Fig. 33a) [246,302]. This suggested that local composition variations correspond to local variations in the stacking fault energy. Local variations in the stacking fault energy correspond to local variations in the stacking fault force acting on the partial dislocations. It was thus speculated that these forces might pin the dislocation, or equivalently that the partial dislocations would seek regions of low-stacking fault energy and avoid regions with high stacking fault energy. Computing the local stacking fault energy by defining a local concentration around an individual atom on the slip plane, a map of estimated local stacking fault energy can be created (Figs. 32b–33b). Relaxation of a dislocation inserted into the random alloy then allows us to probe correlations of dislocation position and structure vs. local stacking fault energy. One must keep in mind, however, that the dislocation is interacting with all the atoms in the system, not only those on either side of the stacking fault. A typical example is shown in Fig. 33b for a model FCC Fe<sub>70</sub>Cr<sub>20</sub>Ni<sub>10</sub> stainless-steel-type material, where common neighbor analysis is used to approximately identify the dislocation core. The partial dislocations are indeed slightly wavy, and tend to avoid regions with high stacking fault energy. However, since the dislocation has some line tension, it cannot become arbitrarily wavy. The dislocation configuration is thus a balance between local potential energy fluctuations (here only the stacking fault energy is shown) versus line energy. The dislocation adopts a wavy length scale that minimizes the total energy.

Motion of a dislocation through a system with stacking fault variations at a specified length scale was studied by [333]. Fig. 33c shows an example where the average stacking fault energy (SFE) is 127.1 mJ/m<sup>2</sup> with a standard deviation of 39.1 mJ/m<sup>2</sup> over a characteristic length scale of 3.2 nm, at zero stress and an applied shear of 195 MPa. The dislocation is wavy and pinned by the regions of high SFE. Thus, it is clear that the SFE variations can provide strengthening. It is important to note that, in a random alloy, there are fluctuations in stacking fault energy over all scales. The dislocation thus presumably selects a scale through minimizing the total energy; there is no single pre-determined scale of stacking fault energy fluctuations, as suggested by Fig. 33c. A theory could be developed for the minimization of the total dislocation energy due only to stacking fault energy variations, from which a strength could be predicted. However, the stacking fault energy is only a subset of the total dislocation/solute interactions and is already included in the full theory of Varvenne et al. [237] (but not in the reduced theory of Eqs. 7 based on elasticity). Therefore, focusing on the stacking fault energy alone likely neglects important additional contributions (misfit volume and core interaction energies) to the strength.

In related work, Zhang et al. [334] developed a Peierls-Nabarro-type analysis to study the effects of the statistical distribution, spatial scale, and spatial correlations of the SFE on the motion of a dislocation. The first emphasis here was on general scaling of dislocation core structure and strength in one dimension. The second emphasis was on extending the model to consider spatially-correlated SFE energies as an approximation to short-range-order (SRO) and to straight dislocations in two dimensions. This work, while within a narrow scope, provides one mathematical approach to SRO, which is a critical under-studied issue in HEAs to date.

**Short-range order (SRO):** All of the modeling discussed above has assumed, implicitly or explicitly, that the alloys are perfectly random. By perfectly random, we mean that the probability of any one lattice site being occupied by a solute of type  $n$  is equal to the concentration  $c_n$  of solutes in the overall alloy. In alloys with SRO,

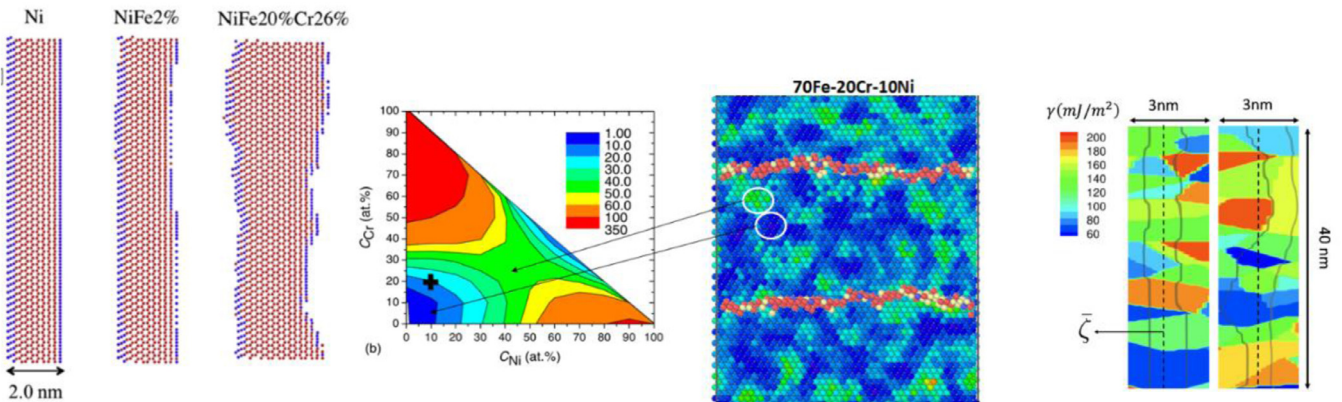


**Fig. 33.** (a) Atomistic prediction of FCC edge dislocation dissociation configurations in pure Ni, dilute Ni-Fe, and a medium-entropy-type Ni-Fe-Co alloy, showing the increasing variability in the stacking fault separation with increasing disorder [246]. (b) Atomistic map of the local stacking fault energy (SFE), as defined by the local composition around each atom, and the equilibrium configuration of an edge dislocation in the alloy, for a model Fe-Co-Ni stainless steel alloy. The local SFE varies considerably, and the partial dislocations adjust to minimize the total energy which involves contributions from the SFE (Varvenne et al., unpublished). (c) A dislocation moving through a pre-specified SFE field having characteristic mean, standard deviation, and length scale, both at zero stress (left) and applied stress (right), the latter indicating pinning by the SFE fluctuations [333].

the occupations of different sites are correlated and are described by appropriate statistical order parameters such as the Warren-Cowley SRO parameter. The theories further assume that there are no specific solute-solute interactions, even in the random alloy. SRO and solute-solute interactions are intertwined because it is the solute-solute interactions, even in the random alloy, that provide the thermodynamic driving force for the formation of SRO and, in many cases, long-range order.

Solute-solute interactions can be computed in the random alloy for systems using EAM interatomic potentials by employing the average alloy method (see, for example, [335]). Unpublished work shows that the solute-solute interactions among elements in the BCC family of Mo-Nb-Ta-V-W using the Zhou et al. EAM potentials are all quite small, on the order of 2 meV, supporting use of these potentials for the study of model random alloys without solute-solute interactions (even if such interactions exist in the real alloys). An excellent test system for solute-solute interactions is the FCC Ni-Al binary alloy, wherein first-neighbor Al-Al interactions are strongly repulsive (~0.25 eV). The effects of these interactions were first revealed by Rodary et al. [336,337] and found to be crucial to explain the strengthening at moderate Al concentrations (~15%). More recently, Antillon et al. have revisited the Ni-Al system using a different Ni-Al EAM potential with strong Al-Al repulsion, and simulated dislocation motion at different Al concentrations [338]. For Al concentrations of a few %, the role of these interactions is fairly small. At a concentration of 10%, the Al-Al repulsion becomes a major factor in the strengthening. Antillon et al. performed a wide range of analyses of their simulations to examine various scaling behaviors in the context of the Leyson et al. theory, but these are tangential to the present discussion. What is important about the studies of Proville et al. and Antillon et al. in the context of HEAs is that solute-solute interactions are important for strengthening only if they are quite strong (100 s of meV) and the concentrations rather high (10%–15%). HEAs certainly have the high concentrations, but the solute-solute interactions may be much smaller, consistent with the fact that HEAs can be fabricated using typical casting and annealing temperatures and times without decomposing into intermetallic phases.

Thermodynamic studies, both theory and experiment, suggest that many HEAs are metastable (for instance, see the extensive recent review by Ikeda et al. [339]). There is thus a driving force for phase separation, which is related to specific solute-solute interactions. Solute-solute interaction energies have been computed via DFT for a BCC HEA [340], and total DFT energy calculations that include solute-solute interactions have been used to evolve SRO in

both BCC [341] and FCC HEAs [342,343] using Monte Carlo methods. The occurrence of, and degree of, SRO depends on both temperature and time, making it difficult to directly connect these simulation studies to experimental processing. Mechanical properties of these HEAs with solute-solute interactions and/or SRO have not been studied extensively. Only a recent paper [343] has developed and used a DFT-calibrated semi-empirical potential for the Ni-Co-Cr system to examine mechanical properties. They report significant strengthening in the model NiCoCr alloy with increasing SRO, which certainly suggests that SRO requires attention. However, the solute-solute interactions that drive SRO in the model NiCoCr alloy (mainly Cr-Co attraction and Cr-Cr repulsion) must be validated, and the degree of SRO under realistic processing conditions must be better established.

Theoretically, modeling of strength in the presence of SRO has not been developed beyond the aforementioned study of Zhang et al. The statistical model of Varvenne et al. might be extendable to include non-random site occupancies according to specified SRO parameters, but no theory yet exists. On the other hand, the role of solute-solute interactions on strengthening in the random alloy is more amenable to theoretical treatment. Forthcoming work of Nag et al. (Nag et al., in preparation) introduces solute-solute interactions, and these create an additional source of fluctuations that contribute to the changes in dislocation energy as it glides through the random alloy. The solute-solute interactions can then be incorporated into the framework of Varvenne et al. and will lead to an increase in strengthening relative to the random alloys. These issues are probably the most critical issues pertaining to yield strength at the present time, and merit further study.

### 3.4.2. Twinning

As discussed earlier, twinning has been implicated as a mechanism for sustaining strain-hardening in FCC HEAs, leading to enhanced ductility. Thus, it is very valuable to understand whether or not twinning in HEAs differs from existing engineering alloys. Twinning is normally correlated with the stable stacking fault energy  $\gamma_{\text{ssf}}$ , or more precisely with the stable twinning fault energy  $\gamma_{\text{stf}}$  that is usually found to be  $\gamma_{\text{stf}} \sim \gamma_{\text{ssf}}/2$  in elemental FCC metals. Fig. 34 shows the experimentally measured twinning stresses for the elemental FCC alloys Au, Ag, and Cu versus stacking fault energy. Twinning is not observed in Ni, Al, Pd, or Pt, all of which have rather large stacking fault energies that suggest high twinning stresses, as indicated in the figure. Pb is excluded because reported results vary over a wide range. To rationalize this correlation, we consider several basic models. All are based on an initial

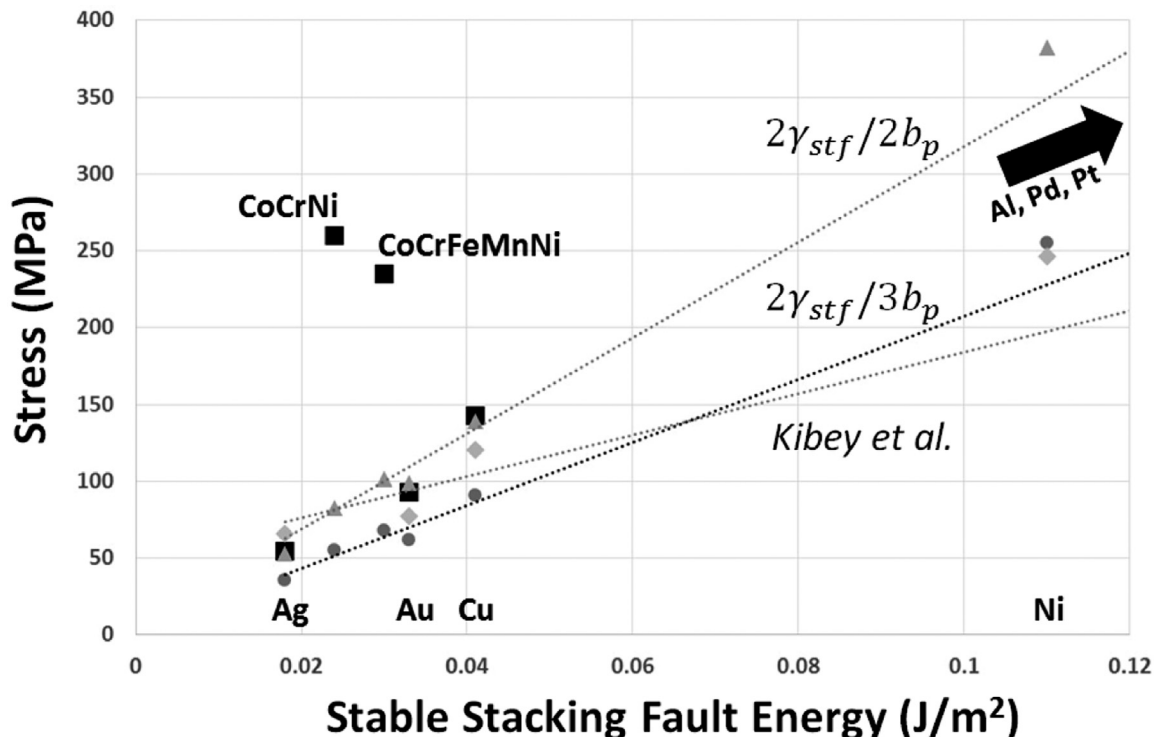


**Fig. 34.** Experimentally measured twinning stress versus stable stacking fault energy. Experiments (black symbols) and various theories (gray symbols, dashed lines) are shown; see text for discussion.

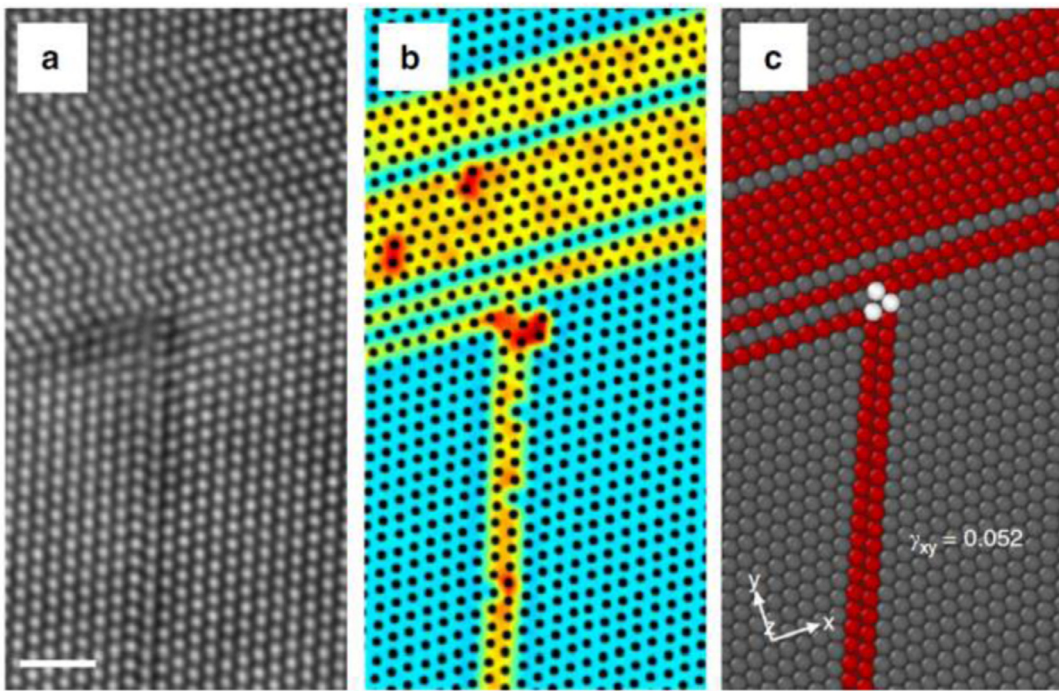
nucleus consisting of several partial dislocations of Burgers vector magnitudes  $b_p$  lying on adjacent slip planes to create multi-layer faults. The stress to move such a configuration is then a balance of the work done by the applied stress in moving the multiple  $b_p$  versus the energy cost of creating the fault surfaces that are left behind. These models are thus presumably lower bounds because they do not address how the initial nucleus is formed, nor interactions with the other dislocations necessary to create the nucleus. One model assumes the three-layer twin nucleus proposed by Mahajan and Chin [344], which then suggests  $\tau_{\text{twin}} = 2\gamma_{\text{stf}}/3b_p$ . A second model involves only a two-layer twin nucleus [Rao et al., unpublished], such that  $\tau_{\text{twin}} = 2\gamma_{\text{stf}}/2b_p$ . A third model [345] is based on the Mahajan nucleus but is more complicated and involves the unstable twinning energy. The agreement of all models is reasonable for the materials that show twinning (Au, Ag, Cu) and all models suggest high twinning stresses of Ni, Al, Pd, and Pt, at levels that exceed the typical accessible stress levels in these materials and thus consistent with the absence of twinning.

Fig. 34 also shows the experimental twinning stresses for both CoCrFeMnNi and CoCrNi, as indicated at the values of  $\gamma_{\text{ssf}} = 30 \frac{\text{mJ}}{\text{m}^2}$  and  $22 \frac{\text{mJ}}{\text{m}^2}$ , respectively, as deduced from TEM measurements of partial spacing using isotropic elasticity [154,257] (see Table 2). The HEAs clearly deviate substantially from all the theoretical trends. How do we rationalize this discrepancy? There seem to be four possibilities. First, perhaps twinning in HEAs is completely different than in elemental alloys; this is rejected due to lack of evidence at the current time. Second, much like full dislocations moving through the solute field of the alloy are significantly strengthened, the twinning dislocations should experience similar solute strengthening. This is entirely feasible but has yet to be studied theoretically (but see Ghazisaeidi et al. for solute strengthening of twinning in Mg alloys [346]). Third, the assumption  $\gamma_{\text{stf}} \sim \gamma_{\text{ssf}}/2$  may not hold in alloys, with some evidence coming from DFT computations by Kibey et al [345]. However, huge deviations would

be needed and this is not expected. Fourth, the experimentally-deduced value for  $\gamma_{\text{ssf}}$  may be incorrect. Considering this last possibility, DFT computations indicate that CoCrFeMnNi is fairly anisotropic, with one DFT computation yielding  $C_{11} = 200 \text{ GPa}$ ,  $C_{12} = 95 \text{ GPa}$ ,  $C_{44} = 142 \text{ GPa}$ , with Zener anisotropy ratio  $A = 2.4$ . The Voigt, Reuss, and Bacon-Scattergood ( $\mu = \frac{C_{44}}{\sqrt{A}}$ ) estimates of the isotropic shear modulus are  $\mu = 106 \text{ GPa}$ ,  $84 \text{ GPa}$ ,  $86 \text{ GPa}$ , respectively, and the latter two are in good agreement with the measured low temperature polycrystalline value of  $85 \text{ GPa}$ . Using the measured stacking fault separation reported in [154] and full anisotropic elasticity theory then yields  $\gamma_{\text{ssf}} = 32 - 38 \frac{\text{mJ}}{\text{m}^2}$  for CoCrFeMnNi, only marginally larger than the value for isotropic elasticity. Thus, anisotropy does not resolve the issue. The origin of the anomalously high twinning stress thus remains unresolved.

One value of the SFE computed for CoCrFeNiMn by DFT including magnetism [136] indicated  $\gamma_{\text{ssf}} = 20 - 27 \frac{\text{mJ}}{\text{m}^2}$ , roughly consistent with experiments. At the same time, a DFT CPA-KKR study [247] predicts that  $\gamma_{\text{ssf}} < 0$  in CoCrFeNiMn at  $T=0 \text{ K}$  and that  $\gamma_{\text{ssf}}$  is just barely positive ( $< 10 \frac{\text{mJ}}{\text{m}^2}$ ) due to entropic effects at  $T=300 \text{ K}$ . New first-principles results on NiCoCr, also predicted to have negative SFE at  $T=0 \text{ K}$ , were recently presented by Ding et al. [342]. Ding et al. further speculated that SRO in NiCoCr might create a positive SFE. They performed Monte Carlo studies to induce SRO in NiCoCr based on the first-principles DFT energetics and found that the SFE increases, and furthermore becomes positive and comparable to experiments with fairly extensive SRO (obtained by Monte Carlo executed at relatively low temperatures). SRO would be expected to contribute to strengthening, and in particular create an athermal contribution to the strength, and so this finding is important to validate.

Stacking fault energies are relevant not only for twinning but also for transformation from FCC to HCP, which can provide both strengthening and toughening. Niu et al. examined the origins of the formation of HCP regions in FCC observed to occur within



**Fig. 35.** HAADF-STEM (a), Center-of-Symmetry map (b) and atomistic simulation (c) of a lattice partial dislocation interacting with a preexisting twin/hcp domain in NiCoCr to grow the HCP domain (reproduced from [347]).

the NiCoCr alloy [347]. They attributed the ability of NiCoCr to transform to the more-negative value of stacking fault energy for the three-layer nascent HCP structure relative to the nascent twin structure, which was then related to the magnetic states of Ni, Co, and Cr in this alloy relative to other related alloys. To examine the HCP growth process, they then used atomistic models of Co, where HCP is favorable to FCC. They showed that FCC lattice dislocations impinging on a pre-existing twin or HCP structure would dissociate to form the HCP structure rather than the twin structure (Fig. 35). In FCC-stable materials, the lattice dislocation impinging on a twin interface will dissociate to grow the twin, without any HCP phase formation.

The observations of HCP phases in NiCoCr due to a possible negative SFE in NiCoCr and the demonstration that a positive SFE might be a consequence of SRO in this alloy may both be correct and related. The SRO may stabilize the FCC phase initially, but the destruction of SRO during deformation (slip) might then create local regions that are unstable and susceptible to HCP transformation. The overall problem remains unsolved, but this recent progress suggests considerable nuances that make it fascinating and should drive further studies.

#### 3.4.3. Work hardening

Work hardening involves the evolution of the dislocation network in a metal. The underlying physical phenomena are dislocation junction formation, creation of new active dislocation sources through appropriate junction formation, multiplication by cross-slip and double-cross-slip, jog formation and debris creation by cross-slip, dislocation junction annihilation, and dislocation annihilation via cross-slip. Unfortunately, the modeling of the collective dislocation evolution is challenging. The current main computational approach is discrete dislocation dynamics (DDD) modeling, where the evolution of dislocation line defects in an elastic medium is followed [348]. A set of rules for mobility and Peierls stress determine the underlying motion of individual segments, and other rules are introduced for junction formation/annihilation and cross-slip. Existing DDD methods do not take into account

specific alloying directly but rather only through the rules, which are essentially based on homogenized properties.

DDD has been used to study the motion of individual dislocations moving past precipitates (see, for instance, [349]). This is a strengthening phenomenon, not a hardening phenomenon (although if Orowan loops are formed, there is hardening), and is not operative in single-phase HEAs. DDD has just recently been used to examine motion of a dislocation through a solute field [350], but the study is on a dilute binary alloy. The complexity of a full random alloy, including interactions between solutes and the dislocation core, is generally beyond the scope of DDD at the present time.

Atomistic simulations have also been used to study various underlying phenomenon (e.g., dislocation mobility versus temperature and character, junction formation/annihilation; cross-slip; dislocation/precipitate interactions; etc.) but rarely in alloys, and not yet in complex alloys such as HEAs. These phenomena are not accessible by first-principles methods.

One exception is recent atomistic work on cross-slip in various binary FCC alloys, not limited to dilute solutions [351,335]. This study demonstrates that solute fluctuations can significantly reduce the cross-slip barrier, as compared to the values in the average alloy. Therefore, cross-slip is predicted to be greatly accelerated in alloys relative to pure elements. Cross-slip in HEAs can thus be expected to be facilitated as well. One computational study has taken the first step in this direction by computing the cross-slip barriers in the model FCC Ni<sub>36</sub>Co<sub>30</sub>Fe<sub>16.67</sub>Ti<sub>16.67</sub> alloy studied previously by Rao et al. [291]. While the average cross-slip barrier in this low-stacking-fault alloy ( $\gamma_{ssf} = 16 \text{ mJ/m}^2$ ) is very high (3.76 eV), some random arrangements of solutes within the ~40b length of the Friedel-Escaig cross-slip process are found to have barriers between 0.0 and 0.5 eV! Rao et al. reported the observation of cross-slip in direct MD simulations of the screw dislocation in this alloy over nanosecond times scales, implying a very low barrier for cross-slip under zero driving force for cross-slip. Therefore, local fluctuations in solute distributions in the random HEA alloys may facilitate cross-slip and thus strongly influence the

entire work-hardening evolution of the alloy. This remains to be studied in far more detail.

### 3.5. Open issues and summary

In this new domain of metallurgy, considerable theory and modeling progress has been made rather quickly in understanding some mechanical properties. While multifaceted and impressive, there certainly remain many open issues for theory and modeling. A number of them have been mentioned in the sections above. A remaining open issue for strength is the origin of the high Hall-Petch grain size strengthening in the FCC HEAs, which can significantly exceed that of, for instance, pure Ni. Different alloys have different Hall-Petch coefficients, and since this strengthening can be an important contribution to the total alloy strength, it is important to understand this effect better. Unfortunately, the H-P effect is not fully understood in the elemental metals (see [309] for a recent review) and the additional effects of high alloying pose an even greater challenge.

Fortunately, HEA deformation appears to be controlled by normal dislocation-mediated phenomena so that an underlying existing framework for metal plasticity is broadly applicable. The complications in HEAs thus arise in understanding how dislocations move through the highly compositionally-disordered lattice. The successes to date in the understanding of flow stress point toward a more-general theoretical approach of examining/predicting how spatial fluctuations of solute distributions over different scales couple to the behavior of crystalline defects, primarily dislocations, vacancies, grain boundaries, and cracks. The behaviors of these defects determine diffusional transport, grain-size strengthening, grain growth and coarsening, fracture, and other important phenomena. However, since quantitative theories for mechanical properties such as work hardening, ductility, twinning, fracture, and fatigue do not exist for traditional engineering alloys including dilute solid-solution alloys, the development of similar theories in the highly complex HEAs remains a major challenge. Experimental results showing high performance of HEAs for various properties provides a strong driving force to take on that challenge.

## 4. Conclusion and perspectives

Despite the large number of publications in the field of HEAs, there are relatively few systematic investigations of the mechanical properties of alloys with well-controlled and characterized microstructures. This is partly because the vast compositional space available provides researchers limitless room for exploration of new compositions (of which only a minuscule fraction has so far been investigated) with the hope of finding even better properties. Unfortunately, this has often led to preliminary hardness or compression tests that show promising results but that are not followed up with more-detailed fabrication, microstructure optimization, or measurement of crucial properties such as tensile, fracture, and fatigue that are most relevant for structural applications. Thus, large gaps remain in the determination of ‘relevant’ mechanical properties of most HEAs. Here, we thus focused on a few properties that have been frequently reported: the ultimate tensile/compressive strength and total elongation/compressive strain at both room temperature and elevated temperatures. These data for HEAs fall within the broad ranges reported for various conventional engineering alloys, although there are challenges in making such comparisons that should be taken into account. More importantly, the fundamental deformation mechanisms governing the flow and fracture of HEAs are essentially similar to those of conventional alloys. Therefore, the community can build on existing metallurgical knowledge to develop new HEAs with improved properties that rely on multiple mechanisms acting synergistically

to simultaneously enhance desirable mechanical properties such as strength and ductility (or toughness) that are often in conflict.

Complications arise from the concentrated, multicomponent nature of HEAs. In particular, whether the different atomic species are distributed randomly or show short-range ordering/clustering remains important yet largely unknown. The measurement of short-range order remains an experimental challenge that must be overcome. Computational results show that short-range order could emerge but connecting such studies to real time scales and materials processing remains to be done. The connection between short-range order and mechanical properties thus remains largely open, except for the basic understanding from traditional alloys that ordering tends to give some athermal strengthening and more planar slip. The assumption of a random alloy has enabled qualitative and quantitative progress in understanding properties. Correlations between average atomic displacements and yield strengths has proven useful for several equiatomic medium-entropy alloys (MEAs) and HEAs. A quantitative theory for yielding in random, concentrated solid solutions has been developed that can successfully predict experimentally measured yield strengths. Progress in adding non-random atomic distributions on top of the random alloy theory would appear to be an attractive avenue.

Theories of flow and fracture are inadequate even in simple metals and that is the case also in HEAs. However, mechanism-based explanations of strengthening seem to work reasonably well. These include Taylor hardening (from dislocation-dislocation interactions) and interface strengthening (from dislocation interactions with grain boundaries, twin boundaries and particle boundaries). Thus, strengthening of HEAs by refining the grain size and introducing precipitates work similarly as in conventional alloys. Introduction of new interfaces during straining (twin and phase boundaries) produces dynamic Hall-Petch strengthening as in TWIP/TRIP alloys.

In FCC HEAs, ductility is often limited by necking. Mechanisms such as TWIP or TRIP that can delay the onset of necking by providing constant (or even increasing) work hardening rates can contribute to both enhanced ductility and enhanced strength (by interface hardening). The details of how ductility is enhanced remain murky but, in the case of TWIP, it may be because twin boundaries both block dislocation motion and allow dislocations to glide along their interfaces thereby relieving stress concentrations. In the case of TRIP, phase transformations that can accommodate deformation with small misfits appear to be desirable for good ductility.

BCC HEAs, similar to simple BCC metals, differ significantly from FCC HEAs. The dominance of screw dislocations changes the fundamental strengthening, although there is the emerging possibility that edge dislocation may also play an important role in some BCC HEAs. The latter would be quite new, relative to existing alloys, but is not yet established. Oxygen and nitrogen interstitials give high additional strengthening, as in dilute and elemental BCC alloys, and usually embrittlement. However, local ordered oxygen complexes appear to avoid embrittlement in one refractory HEA by enhancing dislocation multiplication, and the generality of this promising mechanism requires more study. In some refractory HEAs, composition can be tuned to destabilize the HCP phase relative to BCC to introduce TRIP contributions, but so far there are no indications of TWIP effects in the refractory HEAs. The dominant issue in BCC HEAs is low ductility, and the reason(s) that a few refractory HEAs exhibit significant tensile ductility at room temperature must be understood. This might enable the design of new ductile refractory HEAs.

Going forward, it is unavoidable that HEAs will be screened initially using simple hardness and compression tests on small samples. However, once promising candidates are identified, it is important to scale up, control the microstructure, and perform more appropriate mechanical tests. At the same time, in contrast to this

top-down approach, a more bottom-up mechanistic approach is also warranted. For example, one could start with some of the better performing HEAs already identified in the literature and use various strengthening and toughening mechanisms to produce CCAs with properties that surpass those of existing alloys. The vast compositional space that remains to be explored allows multiple composition knobs to be turned simultaneously, which may make it possible to avoid conventional tradeoffs and obtain otherwise mutually exclusive properties.

### Declaration of Competing Interest

The authors declare that they have no known competing financial interests or personal relationships that could have appeared to influence the work reported in this paper.

### Acknowledgments

EPG is supported by the U.S. Department of Energy, Office of Science, Basic Energy Sciences, Materials Sciences and Engineering Division. WAC acknowledges support for this work through the European Research Council Advanced Grant "Predictive Computational Metallurgy", ERC Grant agreement No. 339081 – Pre-CoMet and from the Swiss National Science Foundation through the grant 200021\_181987 "Harnessing atomic-scale randomness: design and optimization of mechanical performance in High Entropy Alloys". CCT would like to acknowledge contributions of Shaolou Wei, Hyunseok Oh and Onur Guvenc in the preparation of the manuscript.

### Supplementary materials

Supplementary material associated with this article can be found, in the online version, at doi:[10.1016/j.actamat.2019.12.015](https://doi.org/10.1016/j.actamat.2019.12.015).

### References

- [1] D.B. Miracle, O.N. Senkov, A critical review of high entropy alloys and related concepts, *Acta Mater.* 122 (2017) 448–511, doi:[10.1016/j.actamat.2016.08.081](https://doi.org/10.1016/j.actamat.2016.08.081).
- [2] B. Gludovatz, A. Hohenwarter, D. Catooor, E.H. Chang, E.P. George, R.O. Ritchie, A fracture-resistant high-entropy alloy for cryogenic applications, *Science* 345 (2014) 1153–1158 (80–), doi:[10.1126/science.1254581](https://doi.org/10.1126/science.1254581).
- [3] Y. Zou, P. Okle, H. Yu, T. Sumigawa, T. Kitamura, S. Maiti, W. Steurer, R. Spolenak, Fracture properties of a refractory high-entropy alloy: in situ microcantilever and atom probe tomography studies, *Scr. Mater.* 128 (2017) 95–99, doi:[10.1016/j.scriptamat.2016.09.036](https://doi.org/10.1016/j.scriptamat.2016.09.036).
- [4] U. Roy, H. Roy, H. Daoud, U. Glatzel, K.K. Ray, Fracture toughness and fracture micromechanism in a cast AlCoCrCuFeNi high entropy alloy system, *Mater. Lett.* 132 (2014) 186–189, doi:[10.1016/j.matlet.2014.06.067](https://doi.org/10.1016/j.matlet.2014.06.067).
- [5] C. Chen, S. Pang, Y. Cheng, T. Zhang, Microstructure and mechanical properties of Al20-xCr20+0.5xFe20Co20Ni20+0.5x high entropy alloys, *J. Alloys Compd.* 659 (2016) 279–287, doi:[10.1016/j.jallcom.2015.10.258](https://doi.org/10.1016/j.jallcom.2015.10.258).
- [6] Z. Tang, T. Yuan, C.W. Tsai, J.W. Yeh, C.D. Lundin, P.K. Liaw, Fatigue behavior of a wrought Al-<inf>0.5</inf>CrCuFeNi two-phase high-entropy alloy, *Acta Mater.* 99 (2015) 247–258, doi:[10.1016/j.actamat.2015.07.004](https://doi.org/10.1016/j.actamat.2015.07.004).
- [7] M.A. Hemphill, T. Yuan, G.Y. Wang, J.W. Yeh, C.W. Tsai, A. Chuang, P.K. Liaw, Fatigue behavior of Al0.5CoCrCuFeNi high entropy alloys, *Acta Mater.* 60 (2012) 5723–5734, doi:[10.1016/j.actamat.2012.06.046](https://doi.org/10.1016/j.actamat.2012.06.046).
- [8] K.V.S. Thurston, B. Gludovatz, A. Hohenwarter, G. Laplanche, E.P. George, R.O. Ritchie, Effect of temperature on the fatigue-crack growth behavior of the high-entropy alloy CrMnFeCoNi, *Intermetallics* (2017), doi:[10.1016/j.intermet.2017.05.009](https://doi.org/10.1016/j.intermet.2017.05.009).
- [9] M. Seifi, D. Li, Z. Yong, P.K. Liaw, J.J. Lewandowski, Fracture toughness and fatigue crack growth behavior of as-cast high-entropy alloys, *JOM* (2015), doi:[10.1007/s11837-015-1563-9](https://doi.org/10.1007/s11837-015-1563-9).
- [10] J.Y. He, W.H. Liu, H. Wang, Y. Wu, X.J. Liu, T.G. Nieh, Z.P. Lu, Effects of Al addition on structural evolution and tensile properties of the FeCoNiCrMn high-entropy alloy system, *Acta Mater.* 62 (2014) 105–113, doi:[10.1016/j.actamat.2013.09.037](https://doi.org/10.1016/j.actamat.2013.09.037).
- [11] S.I. Hong, J. Moon, S.K. Hong, H.S. Kim, Thermally activated deformation and the rate controlling mechanism in CoCrFeMnNi high entropy alloy, *Mater. Sci. Eng. A* 682 (2017) 569–576, doi:[10.1016/j.msea.2016.11.078](https://doi.org/10.1016/j.msea.2016.11.078).
- [12] Q.F. He, J.F. Zeng, S. Wang, Y.F. Ye, C. Zhu, T.G. Nieh, Z.P. Lu, Y. Yang, Delayed plasticity during nanoindentation of single-phase CoCrFeMnNi high-entropy alloy, *Mater. Res. Lett.* 5 (2017) 300–305, doi:[10.1080/21663831.2016.1269026](https://doi.org/10.1080/21663831.2016.1269026).
- [13] M. Kawasaki, B. Ahn, P. Kumar, J. Il Jang, T.G. Langdon, Nano- and micro-mechanical properties of ultrafine-grained materials processed by severe plastic deformation techniques, *Adv. Eng. Mater.* 19 (2017) 1–17, doi:[10.1002/adem.201600578](https://doi.org/10.1002/adem.201600578).
- [14] Z. Li, C.C. Tasan, H. Springer, B. Gault, D. Raabe, Interstitial atoms enable joint twinning and transformation induced plasticity in strong and ductile high-entropy alloys, *Sci. Rep.* 7 (2017) 40704, doi:[10.1038/srep40704](https://doi.org/10.1038/srep40704).
- [15] Y. Zhang, S. Wang, S. Jiang, X. Zhu, D. Sun, Microstructures and mechanical properties of NiTiFeAlCu high-entropy alloys with exceptional nano-precipitates, *J. Mater. Eng. Perform.* 26 (2017) 41–50, doi:[10.1007/s11665-016-2407-7](https://doi.org/10.1007/s11665-016-2407-7).
- [16] Z.G. Zhu, K.H. Ma, X. Yang, C.H. Shek, Annealing effect on the phase stability and mechanical properties of (FeNiCrMn) (100-x) Co x high entropy alloys, *J. Alloys Compd.* 695 (2017) 2945–2950, doi:[10.1016/j.jallcom.2016.11.376](https://doi.org/10.1016/j.jallcom.2016.11.376).
- [17] S. Jiang, D. sun, Y. Zhang, S. Wang, C. Zhao, Plastic deformation mechanisms of equiatomic Ni20Ti20Fe20Al20Cu20 high-entropy alloy at high temperatures, *J. Mater. Sci.* 52 (2017) 3199–3207, doi:[10.1007/s10853-016-0609-x](https://doi.org/10.1007/s10853-016-0609-x).
- [18] J.Y. He, H. Wang, Y. Wu, X.J. Liu, T.G. Nieh, Z.P. Lu, High-temperature plastic flow of a precipitation-hardened FeCoNiCr high entropy alloy, *Mater. Sci. Eng. A* 686 (2017) 34–40, doi:[10.1016/j.msea.2017.01.027](https://doi.org/10.1016/j.msea.2017.01.027).
- [19] R. Wang, K. Zhang, C. Davies, X. Wu, Evolution of microstructure, mechanical and corrosion properties of AlCoCrFeNi high-entropy alloy prepared by direct laser fabrication, *J. Alloys Compd.* 694 (2017) 971–981, doi:[10.1016/j.jallcom.2016.10.138](https://doi.org/10.1016/j.jallcom.2016.10.138).
- [20] P. Li, A. Wang, C.T. Liu, A ductile high entropy alloy with attractive magnetic properties, *J. Alloys Compd.* 694 (2017) 55–60, doi:[10.1016/j.jallcom.2016.09.186](https://doi.org/10.1016/j.jallcom.2016.09.186).
- [21] M. Komarasamy, N. Kumar, Z. Tang, R.S. Mishra, P.K. Liaw, Effect of microstructure on the deformation mechanism of friction stir-processed Al0.1CoCrFeNi high entropy alloy, *Mater. Res. Lett.* 3 (2014) 30–34, doi:[10.1080/21663831.2014.958586](https://doi.org/10.1080/21663831.2014.958586).
- [22] D.H. Xiao, P.F. Zhou, W.Q. Wu, H.Y. Diao, M.C. Gao, M. Song, P.K. Liaw, Microstructure, mechanical and corrosion behaviors of AlCoCuFeNi-(Cr,Ti) high entropy alloys, *Mater. Des.* 116 (2017) 438–447, doi:[10.1016/j.matdes.2016.12.036](https://doi.org/10.1016/j.matdes.2016.12.036).
- [23] L. Ma, C. Li, Y. Jiang, J. Zhou, L. Wang, F. Wang, T. Cao, Y. Xue, Cooling rate-dependent microstructure and mechanical properties of AlxSi0.2CrFeCoNiCu1-x high entropy alloys, *J. Alloys Compd.* 694 (2017) 61–67, doi:[10.1016/j.jallcom.2016.09.213](https://doi.org/10.1016/j.jallcom.2016.09.213).
- [24] H. Shahmir, J. He, Z. Lu, M. Kawasaki, T.G. Langdon, Evidence for superplasticity in a CoCrFeNiMn high-entropy alloy processed by high-pressure torsion, *Mater. Sci. Eng. A* 685 (2017) 342–348, doi:[10.1016/j.msea.2017.01.016](https://doi.org/10.1016/j.msea.2017.01.016).
- [25] V. Maier-Kiener, B. Schuh, E.P. George, H. Clemens, A. Hohenwarter, Nanoindentation testing as a powerful screening tool for assessing phase stability of nanocrystalline high-entropy alloys, *Mater. Des.* 115 (2017) 479–485, doi:[10.1016/j.matdes.2016.11.055](https://doi.org/10.1016/j.matdes.2016.11.055).
- [26] R. Li, M. Wang, T. Yuan, B. Song, Y. Shi, Microstructural modification of laser-deposited high-entropy CrFeCoNiMoWC alloy by friction stir processing: nanograin formation and deformation mechanism, *Metall. Mater. Trans. A Phys. Metall. Mater. Sci.* 48 (2017) 841–854, doi:[10.1007/s11661-016-3875-y](https://doi.org/10.1007/s11661-016-3875-y).
- [27] N.D. Stepanov, D.G. Shaysultanov, R.S. Chernichenko, N.Y. Yurchenko, S.V. Zherezbtsov, M.A. Tikhonovsky, G.A. Salishchev, Effect of thermomechanical processing on microstructure and mechanical properties of the carbon-containing CoCrFeNiMn high entropy alloy, *J. Alloys Compd.* 693 (2017) 394–405, doi:[10.1016/j.jallcom.2016.09.208](https://doi.org/10.1016/j.jallcom.2016.09.208).
- [28] T. Yang, Z. Tang, X. Xie, R. Carroll, G. Wang, Y. Wang, K.A. Dahmen, P.K. Liaw, Y. Zhang, Deformation mechanisms of Al0.1CoCrFeNi at elevated temperatures, *Mater. Sci. Eng. A* 684 (2017) 552–558, doi:[10.1016/j.msea.2016.12.110](https://doi.org/10.1016/j.msea.2016.12.110).
- [29] L.Y. Tian, G. Wang, J.S. Harris, D.L. Irving, J. Zhao, L. Vitos, Alloying effect on the elastic properties of refractory high-entropy alloys, *Mater. Des.* 114 (2017) 243–252, doi:[10.1016/j.matdes.2016.11.079](https://doi.org/10.1016/j.matdes.2016.11.079).
- [30] H. Prasad, S. Singh, B.B. Panigrahi, Mechanical activated synthesis of alumina dispersed FeNiCrAlMn high entropy alloy, *J. Alloys Compd.* 692 (2017) 720–726, doi:[10.1016/j.jallcom.2016.09.080](https://doi.org/10.1016/j.jallcom.2016.09.080).
- [31] B. Gwalani, V. Soni, M. Lee, S.A. Mantri, Y. Ren, R. Banerjee, Optimizing the coupled effects of Hall-Petch and precipitation strengthening in a Al0.3CoCrFeNi high entropy alloy, *Mater. Des.* 121 (2017) 254–260, doi:[10.1016/j.matdes.2017.02.072](https://doi.org/10.1016/j.matdes.2017.02.072).
- [32] Z. Fu, W. Chen, Z. Chen, H. Wen, E.J. Lavernia, Influence of Ti addition and sintering method on microstructure and mechanical behavior of a medium-entropy Al0.6CoNiFe alloy, *Mater. Sci. Eng. A* 619 (2014) 137–145, doi:[10.1016/j.msea.2014.09.077](https://doi.org/10.1016/j.msea.2014.09.077).
- [33] X. Xian, Z. Zhong, B. Zhang, K. Song, C. Chen, S. Wang, J. Cheng, Y. Wu, A high-entropy V35Ti35Fe15Cr10Zr5 alloy with excellent high-temperature strength, *Mater. Des.* 121 (2017) 229–236, doi:[10.1016/j.matdes.2017.02.029](https://doi.org/10.1016/j.matdes.2017.02.029).
- [34] Z.Y. Liang, J.T.M. De Hosson, M.X. Huang, Size effect on deformation twinning in face-centred cubic single crystals: experiments and modelling, *Acta Mater.* 129 (2017) 1–10, doi:[10.1016/j.actamat.2017.02.063](https://doi.org/10.1016/j.actamat.2017.02.063).
- [35] Z. Rao, X. Wang, Q. Wang, T. Liu, X. Chen, L. Wang, X. Hui, Microstructure, mechanical properties, and oxidation behavior of Al<sub>x</sub>Cr<sub>0.4</sub>CuFe<sub>0.4</sub>MnNi high entropy alloys, *Adv. Eng. Mater.* 19 (2017) 1600726, doi:[10.1002/adem.201600726](https://doi.org/10.1002/adem.201600726).
- [36] T.K. Tsao, A.C. Yeh, H. Murakami, The microstructure stability of precipitation strengthened medium to high entropy superalloys, *Metall. Mater. Trans. A Phys. Metall. Mater. Sci.* 48 (2017) 2435–2442, doi:[10.1007/s11661-017-4037-6](https://doi.org/10.1007/s11661-017-4037-6).

- [37] J.X. Fu, C.M. Cao, W. Tong, Y.X. Hao, L.M. Peng, The tensile properties and serrated flow behavior of a thermomechanically treated CoCrFeNiMn high-entropy alloy, Mater. Sci. Eng. A 690 (2017) 418–426, doi:10.1016/j.msea.2017.03.031.
- [38] S.P. Wang, J. Xu, TiZrNbTaMo high-entropy alloy designed for orthopedic implants: As-cast microstructure and mechanical properties, Mater. Sci. Eng. C 73 (2017) 80–89, doi:10.1016/j.msec.2016.12.057.
- [39] I. Moravcik, J. Cizek, J. Zapletal, Z. Kovacova, J. Vesely, P. Minarik, M. Kitzmantel, R. Neubauer, I. Dlouhy, Microstructure and mechanical properties of Ni<sub>1.5</sub>Co<sub>1.5</sub>Cr<sub>1.5</sub>Ti<sub>0.5</sub> high entropy alloy fabricated by mechanical alloying and spark plasma sintering, Mater. Des. 119 (2017) 141–150, doi:10.1016/j.matdes.2017.01.036.
- [40] S.H. Joo, H. Kato, M.J. Jang, J. Moon, C.W. Tsai, J.W. Yeh, H.S. Kim, Tensile deformation behavior and deformation twinning of an equimolar CoCrFeMnNi high-entropy alloy, Mater. Sci. Eng. A 689 (2017) 122–133, doi:10.1016/j.msea.2017.02.043.
- [41] D. Tabachnikova, V. Podolskiy, M.O. Laktionova, N.A. Bereznina, M.A. Tikhonovsky, A.S. Tortika, Mechanical properties of the CoCrFeNiMnVx high entropy alloys in temperature range 4.2–300K, J. Alloys Compd. 698 (2017) 501–509, doi:10.1016/j.jallcom.2016.12.154.
- [42] P. Gong, J. Jin, L. Deng, S. Wang, G. Yu, K. Yao, X. Wang, Room temperature nanoindentation creep behavior of TiZrHfBeCu(Ni) high entropy bulk metallic glasses, Mater. Sci. Eng. A 688 (2017) 174–179, doi:10.1016/j.msea.2017.01.094.
- [43] Z. Wu, H. Bei, G.M. Pharr, E.P. George, Temperature dependence of the mechanical properties of equiatomic solid solution alloys with face-centered cubic crystal structures, Acta Mater. 81 (2014) 428–441, doi:10.1016/j.actamat.2014.08.026.
- [44] J. Wang, Y. Liu, B. Liu, Y. Wang, Y. Cao, T. Li, R. Zhou, Flow behavior and microstructures of powder metallurgical CrFeCoNiMo0.2 high entropy alloy during high temperature deformation, Mater. Sci. Eng. A 689 (2017) 233–242, doi:10.1016/j.msea.2017.02.064.
- [45] K. Jin, S. Mu, K. An, W.D. Porter, G.D. Samolyuk, G.M. Stocks, H. Bei, Thermo-physical properties of Ni-containing single-phase concentrated solid solution alloys, Mater. Des. 117 (2017) 185–192, doi:10.1016/j.matdes.2016.12.079.
- [46] H.W. Yao, J.W. Qiao, J.A. Hawk, H.F. Zhou, M.W. Chen, M.C. Gao, Mechanical properties of refractory high-entropy alloys: experiments and modeling, J. Alloys Compd. 696 (2017) 1139–1150, doi:10.1016/j.jallcom.2016.11.188.
- [47] B.R. Braeckman, F. Misják, G. Radnócz, M. Caplovicová, P. Djemja, F. Té-tard, L. Belliard, D. Depla, The nanostructure and mechanical properties of nanocomposite Nb x -CoCrCuFeNi thin films, Scr. Mater. 139 (2017) 155–158, doi:10.1016/j.scriptamat.2017.06.046.
- [48] R. Raghavan, C. Kirchlechner, B.N. Jaya, M. Feuerbacher, G. Dehm, Mechanical size effects in a single crystalline equiatomic FeCrCoMnNi high entropy alloy, Scr. Mater. 129 (2017) 52–55, doi:10.1016/j.scriptamat.2016.10.026.
- [49] J. Joseph, N. Stanford, P. Hodgson, D.M. Fabijanic, Tension/compression asymmetry in additive manufactured face centered cubic high entropy alloy, Scr. Mater. 129 (2017) 30–34, doi:10.1016/j.scriptamat.2016.10.023.
- [50] N.Y. Yurchenko, N.D. Stepanov, S.V. Zherebtsov, M.A. Tikhonovsky, G.A. Salishchev, Structure and mechanical properties of B2 ordered refractory AlNbTiVx ( $x = 0–1.5$ ) high-entropy alloys, Mater. Sci. Eng. A 704 (2017) 82–90, doi:10.1016/j.msea.2017.08.019.
- [51] X. Liu, L. Zhang, Y. Xu, Microstructure and mechanical properties of graphene reinforced Fe50Mn30Co10Cr10 high-entropy alloy composites synthesized by MA and SPS, Appl. Phys. A Mater. Sci. Process. (2017) 123, doi:10.1007/s00339-017-1151-7.
- [52] C. Varvenne, W.A. Curtin, Strengthening of high entropy alloys by dilute solute additions: CoCrFeNiAlx and CoCrFeNiMnx alloys, Scr. Mater. 138 (2017) 92–95, doi:10.1016/j.scriptamat.2017.05.035.
- [53] M. Zhang, X. Zhou, J. Li, Microstructure and mechanical properties of a refractory CoCrMoNbTi high-entropy alloy, J. Mater. Eng. Perform. 26 (2017) 3657–3665, doi:10.1007/s11665-017-2799-z.
- [54] C.-W. Lin, M.-H. Tsai, C.-W. Tsai, J.-W. Yeh, S.-K. Chen, Microstructure and aging behaviour of Al<sub>5</sub>Cr<sub>32</sub>Fe<sub>35</sub>Ni<sub>22</sub>Ti<sub>2</sub> high entropy alloy, Mater. Sci. Technol. 31 (2015) 1165–1170, doi:10.1179/1743284715Y.0000000025.
- [55] H. Luo, Z. Li, D. Raabe, Hydrogen enhances strength and ductility of an equiatomic high-entropy alloy, Sci. Rep. 7 (2017) 9892, doi:10.1038/s41598-017-10774-4.
- [56] J. Liu, C. Chen, Y. Xu, S. Wu, G. Wang, H. Wang, Y. Fang, L. Meng, Deformation twinning behaviors of the low stacking fault energy high-entropy alloy: an in-situ TEM study, Scr. Mater. 137 (2017) 9–12, doi:10.1016/j.scriptamat.2017.05.001.
- [57] M. Ogura, T. Fukushima, R. Zeller, P.H. Dederichs, Structure of the high-entropy alloy Al<sub>x</sub>Cr<sub>Fe</sub>CoNi: FCC versus BCC, J. Alloys Compd. 715 (2017) 454–459, doi:10.1016/j.jallcom.2017.04.318.
- [58] A.S. Ahmad, Y. Su, S.Y. Liu, K. Stähli, Y.D. Wu, X.D. Hui, U. Ruett, O. Gutowski, K. Glazyrin, H.P. Liermann, H. Franz, H. Wang, X.D. Wang, Q.P. Cao, D.X. Zhang, J.Z. Jiang, Structural stability of high entropy alloys under pressure and temperature, J. Appl. Phys. (2017) 121, doi:10.1063/1.4984796.
- [59] X.B. Feng, J.Y. Zhang, Y.Q. Wang, Z.Q. Hou, K. Wu, G. Liu, J. Sun, Size effects on the mechanical properties of nanocrystalline NbMoTaW refractory high entropy alloy thin films, Int. J. Plast. 95 (2017) 264–277, doi:10.1016/j.ijplas.2017.04.013.
- [60] D.G. Shaysultanov, N.D. Stepanov, G.A. Salishchev, M.A. Tikhonovsky, Effect of heat treatment on the structure and hardness of high-entropy alloys CoCrFeNiMnV x ( $x = 0.25, 0.5, 0.75, 1$ ), Phys. Met. Metallogr. 118 (2017) 579–590, doi:10.1134/S0031918X17060084.
- [61] J. Guo, X. Huang, W. Huang, Microstructure and Room-temperature mechanical properties of FeCrMoV<sub>1-x</sub>Cr<sub>x</sub>-high-entropy alloys, J. Mater. Eng. Perform. 26 (2017) 3071–3078, doi:10.1007/s11665-017-2742-3.
- [62] K. Ming, X. Bi, J. Wang, Precipitation strengthening of ductile Cr15Fe20Co35Ni20Mo10 alloys, Scr. Mater. 137 (2017) 88–93, doi:10.1016/j.scriptamat.2017.05.019.
- [63] Z. Li, C.C. Tasan, K.G. Pradeep, D. Raabe, A TRIP-assisted dual-phase high-entropy alloy: Grain size and phase fraction effects on deformation behavior, Acta Mater. 131 (2017) 323–335, doi:10.1016/j.actamat.2017.03.069.
- [64] Á. Vida, N.Q. Chinh, J. Lendvai, A. Heczel, L.K. Varga, Microstructures and transition from brittle to ductile behavior of NiFeCrMoW High Entropy Alloys, Mater. Lett. 195 (2017) 14–17, doi:10.1016/j.matlet.2017.02.063.
- [65] D. Liu, J.B. Cheng, H. Ling, Electrochemical behaviours of (NiCoFeCrCu)<sub>95</sub>B<sub>5</sub> high entropy alloy coatings, Mater. Sci. Technol. 31 (2015) 1159–1164, doi:10.1179/1743284714Y.0000000739.
- [66] J. Joseph, N. Stanford, P. Hodgson, D.M. Fabijanic, Understanding the mechanical behaviour and the large strength/ductility differences between FCC and BCC Al x CoCrFeNi high entropy alloys, J. Alloys Compd. 726 (2017) 885–895, doi:10.1016/j.jallcom.2017.08.067.
- [67] D.G. Shaysultanov, G.A. Salishchev, Y.V. Ivanisenko, S.V. Zherebtsov, M.A. Tikhonovsky, N.D. Stepanov, Novel Fe36Mn21Cr18Ni15Al10 high entropy alloy with bcc/B2 dual-phase structure, J. Alloys Compd. 705 (2017) 756–763, doi:10.1016/j.jallcom.2017.02.211.
- [68] W. Huo, H. Zhou, F. Fang, Z. Xie, J. Jiang, Microstructure and mechanical properties of CoCrFeNiZr x eutectic high-entropy alloys, Mater. Des. 134 (2017) 226–233, doi:10.1016/j.matdes.2017.08.030.
- [69] K.R. Lim, K.S. Lee, J.S. Lee, J.Y. Kim, H.J. Chang, Y.S. Na, Dual-phase high-entropy alloys for high-temperature structural applications, J. Alloys Compd. 728 (2017) 1235–1238, doi:10.1016/j.jallcom.2017.09.089.
- [70] W. Huo, F. Fang, H. Zhou, Z. Xie, J. Shang, J. Jiang, Remarkable strength of CoCrFeNi high-entropy alloy wires at cryogenic and elevated temperatures, Scr. Mater. 141 (2017) 125–128, doi:10.1016/j.scriptamat.2017.08.006.
- [71] S.J. Sun, Y.Z. Tian, H.R. Lin, X.G. Dong, Y.H. Wang, Z.J. Zhang, Z.F. Zhang, Enhanced strength and ductility of bulk CoCrFeMnNi high entropy alloy having fully recrystallized ultrafine-grained structure, Mater. Des. 133 (2017) 122–127, doi:10.1016/j.matdes.2017.07.054.
- [72] P. Sathiyamoorthi, J. Basu, S. Kashyap, K.G. Pradeep, R.S. Kottada, Thermal stability and grain boundary strengthening in ultrafine-grained CoCrFeNi high entropy alloy composite, Mater. Des. 134 (2017) 426–433, doi:10.1016/j.matdes.2017.08.053.
- [73] H. Zhang, H. Tang, Y.Z. He, J.L. Zhang, W.H. Li, S. Guo, Effect of heat treatment on borides precipitation and mechanical properties of CoCrFe-NiAl1.8Cu0.7B0.3Si0.1 high-entropy alloy prepared by arc-melting and laser-cladding, JOM 69 (2017) 2078–2083, doi:10.1007/s11837-017-2381-z.
- [74] Z. Zhang, H. Zhang, Y. Tang, L. Zhu, Y. Ye, S. Li, S. Bai, Microstructure, mechanical properties and energetic characteristics of a novel high-entropy alloy HfZrTiTa0.53, Mater. Des. 133 (2017) 435–443, doi:10.1016/j.matdes.2017.08.022.
- [75] K.S. Lee, J.H. Kang, K.R. Lim, Y.S. Na, Influence of compressive strain on the microstructural evolution of an AlCrCrFeNi high entropy alloy, Mater. Charact. 132 (2017) 162–168, doi:10.1016/j.matchar.2017.08.010.
- [76] Z.M. Jiao, M.Y. Chu, H.J. Yang, Z.H. Wang, J.W. Qiao, Nanoindentation characterised plastic deformation of a Al<sub>0.5</sub>CoCrFeNi high entropy alloy, Mater. Sci. Technol. 31 (2015) 1244–1249, doi:10.1179/1743284715Y.0000000048.
- [77] Z. Cai, X. Cui, G. Jin, Z. Liu, N. Tan, Y. Li, M. Dong, D. Zhang, Effect of V content on microstructure and properties of laser-solidified Fe<sub>60</sub>(NiCrCoTi)V<sub>40</sub> ( $x = 0, 0.5, 1$ ) multicomponent alloy coatings on AISI 1045 steel, Mater. Charact. 132 (2017) 373–380, doi:10.1016/j.matchar.2017.09.007.
- [78] T.-K. Tsao, A.-C. Yeh, C.-M. Kuo, K. Kakehi, H. Murakami, J.-W. Yeh, S.-R. Jian, The high temperature tensile and creep behaviors of high entropy superalloy, Sci. Rep. 7 (2017) 12658, doi:10.1038/s41598-017-13026-7.
- [79] T.K. Liu, Z. Wu, A.D. Stoica, Q. Xie, W. Wu, Y.F. Gao, H. Bei, K. An, Twinning-mediated work hardening and texture evolution in CrCoFeMnNi high entropy alloys at cryogenic temperature, Mater. Des. 131 (2017) 419–427, doi:10.1016/j.matdes.2017.06.039.
- [80] Z. Wu, M.C. Troparevsky, Y.F. Gao, J.R. Morris, G.M. Stocks, H. Bei, Phase stability, physical properties and strengthening mechanisms of concentrated solid solution alloys, Curr. Opin. Solid State Mater. Sci. 21 (2017) 267–284, doi:10.1016/j.cosss.2017.07.001.
- [81] X.B. Feng, W. Fu, J.Y. Zhang, J.T. Zhao, J. Li, K. Wu, G. Liu, J. Sun, Effects of nanotwins on the mechanical properties of Al<sub>x</sub>CoCrFeNi high entropy alloy thin films, Scr. Mater. 139 (2017) 71–76, doi:10.1016/j.scriptamat.2017.06.009.
- [82] Z. Fu, B.E. MacDonald, D. Zhang, B. Wu, W. Chen, J. Ivanisenko, H. Hahn, E.J. Lavernia, Fcc nanostructured TiFeCoNi alloy with multi-scale grains and enhanced plasticity, Scr. Mater. 143 (2018) 108–112, doi:10.1016/j.scriptamat.2017.09.023.
- [83] T. Niendorf, T. Wegener, Z. Li, D. Raabe, Unexpected cyclic stress-strain response of dual-phase high-entropy alloys induced by partial reversibility of deformation, Scr. Mater. 143 (2018) 63–67, doi:10.1016/j.scriptamat.2017.09.013.
- [84] X. Feng, J. Zhang, Z. Xia, W. Fu, K. Wu, G. Liu, J. Sun, Stable nanocrystalline NbMoTaW high entropy alloy thin films with excellent mechanical and electrical properties, Mater. Lett. 210 (2018) 84–87, doi:10.1016/j.matlet.2017.08.129.

- [85] C. Varvenne, W.A. Curtin, Predicting yield strengths of noble metal high entropy alloys, *Scr. Mater.* 142 (2018) 92–95, doi:[10.1016/j.scriptamat.2017.08.030](https://doi.org/10.1016/j.scriptamat.2017.08.030).
- [86] S. Wei, F. He, C.C. Tasan, Metastability in high-entropy alloys: a review, *J. Mater. Res.* (2018) 1–14, doi:[10.1557/jmr.2018.306](https://doi.org/10.1557/jmr.2018.306).
- [87] G. Meng, T.M. Yue, X. Lin, H. Yang, H. Xie, X. Ding, Laser surface forming of AlCoCrCuFeNi particle reinforced AZ91D matrix composites, *Opt. Laser Technol.* 70 (2015) 119–127, doi:[10.1016/j.optlastec.2015.02.001](https://doi.org/10.1016/j.optlastec.2015.02.001).
- [88] Y. Ma, Q. Wang, B.B. Jiang, C.L. Li, J.M. Hao, X.N. Li, C. Dong, T.G. Nieh, Controlled formation of coherent cuboidal nanoprecipitates in body-centered cubic high-entropy alloys based on Al<sub>2</sub>(Ni,Co,Fe,Cr)<sub>14</sub> compositions, *Acta Mater.* (2018), doi:[10.1016/j.actamat.2018.01.050](https://doi.org/10.1016/j.actamat.2018.01.050).
- [89] X.D. Xu, P. Liu, Z. Tang, A. Hirata, S.X. Song, T.G. Nieh, P.K. Liaw, C.T. Liu, M.W. Chen, Transmission electron microscopy characterization of dislocation structure in a face-centered cubic high-entropy alloy Al0.1CoCrFeNi, *Acta Mater.* (2018), doi:[10.1016/j.actamat.2017.10.050](https://doi.org/10.1016/j.actamat.2017.10.050).
- [90] R. Chen, G. Qin, H. Zheng, L. Wang, Y. Su, Y.L. Chiu, H. Ding, J. Guo, H. Fu, Composition design of high entropy alloys using the valence electron concentration to balance strength and ductility, *Acta Mater.* (2018), doi:[10.1016/j.actamat.2017.10.058](https://doi.org/10.1016/j.actamat.2017.10.058).
- [91] Z. Li, S. Zhao, S.M. Alotaibi, Y. Liu, B. Wang, M.A. Meyers, Adiabatic shear localization in the CrMnFeCoNi high-entropy alloy, *Acta Mater.* (2018), doi:[10.1016/j.actamat.2018.03.040](https://doi.org/10.1016/j.actamat.2018.03.040).
- [92] J.B. Seol, J.W. Bae, Z. Li, J. Chan Han, J.G. Kim, D. Raabe, H.S. Kim, Boron doped ultrastrong and ductile high-entropy alloys, *Acta Mater.* (2018), doi:[10.1016/j.actamat.2018.04.004](https://doi.org/10.1016/j.actamat.2018.04.004).
- [93] M. Bönisch, Y. Wu, H. Sehitoglu, Hardening by slip-twin and twin-twin interactions in FeMnNiCoCr, *Acta Mater.* (2018), doi:[10.1016/j.actamat.2018.04.054](https://doi.org/10.1016/j.actamat.2018.04.054).
- [94] C. Lee, G. Song, M.C. Gao, R. Feng, P. Chen, J. Brecht, Y. Chen, K. An, W. Guo, J.D. Poplawsky, S. Li, A.T. Samaei, W. Chen, A. Hu, H. Choo, P.K. Liaw, Lattice distortion in a strong and ductile refractory high-entropy alloy, *Acta Mater.* (2018), doi:[10.1016/j.actamat.2018.08.053](https://doi.org/10.1016/j.actamat.2018.08.053).
- [95] B. Gwaltani, S. Gorsse, D. Choudhuri, M. Styles, Y. Zheng, R.S. Mishra, R. Banerjee, Modifying transformation pathways in high entropy alloys or complex concentrated alloys via thermo-mechanical processing, *Acta Mater.* (2018), doi:[10.1016/j.actamat.2018.05.009](https://doi.org/10.1016/j.actamat.2018.05.009).
- [96] Z. Lei, X. Liu, Y. Wu, H. Wang, S. Jiang, S. Wang, X. Hui, Y. Wu, B. Gault, P. Kontis, D. Raabe, L. Gu, Q. Zhang, H. Chen, H. Wang, J. Liu, K. An, Q. Zeng, T.G. Nieh, Z. Lu, Enhanced strength and ductility in a high-entropy alloy via ordered oxygen complexes, *Nature* (2018), doi:[10.1038/s41586-018-0685-y](https://doi.org/10.1038/s41586-018-0685-y).
- [97] C. Haase, L.A. Barrales-Mora, Influence of deformation and annealing twinning on the microstructure and texture evolution of face-centered cubic high-entropy alloys, *Acta Mater.* (2018), doi:[10.1016/j.actamat.2018.02.048](https://doi.org/10.1016/j.actamat.2018.02.048).
- [98] S. Guo, Phase selection rules for cast high entropy alloys: an overview, *Mater. Sci. Technol.* 31 (2015) 1223–1230, doi:[10.1179/1743284715Y.0000000018](https://doi.org/10.1179/1743284715Y.0000000018).
- [99] Y. Wang, B. Liu, K. Yan, M. Wang, S. Kabra, Y.L. Chiu, D. Dye, P.D. Lee, Y. Liu, B. Cai, Probing deformation mechanisms of a FeCoCrNi high-entropy alloy at 293 and 77 K using *in situ* neutron diffraction, *Acta Mater.* (2018), doi:[10.1016/j.actamat.2018.05.013](https://doi.org/10.1016/j.actamat.2018.05.013).
- [100] G. Laplanche, J. Bonneville, C. Varvenne, W.A. Curtin, E.P. George, Thermal activation parameters of plastic flow reveal deformation mechanisms in the CrMnFeCoNi high-entropy alloy, *Acta Mater.* (2018), doi:[10.1016/j.actamat.2017.10.014](https://doi.org/10.1016/j.actamat.2017.10.014).
- [101] B. Schuh, B. Völker, J. Todt, N. Schell, L. Perrière, J. Li, J.P. Couzinié, A. Hohenwarter, Thermodynamic instability of a nanocrystalline, single-phase TiZrNbHfTa alloy and its impact on the mechanical properties, *Acta Mater.* (2018), doi:[10.1016/j.actamat.2017.09.035](https://doi.org/10.1016/j.actamat.2017.09.035).
- [102] C.E. Slone, S. Chakraborty, J. Miao, E.P. George, M.J. Mills, S.R. Niezgoda, Influence of deformation induced nanoscale twinning and FCC-HCP transformation on hardening and texture development in medium-entropy CrCoNi alloy, *Acta Mater.* (2018), doi:[10.1016/j.actamat.2018.07.028](https://doi.org/10.1016/j.actamat.2018.07.028).
- [103] J.M. Sosa, J.K. Jensen, D.E. Huber, G.B. Viswanathan, M.A. Gibson, H.L. Fraser, Three-dimensional characterisation of the microstructure of an high entropy alloy using STEM/HAADF tomography, *Mater. Sci. Technol.* 31 (2015) 1250–1258, doi:[10.1179/1743284715Y.0000000049](https://doi.org/10.1179/1743284715Y.0000000049).
- [104] S. Liu, M.C. Gao, P.K. Liaw, Y. Zhang, Microstructures and mechanical properties of Al x CrFeNiTi 0.25 alloys, *J. Alloys Compd.* 619 (2015) 610–615, doi:[10.1016/j.jallcom.2014.09.073](https://doi.org/10.1016/j.jallcom.2014.09.073).
- [105] D. Choudhuri, T. Alam, T. Borkar, B. Gwaltani, A.S. Mantri, S.G. Srinivasan, M.A. Gibson, R. Banerjee, Formation of a Huesler-like L21 phase in a CoCr-CuFeNiAl high-entropy alloy, *Scr. Mater.* 100 (2015) 36–39, doi:[10.1016/j.scriptamat.2014.12.006](https://doi.org/10.1016/j.scriptamat.2014.12.006).
- [106] J. Joseph, T. Jarvis, X. Wu, N. Stanford, P. Hodgson, D.M. Fabijanic, Comparative study of the microstructures and mechanical properties of direct laser fabricated and arc-melted AlxCoCrFeNi high entropy alloys, *Mater. Sci. Eng. A* 633 (2015) 184–193, doi:[10.1016/j.msea.2015.02.072](https://doi.org/10.1016/j.msea.2015.02.072).
- [107] M. Feuerbacher, M. Heidelmann, C. Thomas, Plastic deformation properties of Zr-Nb-Ti-Ta-Hf high-entropy alloys, *Philos. Mag.* 95 (2015) 1221–1232, doi:[10.1080/14786435.2015.1028506](https://doi.org/10.1080/14786435.2015.1028506).
- [108] N.D. Stepanov, D.G. Shaysultanov, G.A. Salishchev, M.A. Tikhonovsky, Structure and mechanical properties of a light-weight AlNbTiV high entropy alloy, *Mater. Lett.* 142 (2015) 153–155, doi:[10.1016/j.matlet.2014.11.162](https://doi.org/10.1016/j.matlet.2014.11.162).
- [109] I.V. Karpets', O.M. Myslyuchenko, M.O. Krapivka, V.F. Gorban', O.S. Makarenko, V.A. Nazarenko, Influence of plastic deformation on the phase composition, texture, and mechanical properties of the CrMnFeCoNi2Cu high-entropy alloy, *J. Superhard Mater.* 37 (2015) 21–26, doi:[10.3103/s1063457615010049](https://doi.org/10.3103/s1063457615010049).
- [110] J.J. Licavoli, M.C. Gao, J.S. Sears, P.D. Jablonski, J.A. Hawk, Microstructure and mechanical behavior of high-entropy alloys, *J. Mater. Eng. Perform.* 24 (2015) 3685–3698, doi:[10.1007/s11665-015-1679-7](https://doi.org/10.1007/s11665-015-1679-7).
- [111] Z. Han, X. Liu, S. Zhao, Y. Shao, J. Li, K. Yao, Microstructure, phase stability and mechanical properties of Nb-Ni-Ti-Co-Zr and Nb-Ni-Ti-Co-Zr-Hf high entropy alloys, *Prog. Nat. Sci. Mater. Int.* 25 (2015) 365–369, doi:[10.1016/j.pnsc.2015.09.001](https://doi.org/10.1016/j.pnsc.2015.09.001).
- [112] J.P. Couzinié, L. Lilenstein, Y. Champion, G. Dirras, L. Perrière, I. Guillot, On the room temperature deformation mechanisms of a TiZrHfNbTa refractory high-entropy alloy, *Mater. Sci. Eng. A* 645 (2015) 255–263, doi:[10.1016/j.msea.2015.08.024](https://doi.org/10.1016/j.msea.2015.08.024).
- [113] G. Dirras, J. Gubicza, A. Heczel, L. Lilenstein, J.-P. Couzinié, L. Perrière, I. Guillot, A. Hocini, Microstructural investigation of plastically deformed Ti20Zr20HF20Nb20Ta20 high entropy alloy by X-ray diffraction and transmission electron microscopy, *Mater. Charact.* 108 (2015) 1–7, doi:[10.1016/j.matchar.2015.08.007](https://doi.org/10.1016/j.matchar.2015.08.007).
- [114] O.N. Senkov, G.B. Wilks, J.M. Scott, D.B. Miracle, Mechanical properties of Nb25Mo25Ta25W25 and V20Nb20Mo20Ta20W20 refractory high entropy alloys, *Intermetallics* 19 (2011) 698–706.
- [115] H.M. Daoud, A.M. Manzoni, N. Wanderka, U. Glatzel, High-temperature tensile strength of Al10Co25Cr8Fe15Ni36Ti6 compositionally complex alloy (high-entropy alloy), *JOM* 67 (2015) 2271–2277, doi:[10.1007/s11837-015-1484-7](https://doi.org/10.1007/s11837-015-1484-7).
- [116] B. Gludovatz, E.P. George, R.O. Ritchie, Processing, microstructure and mechanical properties of the CrMnFeCoNi high-entropy alloy, *JOM* 67 (2015) 2262–2270, doi:[10.1007/s11837-015-1589-z](https://doi.org/10.1007/s11837-015-1589-z).
- [117] D.-H. Lee, I.-C. Choi, M.-Y. Seok, J. He, Z. Lu, J.-Y. Suh, M. Kawasaki, T.G. Langdon, J. Jang, Nanomechanical behavior and structural stability of a nanocrystalline CoCrFeNiMn high-entropy alloy processed by high-pressure torsion, *J. Mater. Res.* 30 (2015) 2804–2815, doi:[10.1557/jmr.2015.239](https://doi.org/10.1557/jmr.2015.239).
- [118] S. Mridha, S. Das, S. Aouadi, S. Mukherjee, R.S. Mishra, Nanomechanical behavior of CoCrFeMnNi high-entropy alloy, *JOM* 67 (2015) 2296–2302, doi:[10.1007/s11837-015-1566-6](https://doi.org/10.1007/s11837-015-1566-6).
- [119] Z. Fu, W. Chen, H. Wen, S. Morgan, F. Chen, B. Zheng, Y. Zhou, L. Zhang, E.J. Lavernia, Microstructure and mechanical behavior of a novel Co20Ni20Fe20Al20Ti20 alloy fabricated by mechanical alloying and spark plasma sintering, *Mater. Sci. Eng. A* 644 (2015) 10–16, doi:[10.1016/j.msea.2015.07.052](https://doi.org/10.1016/j.msea.2015.07.052).
- [120] N. Park, X. Li, N. Tsuji, Microstructure and mechanical properties of Co21Cr22Cu22Fe21Ni14 processed by high pressure torsion and annealing, *JOM* 67 (2015) 2303–2309, doi:[10.1007/s11837-015-1586-2](https://doi.org/10.1007/s11837-015-1586-2).
- [121] B. Schuh, F. Mendez-Martin, B. Völker, E.P. George, H. Clemens, R. Pippan, A. Hohenwarter, Mechanical properties, microstructure and thermal stability of a nanocrystalline CoCrFeMnNi high-entropy alloy after severe plastic deformation, *Acta Mater.* 96 (2015) 258–268, doi:[10.1016/j.actamat.2015.06.025](https://doi.org/10.1016/j.actamat.2015.06.025).
- [122] N.N. Guo, L. Wang, L.S. Luo, X.Z. Li, Y.Q. Su, J.J. Guo, H.Z. Fu, Microstructure and mechanical properties of refractory MoNbHfZrTi high-entropy alloy, *Mater. Des.* 81 (2015) 87–94, doi:[10.1016/j.matdes.2015.05.019](https://doi.org/10.1016/j.matdes.2015.05.019).
- [123] Z.M. Jiao, S.G. Ma, G.Z. Yuan, Z.H. Wang, H.J. Yang, J.W. Qiao, Plastic deformation of Al0.3CoCrFeNi and AlCoCrFeNi high-entropy alloys under nanoindentation, *J. Mater. Eng. Perform.* 24 (2015) 3077–3083, doi:[10.1007/s11665-015-1576-0](https://doi.org/10.1007/s11665-015-1576-0).
- [124] N.I. Kourov, V.G. Pushin, A.V. Korolev, Y.V. Knyazev, M.V. Ivchenko, Y.M. Ustyugov, Peculiar features of physical properties of the rapid quenched AlCrFe-CoNiCu high-entropy alloy, *J. Alloys Compd.* 636 (2015) 304–309, doi:[10.1016/j.jallcom.2014.12.012](https://doi.org/10.1016/j.jallcom.2014.12.012).
- [125] H.M. Daoud, A. Manzoni, R. Völkli, N. Wanderka, U. Glatzel, Microstructure and tensile behavior of Al8Co17Cr 17Cu8Fe17Ni33 (at.%) high-entropy alloy, *JOM* 65 (2013) 1805–1814, doi:[10.1007/s11837-013-0756-3](https://doi.org/10.1007/s11837-013-0756-3).
- [126] X. Ji, Relative effect of electronegativity on formation of high entropy alloys, *Int. J. Cast Met. Res.* 28 (2015) 229–233, doi:[10.1179/1743133615Y.0000000004](https://doi.org/10.1179/1743133615Y.0000000004).
- [127] W.Q. Zhang, C.S. Lou, X.C. Wu, H.M. Fu, H.F. Zhang, Microstructures and mechanical property of [AlCoNiCrFe] alloy annealed in high magnetic field, *Mater. Sci. Technol.* (2015), doi:[10.1179/1743284714Y.000000069810.1179/1743284714Y.0000000698](https://doi.org/10.1179/1743284714Y.000000069810.1179/1743284714Y.0000000698).
- [128] S.G. Ma, J.W. Qiao, Z.H. Wang, H.J. Yang, Y. Zhang, Microstructural features and tensile behaviors of the Al0.5CrCuFeNi2 high-entropy alloys by cold rolling and subsequent annealing, *Mater. Des.* 88 (2015) 1057–1062, doi:[10.1016/j.matdes.2015.09.092](https://doi.org/10.1016/j.matdes.2015.09.092).
- [129] N. Kumar, Q. Ying, X. Nie, R.S. Mishra, Z. Tang, P.K. Liaw, R.E. Brennan, K.J. Doherty, K.C. Cho, High strain-rate compressive deformation behavior of the Al0.1CrFeCoNi high entropy alloy, *Mater. Des.* 86 (2015) 598–602, doi:[10.1016/j.matdes.2015.07.161](https://doi.org/10.1016/j.matdes.2015.07.161).
- [130] Y.-J. Chang, A.-C. Yeh, The evolution of microstructures and high temperature properties of AlxCo1.5CrFeNi1.5Tiy high entropy alloys, *J. Alloys Compd.* 653 (2015) 379–385, doi:[10.1016/j.jallcom.2015.09.042](https://doi.org/10.1016/j.jallcom.2015.09.042).
- [131] N.D. Stepanov, D.G. Shaysultanov, M.A. Tikhonovsky, G.A. Salishchev, Tensile properties of the Cr-Fe-Ni-Mn non-equiautomatic multicomponent alloys with different Cr contents, *Mater. Des.* 87 (2015) 60–65, doi:[10.1016/j.matdes.2015.08.007](https://doi.org/10.1016/j.matdes.2015.08.007).
- [132] N.D. Stepanov, N.Y. Yurchenko, D.V. Skibin, M.A. Tikhonovsky, G.A. Salishchev, Structure and mechanical properties of the AlCr<sub>x</sub>NbTiV (x = 0, 0.5, 1, 1.5) high entropy alloys, *J. Alloys Compd.* 652 (2015) 266–280, doi:[10.1016/j.jallcom.2015.08.224](https://doi.org/10.1016/j.jallcom.2015.08.224).
- [133] H. Jiang, L. Jiang, K. Han, Y. Lu, T. Wang, Z. Cao, T. Li, Effects of tungsten on microstructure and mechanical properties of CrFeNiV0.5Wx and Cr-

- FeNi2V0.5Wx high-entropy alloys, J. Mater. Eng. Perform. 24 (2015) 4594–4600, doi:10.1007/s11665-015-1767-8.
- [134] X.-R. Wang, P. He, T.-S. Lin, Z.-Q. Wang, Microstructure, thermodynamics and compressive properties of AlCrCuNi<sub>x</sub>Ti ( $x = 0, 1$ ) high entropy alloys, Mater. Sci. Technol. 31 (2015) 1842–1849, doi:10.1179/1743284715Y.0000000101.
- [135] Z. Chen, W. Chen, B. Wu, X. Cao, L. Liu, Z. Fu, Effects of Co and Ti on microstructure and mechanical behavior of Al0.75FeNiCrCo high entropy alloy prepared by mechanical alloying and spark plasma sintering, Mater. Sci. Eng. A. 648 (2015) 217–224, doi:10.1016/j.msea.2015.08.056.
- [136] A.J. Zaddach, C. Niu, C.C. Koch, D.L. Irving, Mechanical properties and stacking fault energies of NiFeCrCoMn high-entropy alloy, JOM 65 (2013) 1780–1789, doi:10.1007/s11837-013-0771-4.
- [137] L. Jiang, Z.Q. Cao, J.C. Jie, J.J. Zhang, Y.P. Lu, T.M. Wang, T.J. Li, Effect of Mo and Ni elements on microstructure evolution and mechanical properties of the CoFeNi<math>x</math>VMo<math>y</math>high entropy alloys, J. Alloys Compd. 649 (2015) 585–590, doi:10.1016/j.jallcom.2015.07.185.
- [138] O.N. Senkov, S.L. Semiatin, Microstructure and properties of a refractory high-entropy alloy after cold working, J. Alloys Compd. 649 (2015) 1110–1123, doi:10.1016/j.jallcom.2015.07.209.
- [139] T. Yang, S. Xia, S. Liu, C. Wang, S. Liu, Y. Zhang, J. Xue, S. Yan, Y. Wang, Effects of AL addition on microstructure and mechanical properties of AlxCrCoFeNi High-entropy alloy, Mater. Sci. Eng. A 648 (2015) 15–22, doi:10.1016/j.msea.2015.09.034.
- [140] H. Chen, A. Kauffmann, B. Gorr, D. Schliephake, C. Seemüller, J.N. Wagner, H.J. Christ, M. Heilmayer, Microstructure and mechanical properties at elevated temperatures of a new Al-containing refractory high-entropy alloy Nb-Mo-Cr-Ti-Al, J. Alloys Compd. 661 (2016) 206–215, doi:10.1016/j.jallcom.2015.11.050.
- [141] E.J. Pickering, R. Muñoz-Moreno, H.J. Stone, N.G. Jones, Precipitation in the equiatomic high-entropy alloy CrMnFeCoNi, Scr. Mater. 113 (2016) 106–109, doi:10.1016/j.scriptamat.2015.10.025.
- [142] S. Maiti, W. Steurer, Structural-disorder and its effect on mechanical properties in single-phase TaNbHFzr high-entropy alloy, Acta Mater. 106 (2016) 87–97, doi:10.1016/j.actamat.2016.01.018.
- [143] Z.M. Jiao, S.G. Ma, M.Y. Chu, H.J. Yang, Z.H. Wang, Y. Zhang, J.W. Qiao, Superior mechanical properties of AlCoCrFeNiTi<sub>x</sub> high-entropy alloys upon dynamic loading, J. Mater. Eng. Perform. 25 (2016) 451–456, doi:10.1007/s11665-015-1869-3.
- [144] G. Dirras, L. Liliensten, P. Djemia, M. Laurent-Brocq, D. Tingaud, J.P. Couzinié, L. Perrière, T. Chauveau, I. Guillot, Elastic and plastic properties of as-cast equimolar TiHFzrTaNb high-entropy alloy, Mater. Sci. Eng. A 654 (2016) 30–38, doi:10.1016/j.msea.2015.12.017.
- [145] P.F. Yu, H. Cheng, L.J. Zhang, H. Zhang, Q. Jing, M.Z. Ma, P.K. Liaw, G. Li, R.P. Liu, Effects of high pressure torsion on microstructures and properties of an Al0.1CoCrFeNi high-entropy alloy, Mater. Sci. Eng. A. 655 (2016) 283–291, doi:10.1016/j.msea.2015.12.085.
- [146] L. Rogal, J. Morgiel, Z. Świątek, F. Czerwiński, Microstructure and mechanical properties of the new Nb25Sc25Ti25Zr25 eutectic high entropy alloy, Mater. Sci. Eng. A 651 (2016) 590–597, doi:10.1016/j.msea.2015.10.071.
- [147] T. Author, I.D. Society, 4, 3, 1 (2013) 1–31.
- [148] C. Li, Y. Xue, M. Hua, T. Cao, L. Ma, L. Wang, Microstructure and mechanical properties of AlxSi0.2CrFeCoNiCu1-x high-entropy alloys, Mater. Des. 90 (2016) 601–609, doi:10.1016/j.matdes.2015.11.013.
- [149] J. Li, Q. Fang, B. Liu, Y. Liu, Y. Liu, Mechanical behaviors of AlCrFeCuNi high-entropy alloys under uniaxial tension via molecular dynamics simulation, RSC Adv. 6 (2016) 76409–76419, doi:10.1039/C6RA16503F.
- [150] Z.J. Jiang, J.Y. He, H.Y. Wang, H.S. Zhang, Z.P. Lu, L.H. Dai, Shock compression response of high entropy alloys, Mater. Res. Lett. 4 (2016) 226–232, doi:10.1080/21663831.2016.1191554.
- [151] I.S. Wani, T. Bhattacharjee, S. Sheikh, P.P. Bhattacharjee, S. Guo, N. Tsuji, Tailoring nanostructures and mechanical properties of AlCoCrFeNi2.1 eutectic high entropy alloy using thermo-mechanical processing, Mater. Sci. Eng. A. 675 (2016) 99–109, doi:10.1016/j.msea.2016.08.048.
- [152] A. Munitz, S. Salhov, S. Hayun, N. Frage, Heat treatment impacts the microstructure and mechanical properties of AlCoCrFeNi high entropy alloy, J. Alloys Compd. 683 (2016) 221–230, doi:10.1016/j.jallcom.2016.05.034.
- [153] H. Zhang, K.W. Siu, W. Liao, Q. Wang, Y. Yang, Y. Lu, In situ mechanical characterization of CoCrCuFeNi high-entropy alloy micro/nano-pillars for their size-dependent mechanical behavior, Mater. Res. Express 3 (2016) 094002, doi:10.1088/2053-1591/3/9/094002.
- [154] N.L. Okamoto, S. Fujimoto, Y. Kambara, M. Kawamura, Z.M.T. Chen, H. Matsunoshita, K. Tanaka, H. Inui, E.P. George, Size effect, critical resolved shear stress, stacking fault energy, and solid solution strengthening in the CrMnFe-CoNi high-entropy alloy, Sci. Rep. 6 (2016) 35863, doi:10.1038/srep35863.
- [155] C.C. Juan, K.K. Tseng, W.L. Hsu, M.H. Tsai, C.W. Tsai, C.M. Lin, S.K. Chen, S.J. Lin, J.W. Yeh, Solution strengthening of ductile refractory HfMoNbTaTiZr high-entropy alloys, Mater. Lett. 175 (2016) 284–287, doi:10.1016/j.matchat.2016.03.133.
- [156] P.J. Bardziński, P. Błyskun, Mechanical properties and structure of rapidly solidified bulk Fe89 - xHf4Ta1Cu1Gd1SixB4 ( $x = 0\text{--}15$ ) and Fe74Hf4Ta1Cu1Gd1LaySi15 - yB4 ( $y = 7$ ) alloys, Mater. Des. 103 (2016) 377–390, doi:10.1016/j.matdes.2016.04.054.
- [157] S. Niu, H. Kou, T. Guo, Y. Zhang, J. Wang, J. Li, Strengthening of nanoprecipitations in an annealed Al0.5CoCrFeNi high entropy alloy, Mater. Sci. Eng. A 671 (2016) 82–86, doi:10.1016/j.msea.2016.06.040.
- [158] A.D. Pogrebnyak, A.A. Bagdasaryan, I.V. Yakushchenko, V.M. Beresnev, The structure and properties of high-entropy alloys and nitride coatings based on them, Russ. Chem. Rev. 83 (2014) 1027–1061, doi:10.1070/RCR4407.
- [159] A.I. Yurkova, V.V. Chernyavskii, V.F. Gorban', Structure and mechanical properties of high-entropy AlCuNiFeTi and AlCuNiFeCr alloys produced by mechanical activation followed by pressure sintering, Powder Metall. Met. Ceram. 55 (2016) 152–163, doi:10.1007/s11106-016-9790-3.
- [160] I. Moravcik, J. Cizek, P. Gavendova, S. Sheikh, S. Guo, I. Dlouhy, Effect of heat treatment on microstructure and mechanical properties of spark plasma sintered AlCoCrFeNiTi0.5 high entropy alloy, Mater. Lett. 174 (2016) 53–56, doi:10.1016/j.matchat.2016.03.077.
- [161] B. Wang, A. Fu, X. Huang, B. Liu, Y. Liu, Z. Li, X. Zan, Mechanical properties and microstructure of the CoCrFeMnNi high entropy alloy under high strain rate compression, J. Mater. Eng. Perform. 25 (2016) 2985–2992, doi:10.1007/s11665-016-2105-5.
- [162] X.C. Li, D. Dou, Z.Y. Zheng, J.C. Li, Microstructure and properties of FeAl-CrNiMo x high-entropy alloys, J. Mater. Eng. Perform. 25 (2016) 2164–2169, doi:10.1007/s11665-016-2060-1.
- [163] Y. Zhang, Y. Liu, Y. Li, X. Chen, H. Zhang, Microstructure and mechanical properties of a refractory HfNbTiVSi0.5 high-entropy alloy composite, Mater. Lett. 174 (2016) 82–85, doi:10.1016/j.matchat.2016.03.092.
- [164] D.H. Lee, M.Y. Seok, Y. Zhao, I.C. Choi, J. He, Z. Lu, J.Y. Suh, U. Ramamurti, M. Kawasaki, T.G. Langdon, J. Il Jang, Spherical nanoindentation creep behavior of nanocrystalline and coarse-grained CoCrFeMnNi high-entropy alloys, Acta Mater. 109 (2016) 314–322, doi:10.1016/j.actamat.2016.02.049.
- [165] F. He, Z. Wang, S. Niu, Q. Wu, J. Li, J. Wang, C.T. Liu, Y. Dang, Strengthening the CoCrFeNiNb0.25 high entropy alloy by FCC precipitate, J. Alloys Compd. 667 (2016) 53–57, doi:10.1016/j.jallcom.2016.01.153.
- [166] J. Li, W. Jia, J. Wang, H. Kou, D. Zhang, E. Beaugnon, Enhanced mechanical properties of a CoCrFeNi high entropy alloy by supercooling method, Mater. Des. 95 (2016) 183–187, doi:10.1016/j.matdes.2016.01.112.
- [167] L. Tian, Z.M. Jiao, G.Z. Yuan, S.G. Ma, Z.H. Wang, H.J. Yang, Y. Zhang, J.W. Qiao, Effect of strain rate on deformation behavior of AlCoCrFeNi high-entropy alloy by nanoindentation, J. Mater. Eng. Perform. 25 (2016) 2255–2260, doi:10.1007/s11665-016-2082-8.
- [168] L. Zhang, P. Yu, H. Cheng, H. Zhang, H. Diao, Y. Shi, B. Chen, P. Chen, R. Feng, J. Bai, Q. Jing, M. Ma, P.K. Liaw, G. Li, R. Liu, Nanoindentation creep behavior of an Al0.3CoCrFeNi high-entropy alloy, Metall. Mater. Trans. A Phys. Metall. Mater. Sci. 47 (2016) 5871–5875, doi:10.1007/s11661-016-3469-8.
- [169] C. Ng, S. Guo, J. Luan, Q. Wang, J. Lu, S. Shi, C.T. Liu, Phase stability and tensile properties of Co-free Al 0.5CrCuFeNi2 high-entropy alloys, J. Alloys Compd. 584 (2014) 530–537, doi:10.1016/j.jallcom.2013.09.105.
- [170] C.C. Juan, M.H. Tsai, C.W. Tsai, W.L. Hsu, C.M. Lin, S.K. Chen, S.J. Lin, J.W. Yeh, Simultaneously increasing the strength and ductility of a refractory high-entropy alloy via grain refining, Mater. Lett. 184 (2016) 200–203, doi:10.1016/j.matchat.2016.08.060.
- [171] K. Jin, W. Guo, C. Lu, M.W. Ullah, Y. Zhang, W.J. Weber, L. Wang, J.D. Poplawsky, H. Bei, Effects of Fe concentration on the ion-irradiation induced defect evolution and hardening in Ni-Fe solid solution alloys, Acta Mater. 121 (2016) 365–373, doi:10.1016/j.actamat.2016.09.025.
- [172] M.J. Jang, S.H. Joo, C.W. Tsai, J.W. Yeh, H.S. Kim, Compressive deformation behavior of CrMnFeCoNi high-entropy alloy, Met. Mater. Int. 22 (2016) 982–986, doi:10.1007/s12540-016-6304-2.
- [173] Z. Wang, I. Baker, Z. Cai, S. Chen, J.D. Poplawsky, W. Guo, The effect of interstitial carbon on the mechanical properties and dislocation substructure evolution in Fe40Ni11.3Mn34.8Al7.5Cr6 high entropy alloys, Acta Mater. 120 (2016) 228–239, doi:10.1016/j.actamat.2016.08.072.
- [174] N.Y. Yurchenko, N.D. Stepanov, D.G. Shaysultanov, M.A. Tikhonovsky, G.A. Salishchev, Effect of Al content on structure and mechanical properties of the AlxCrNbTiVZr ( $x=0, 0.25, 0.5, 1$ ) high-entropy alloys, Mater. Charact. 121 (2016) 125–134, doi:10.1016/j.matchar.2016.09.039.
- [175] H. Jiang, H. Zhang, T. Huang, Y. Lu, T. Wang, T. Li, Microstructures and mechanical properties of Co2MoxNi2VVx eutectic high entropy alloys, Mater. Des. 109 (2016) 539–546, doi:10.1016/j.matdes.2016.07.113.
- [176] J.H. Pi, Z.Z. Wang, X.C. He, Y.Q. Bai, Nanoindentation mechanical properties of a bi-phase Cu29Zr32Ti15Al5Ni19 alloy, J. Mater. Eng. Perform. 25 (2016) 76–82, doi:10.1007/s11665-015-1821-6.
- [177] X.R. Wang, Z.Q. Wang, T.S. Lin, P. He, Microstructure, thermodynamics and compressive properties of AlCrCuNiZrx ( $x = 0, 1$ ) high-entropy alloys, Mater. Sci. Technol. (United Kingdom) 32 (2016) 1289–1295, doi:10.1080/02670836.2015.1117194.
- [178] J.Y. He, H. Wang, H.L. Huang, X.D. Xu, M.W. Chen, Y. Wu, X.J. Liu, T.G. Nieh, K. An, Z.P. Lu, A precipitation-hardened high-entropy alloy with outstanding tensile properties, Acta Mater. 102 (2016) 187–196, doi:10.1016/j.actamat.2015.08.076.
- [179] G. Dirras, H. Couque, L. Liliensten, A. Heczel, D. Tingaud, J.P. Couzinié, L. Perrière, J. Gubicza, I. Guillot, Mechanical behavior and microstructure of Ti20Hf20Zr20Ta20Nb20 high-entropy alloy loaded under quasi-static and dynamic compression conditions, Mater. Charact. 111 (2016) 106–113, doi:10.1016/j.matchar.2015.11.018.
- [180] G.A. Salishchev, M.A. Tikhonovsky, D.G. Shaysultanov, N.D. Stepanov, A.V. Kuznetsov, I.V. Kolodiy, A.S. Tortika, O.N. Senkov, Effect of Mn and v on structure and mechanical properties of high-entropy alloys based on CoCr-FeNi system, J. Alloys Compd. 591 (2014) 11–24, doi:10.1016/j.jallcom.2013.12.210.

- [181] S.G. Ma, Z.M. Jiao, J.W. Qiao, H.J. Yang, Y. Zhang, Z.H. Wang, Strain rate effects on the dynamic mechanical properties of the AlCrCuFeNi<sub>2</sub> high-entropy alloy, *Mater. Sci. Eng. A* 649 (2016) 35–38, doi:[10.1016/j.msea.2015.09.089](https://doi.org/10.1016/j.msea.2015.09.089).
- [182] X.R. Wang, Z.Q. Wang, T.S. Lin, P. He, D.P. Sekulic, Impact of CrSiTi and NiSi on the Thermodynamics, Microstructure, and Properties of AlCoCuFe-Based High-Entropy Alloys, *J. Mater. Eng. Perform.* 25 (2016) 2053–2064, doi:[10.1007/s11665-016-2000-0](https://doi.org/10.1007/s11665-016-2000-0).
- [183] C.F. Lee, T.T. Shun, Effect of Fe content on microstructure and mechanical properties of Al<sub>0.5</sub>CoCrFeNiTi<sub>0.5</sub> high-entropy alloys, *Mater. Charact.* 114 (2016) 179–184, doi:[10.1016/j.matchar.2016.02.018](https://doi.org/10.1016/j.matchar.2016.02.018).
- [184] Z. Fu, W. Chen, H. Wen, D. Zhang, Z. Chen, B. Zheng, Y. Zhou, E.J. Lavernia, Microstructure and strengthening mechanisms in an FCC structured single-phase nanocrystalline Co<sub>25</sub>Ni<sub>25</sub>Fe<sub>25</sub>Al<sub>7</sub>Cu<sub>17.5</sub> high-entropy alloy, *Acta Mater.* 107 (2016) 59–71, doi:[10.1016/j.actamat.2016.01.050](https://doi.org/10.1016/j.actamat.2016.01.050).
- [185] J. Chen, P. Niu, Y. Liu, Y. Lu, X. Wang, Y. Peng, J. Liu, Effect of Zr content on microstructure and mechanical properties of AlCoCrFeNi high entropy alloy, *Mater. Des.* 94 (2016) 39–44, doi:[10.1016/j.matdes.2016.01.033](https://doi.org/10.1016/j.matdes.2016.01.033).
- [186] K.Biswas Tazuddin, N.P. Guroo, Deciphering micro-mechanisms of plastic deformation in a novel single phase fcc-based MnFeCoNiCu high entropy alloy using crystallographic texture, *Mater. Sci. Eng. A* 657 (2016) 224–233, doi:[10.1016/j.msea.2016.01.065](https://doi.org/10.1016/j.msea.2016.01.065).
- [187] S.W. Wu, G. Wang, J. Yi, Y.D. Jia, I. Hussain, Q.J. Zhai, P.K. Liaw, Strong grain-size effect on deformation twinning of an Al<sub>0.1</sub>CoCrFeNi high-entropy alloy, *Mater. Res. Lett.* 5 (2017) 276–283, doi:[10.1080/21663831.2016.1257514](https://doi.org/10.1080/21663831.2016.1257514).
- [188] S.R. Reddy, S. Bapari, P.P. Bhattacharjee, A.H. Chokshi, Superplastic-like flow in a fine-grained equiatomic CoCrFeMnNi high-entropy alloy, *Mater. Res. Lett.* 5 (2017) 408–414, doi:[10.1080/21663831.2017.1305460](https://doi.org/10.1080/21663831.2017.1305460).
- [189] G. Cakmak, Effect of heat treatment on the microstructure, phase distribution, and mechanical properties of AlCoCuFeMnNi high entropy alloy, *Adv. Mater. Sci. Eng.* 2017 (2017) 1950196, 6 pages, doi:[10.1155/2017/1950196](https://doi.org/10.1155/2017/1950196).
- [190] X. Chen, J.Q. Qi, Y.W. Sui, Y.Z. He, F.X. Wei, Q.K. Meng, Z. Sun, Effects of aluminum on microstructure and compressive properties of Al-Cr-Fe-Ni eutectic multi-component alloys, *Mater. Sci. Eng. A* 681 (2017) 25–31, doi:[10.1016/j.msea.2016.11.019](https://doi.org/10.1016/j.msea.2016.11.019).
- [191] H. Huang, Y. Wu, J. He, H. Wang, X. Liu, K. An, W. Wu, Z. Lu, Phase-transformation ductilization of brittle high-entropy alloys via metastability engineering, *Adv. Mater.* 29 (2017) 1–7, doi:[10.1002/adma.201701678](https://doi.org/10.1002/adma.201701678).
- [192] D.K. Matlock, J.G. Speer, Third generation of AHSS: microstructure design concepts, *Microstruct. Texture Steels* (2009) 185–205, doi:[10.1007/978-1-84882-454-6\\_11](https://doi.org/10.1007/978-1-84882-454-6_11).
- [193] C.C. Tasan, M. Diehl, D. Yan, M. Bechtold, F. Roters, L. Schemmann, C. Zheng, N. Peranio, D. Ponge, M. Koyama, K. Tsuzaki, D. Raabe, An overview of dual-phase steels: advances in microstructure-oriented processing and micromechanically guided design, *Annu. Rev. Mater. Res.* 45 (2015) 391–431, doi:[10.1146/annurev-matsci-070214-021103](https://doi.org/10.1146/annurev-matsci-070214-021103).
- [194] R. Kuziak, S. Waengler, Advanced high strength steels for automotive industry: a review, VIII (2008).
- [195] S. Gorse, D.B. Miracle, O.N. Senkov, Mapping the world of complex concentrated alloys, *Acta Mater.* (2017), doi:[10.1016/j.actamat.2017.06.027](https://doi.org/10.1016/j.actamat.2017.06.027).
- [196] B. Gludovatz, A. Hohenwarter, K.V.S. Thurston, H. Bei, Z. Wu, E.P. George, R.O. Ritchie, Exceptional damage-tolerance of a medium-entropy alloy Cr-CoNi at cryogenic temperatures, *Nat. Commun.* 7 (2016) 1–8, doi:[10.1038/ncomms10602](https://doi.org/10.1038/ncomms10602).
- [197] Z. Lei, X. Liu, Y. Wu, H. Wang, S. Jiang, S. Wang, X. Hui, Y. Wu, B. Gault, P. Kontis, D. Raabe, L. Gu, Q. Zhang, H. Chen, H. Wang, J. Liu, K. An, Q. Zeng, T.G. Nieh, Z. Lu, Enhanced strength and ductility in a high-entropy alloy via ordered oxygen complexes, *Nature* 563 (2018) 546–550, doi:[10.1038/s41586-018-0685-y](https://doi.org/10.1038/s41586-018-0685-y).
- [198] H.M. Daoud, A.M. Manzoni, R. Völkli, N. Wanderka, U. Glatzel, Oxidation behavior of Al<sub>8</sub>Co<sub>17</sub>Cr<sub>17</sub>Cu<sub>8</sub>Fe<sub>17</sub>Ni<sub>33</sub>, Al<sub>23</sub>Co<sub>15</sub>Cr<sub>23</sub>Cu<sub>8</sub>Fe<sub>15</sub>Ni<sub>15</sub>, and Al<sub>17</sub>Co<sub><sub>x</sub></sub>
- [199] Z. Li, K.G. Pradeep, Y. Deng, D. Raabe, C.C. Tasan, Metastable high-entropy dual-phase alloys overcome the strength-ductility trade-off, *Nature* 534 (2016) 227–230, doi:[10.1038/nature17981](https://doi.org/10.1038/nature17981).
- [200] S. Wei, J. Kim, C.C. Tasan, Boundary micro-cracking in metastable Fe<sub>45</sub>Mn<sub>35</sub>Co<sub>10</sub>Cr<sub>10</sub> high-entropy alloys, *Acta Mater.* 168 (2019) 76–86, doi:[10.1016/j.actamat.2019.01.036](https://doi.org/10.1016/j.actamat.2019.01.036).
- [201] W. Lu, C.H. Liebscher, G. Dehm, D. Raabe, Z. Li, Bidirectional transformation enables hierarchical nanolaminate dual-phase high-entropy alloys, *Adv. Mater.* 30 (2018) 1–10, doi:[10.1002/adma.201804727](https://doi.org/10.1002/adma.201804727).
- [202] O.N. Senkov, D.B. Miracle, K.J. Chait, Development and exploration of refractory high entropy alloys – A review, (2018). doi:[10.1557/jmr.2018.153](https://doi.org/10.1557/jmr.2018.153).
- [203] A.V. Kuznetsov, D.G. Shaysultanov, N.D. Stepanov, G.A. Salishchev, O.N. Senkov, Tensile properties of an AlCrCuNiFeCo high-entropy alloy in as-cast and wrought conditions, *Mater. Sci. Eng. A* 533 (2012) 107–118, doi:[10.1016/j.msea.2011.11.045](https://doi.org/10.1016/j.msea.2011.11.045).
- [204] P.F. Koshelev, Mechanical properties of materials at low temperatures, *Strength Mater.* 3 (1971) 286–291, doi:[10.1007/BF01527440](https://doi.org/10.1007/BF01527440).
- [205] H. Traub, H. Neuhäuser, C. Schwink, Investigations of the yield region of concentrated CuGe and CuZn single crystals-I. Critical resolved shear stress, slip line formation and the true strain rate, *Acta Metall.* 25 (1977) 437–446, doi:[10.1016/0001-6160\(77\)90234-6](https://doi.org/10.1016/0001-6160(77)90234-6).
- [206] T.H. Wille, W. Gieseke, C.H. Schwink, Quantitative analysis of solution hardening in selected copper alloys, *Acta Metall.* 35 (1987) 2679–2693, doi:[10.1016/0001-6160\(87\)90267-7](https://doi.org/10.1016/0001-6160(87)90267-7).
- [207] M.Z. Butt, Stress equivalence of solid-solution hardening, *J. Phys. Condens. Matter.* 2 (1990) 5797–5808, doi:[10.1088/0953-8984/2/26/017](https://doi.org/10.1088/0953-8984/2/26/017).
- [208] A. Sato, M. Meshii, Solid solution softening and solid solution hardening, *Acta Metall.* 21 (1973) 753–768, doi:[10.1016/0001-6160\(73\)90040-0](https://doi.org/10.1016/0001-6160(73)90040-0).
- [209] P. Pafler, R.W.K. Honeycombe, The plastic deformation of metals. Edward Arnold (Publ.) Ltd., maidenhead, 2nd ed. 1984, 483 p., paperback. price £ 17.50. ISBN 0713134682, *Cryst. Res. Technol.* 20 (2007) 634–634, doi:[10.1002/crat.2170200506](https://doi.org/10.1002/crat.2170200506).
- [210] D. Hull, D.J. Bacon, Dislocations in face-centred cubic metals, in: *Introd. to Dislocations*, 2007: pp. 82–101. doi:[10.1016/b978-075064681-9/50005-5](https://doi.org/10.1016/b978-075064681-9/50005-5).
- [211] A. Gali, E.P. George, Tensile properties of high- and medium-entropy alloys, *Intermetallics* 39 (2013) 74–78, doi:[10.1016/j.intermet.2013.03.018](https://doi.org/10.1016/j.intermet.2013.03.018).
- [212] F. Otto, A. Dlouhý, C. Somsen, H. Bei, G. Eggeler, E.P. George, The influences of temperature and microstructure on the tensile properties of a CoCrFeMnNi high-entropy alloy, *Acta Mater.* 61 (2013) 5743–5755, doi:[10.1016/j.actamat.2013.06.018](https://doi.org/10.1016/j.actamat.2013.06.018).
- [213] A. Haglund, M. Koehler, D. Catooor, E.P. George, V. Keppens, Polycrystalline elastic moduli of a high-entropy alloy at cryogenic temperatures, *Intermetallics* 58 (2015) 62–64, doi:[10.1016/j.intermet.2014.11.005](https://doi.org/10.1016/j.intermet.2014.11.005).
- [214] G. Laplanche, P. Gadaud, O. Horst, F. Otto, G. Eggeler, E.P. George, Temperature dependences of the elastic moduli and thermal expansion coefficient of an equiatomic, single-phase CoCrFeMnNi high-entropy alloy, *J. Alloys Compd.* 623 (2015) 348–353, doi:[10.1016/j.jallcom.2014.11.061](https://doi.org/10.1016/j.jallcom.2014.11.061).
- [215] G. Laplanche, P. Gadaud, C. Bärsch, K. Demtröder, C. Reinhart, J. Schreuer, E.P. George, Elastic moduli and thermal expansion coefficients of medium-entropy subsystems of the CrMnFeCoNi high-entropy alloy, *J. Alloys Compd.* 746 (2018) 244–255, doi:[10.1016/j.jallcom.2018.02.251](https://doi.org/10.1016/j.jallcom.2018.02.251).
- [216] N.F. Mott, F.R.N. Nabarro, An attempt to estimate the degree of precipitation hardening, with a simple model, *Proc. Phys. Soc.* (1940).
- [217] R.L. Fleischer, Solution hardening by interaction of impurity gradients and dislocations, *Acta Metall.* 8 (1960) 32–35, doi:[10.1016/0001-6160\(60\)90137-1](https://doi.org/10.1016/0001-6160(60)90137-1).
- [218] R. HONEYCOMBE, The effect of temperature and alloying additions on the deformation of metal crystals, *Prog. Mater. Sci.* 9 (2003) 95–130, doi:[10.1016/0079-6425\(61\)90026-3](https://doi.org/10.1016/0079-6425(61)90026-3).
- [219] C. Varvenne, A. Luque, W.A. Curtin, Erratum: corrigendum to “theory of strengthening in fcc high entropy alloys” (Acta Materialia (2016) 118 (164–176)(S1359645416305481)(10.1016/j.actamat.2016.07.040)), *Acta Mater.* 119 (2016) 242, doi:[10.1016/j.actamat.2016.08.069](https://doi.org/10.1016/j.actamat.2016.08.069).
- [220] J.W. Yeh, Physical metallurgy of high-entropy alloys, *JOM* 67 (2015) 2254–2261, doi:[10.1007/s11837-015-1583-5](https://doi.org/10.1007/s11837-015-1583-5).
- [221] W.H. Liu, Y. Wu, J.Y. He, T.G. Nieh, Z.P. Lu, Grain growth and the Hall-Petch relationship in a high-entropy FeCrNiCoMn alloy, *Scr. Mater.* 68 (2013) 526–529, doi:[10.1016/j.scriptamat.2012.12.002](https://doi.org/10.1016/j.scriptamat.2012.12.002).
- [222] Z.C. Cordero, B.E. Knight, C.A. Schuh, Six decades of the Hall-Petch effect – a survey of grain-size strengthening studies on pure metals, *Int. Mater. Rev.* 61 (2016) 495–512, doi:[10.1080/09506608.2016.1191808](https://doi.org/10.1080/09506608.2016.1191808).
- [223] Z. Wu, H. Bei, F. Otto, G.M. Pharr, E.P. George, Recovery, recrystallization, grain growth and phase stability of a family of FCC-structured multi-component equiatomic solid solution alloys, *Intermetallics* 46 (2014) 131–140, doi:[10.1016/j.intermet.2013.10.024](https://doi.org/10.1016/j.intermet.2013.10.024).
- [224] L. Patriarca, A. Ojha, H. Sehitoglu, Y.I. Chumlyakov, Slip nucleation in single crystal FeNiCoCrMn high entropy alloy, *Scr. Mater.* 112 (2016) 54–57, doi:[10.1016/j.scriptamat.2015.09.009](https://doi.org/10.1016/j.scriptamat.2015.09.009).
- [225] I.V. Kireeva, Y.I. Chumlyakov, Z.V. Pobedennaya, I.V. Kuksgauzen, I. Karaman, Orientation dependence of twinning in single crystalline CoCrFeMnNi high-entropy alloy, *Mater. Sci. Eng. A* 705 (2017) 176–181, doi:[10.1016/j.msea.2017.08.065](https://doi.org/10.1016/j.msea.2017.08.065).
- [226] Z. Wu, Y.F. Gao, H. Bei, Single crystal plastic behavior of a single-phase, face-center-cubic-structured, equiatomic FeNiCrCo alloy, *Scr. Mater.* 109 (2015) 108–112, doi:[10.1016/j.scriptamat.2015.07.031](https://doi.org/10.1016/j.scriptamat.2015.07.031).
- [227] W. Abuzaid, H. Sehitoglu, Critical resolved shear stress for slip and twin nucleation in single crystalline FeNiCoCrMn high entropy alloy, *Mater. Charact.* 129 (2017) 288–299, doi:[10.1016/j.matchar.2017.05.014](https://doi.org/10.1016/j.matchar.2017.05.014).
- [228] I. Kireeva, Y. Chumlyakov, Z. Pobedennaya, D. Kuksgauzen, I. Karaman, H. Sehitoglu, Mechanisms of plastic deformation in [1-11]-oriented single crystals of FeNiMnCrCo high entropy alloy, in: *AIP Conf. Proc.*, 2016, doi:[10.1063/1.4966383](https://doi.org/10.1063/1.4966383).
- [229] I.V. Kireeva, Y.I. Chumlyakov, Z.V. Pobedennaya, A.V. Vyrodova, I. Karaman, Twinning in [001]-oriented single crystals of CoCrFeMnNi high-entropy alloy at tensile deformation, *Mater. Sci. Eng. A* 713 (2018) 253–259, doi:[10.1016/j.msea.2017.12.059](https://doi.org/10.1016/j.msea.2017.12.059).
- [230] A. Gali, E.P. George, Tensile properties of high- and medium-entropy alloys, *Intermetallics* 39 (2013) 74–78, doi:[10.1016/j.intermet.2013.03.018](https://doi.org/10.1016/j.intermet.2013.03.018).
- [231] B. Uzer, S. Picak, J. Liu, T. Jozaghi, D. Canadinc, I. Karaman, Y.I. Chumlyakov, I. Kireeva, On the mechanical response and microstructure evolution of Ni-C-oCr single crystalline medium entropy alloys, *Mater. Res. Lett.* 6 (2018) 442–449, doi:[10.1080/21663831.2018.1478331](https://doi.org/10.1080/21663831.2018.1478331).
- [232] S.G. Ma, S.F. Zhang, J.W. Qiao, Z.H. Wang, M.C. Gao, Z.M. Jiao, H.J. Yang, Y. Zhang, Superior high tensile elongation of a single-crystal CoCrFeNiAl 0.3 high-entropy alloy by Bridgman solidification, *Intermetallics* 54 (2014) 104–109, doi:[10.1016/j.intermet.2014.05.018](https://doi.org/10.1016/j.intermet.2014.05.018).
- [233] I.V. Kireeva, Y.I. Chumlyakov, Z.V. Pobedennaya, A.V. Vyrodova, I.V. Kuksgauzen, D.A. Kuksgauzen, Orientation and temperature dependence of a planar slip and twinning in single crystals of Al0.3CoCrFeNi high-entropy alloy, *Mater. Sci. Eng. A* 737 (2018) 47–60, doi:[10.1016/j.msea.2018.09.025](https://doi.org/10.1016/j.msea.2018.09.025).

- [234] H.Y. Yasuda, K. Shigeno, T. Nagase, Dynamic strain aging of Al<sub>0.3</sub>CoCrFeNi high entropy alloy single crystals, *Scr. Mater.* 108 (2015) 80–83, doi:10.1016/j.scriptamat.2015.06.022.
- [235] P. Haasen, Plastic deformation of nickel single crystals at low temperatures, *Philos. Mag. 3* (1958) 384–418, doi:10.1080/14786435808236826.
- [236] R. Labusch, A Statistical Theory of Solid Solution Hardening, *Phys. Status Solidi* 41 (1970) 659–669, doi:10.1002/pssb.19700410221.
- [237] C. Varvenne, A. Luque, W.A. Curtin, Theory of strengthening in fcc high entropy alloys, *Acta Mater.* 118 (2016) 164–176, doi:10.1016/j.actamat.2016.07.040.
- [238] M. Kang, J.W. Won, J.B. Kwon, Y.S. Na, Intermediate strain rate deformation behavior of a CoCrFeMnNi high-entropy alloy, *Mater. Sci. Eng. A* 707 (2017) 16–21, doi:10.1016/j.msea.2017.09.026.
- [239] J.M. Park, J. Moon, J.W. Bae, M.J. Jang, J. Park, S. Lee, H.S. Kim, Strain rate effects of dynamic compressive deformation on mechanical properties and microstructure of CoCrFeMnNi high-entropy alloy, *Mater. Sci. Eng. A* 719 (2018) 155–163, doi:10.1016/j.msea.2018.02.031.
- [240] R. Bobbili, V. Madhu, A modified Johnson-Cook model for FeCoNiCr high entropy alloy over a wide range of strain rates, *Mater. Lett.* 218 (2018) 103–105, doi:10.1016/j.matlet.2018.01.163.
- [241] N. Kumar, Q. Ying, X. Nie, R.S. Mishra, Z. Tang, P.K. Liaw, R.E. Brennan, K.J. Doherty, K.C. Cho, High strain-rate compressive deformation behavior of the Al<sub>0.1</sub>CrFeCoNi high entropy alloy, *Mater. Des.* 86 (2015) 598–602, doi:10.1016/j.matedes.2015.07.161.
- [242] Z. Li, S. Zhao, H. Diao, P.K. Liaw, M.A. Meyers, High-velocity deformation of Al<sub>0.3</sub>CoCrFeNi high-entropy alloy: Remarkable resistance to shear failure, *Sci. Rep.* 7 (2017), doi:10.1038/srep42742.
- [243] G. Laplanche, A. Kostka, O.M. Horst, G. Eggeler, E.P. George, Microstructure evolution and critical stress for twinning in the CrMnFeCoNi high-entropy alloy, *Acta Mater.* 118 (2016) 152–163, doi:10.1016/j.actamat.2016.07.038.
- [244] Z.J. Zhang, M.M. Mao, J. Wang, B. Gludovatz, Z. Zhang, S.X. Mao, E.P. George, Q. Yu, R.O. Ritchie, Nanoscale origins of the damage tolerance of the high-entropy alloy CrMnFeCoNi, *Nat. Commun.* 6 (2015) 1–6, doi:10.1038/ncomms10143.
- [245] S. Huang, W. Li, S. Lu, F. Tian, J. Shen, E. Holmström, L. Vitos, Temperature dependent stacking fault energy of FeCrCoNiMn high entropy alloy, *Scr. Mater.* 108 (2015) 44–47, doi:10.1016/j.scriptamat.2015.05.041.
- [246] T.M. Smith, M.S. Hooshmand, B.D. Esser, F. Otto, D.W. McComb, E.P. George, M. Ghazisaeidi, M.J. Mills, Atomic-scale characterization and modeling of 60°dislocations in a high-entropy alloy, *Acta Mater.* (2016), doi:10.1016/j.actamat.2016.03.045.
- [247] D.B. Williams, C.B. Carter, in: *Transmission Electron Microscopy - A Textbook for Materials Science, Part 1: Basics*, Second Ed., Springer, 2009, p. 468.
- [248] C.B. Carter, The extension of jogs on dissociated dislocations in FCC metals, *Phys. Status Solidi A* 54 (1979) 395–406.
- [249] D.J.H. Cockayne, M.L. Jenkins, I.I.F. Ray, The measurement of stacking-fault energies of pure face-centered cubic metals, *Philos. Mag.* 24 (1971) 1383–1392.
- [250] S. Zhao, G.M. Stocks, Y. Zhang, Stacking fault energies of face-centered cubic concentrated solid solution alloys, *Acta Mater.* (2017), doi:10.1016/j.actamat.2017.05.001.
- [251] N. Bernstein, E.B. Tadmor, Tight-binding calculations of stacking energies and twinnability in FCC metals, *Phys. Rev. B Condens. Matter Mater. Phys.* 69 (2004), doi:10.1103/PhysRevB.69.094116.
- [252] E.B. Tadmor, N. Bernstein, A first-principles measure for the twinnability of FCC metals, *J. Mech. Phys. Solids* 52 (2004) 2507–2519, doi:10.1016/j.jmps.2004.05.002.
- [253] D. Ma, B. Grabowski, F. Körmann, J. Neugebauer, D. Raabe, Ab initio thermodynamics of the CoCrFeMnNi high entropy alloy: importance of entropy contributions beyond the configurational one, *Acta Mater.* 100 (2015) 90–97, doi:10.1016/j.actamat.2015.08.050.
- [254] C.L. Tracy, S. Park, D.R. Rittman, S.J. Zinkle, H. Bei, M. Lang, R.C. Ewing, W.L. Mao, High pressure synthesis of a hexagonal close-packed phase of the high-entropy alloy CrMnFeCoNi, *Nat. Commun.* 8 (2017), doi:10.1038/ncomms15634.
- [255] F. Zhang, Y. Wu, H. Lou, Z. Zeng, V.B. Prakapenka, E. Greenberg, Y. Ren, J. Yan, J.S. Okasinski, X. Liu, Y. Liu, Q. Zeng, Z. Lu, Polymorphism in a high-entropy alloy, *Nat. Commun.* 8 (2017), doi:10.1038/ncomms15687.
- [256] S.F. Liu, Y. Wu, H.T. Wang, J.Y. He, J.B. Liu, C.X. Chen, X.J. Liu, H. Wang, Z.P. Lu, Stacking fault energy of face-centered-cubic high entropy alloys, *Intermetallics* 93 (2018) 269–273, doi:10.1016/j.intermet.2017.10.004.
- [257] G. Laplanche, A. Kostka, C. Reinhart, J. Hunfeld, G. Eggeler, E.P. George, Reasons for the superior mechanical properties of medium-entropy CrCoNi compared to high-entropy CrMnFeCoNi, *Acta Mater.* (2017), doi:10.1016/j.actamat.2017.02.036.
- [258] Y.T. Zhu, X.Z. Liao, X.L. Wu, Deformation twinning in nanocrystalline materials, *Prog. Mater. Sci.* 57 (2012) 1–62, doi:10.1016/j.pmatsci.2011.05.001.
- [259] L. Remy, A. Pineau, Twinning and strain-induced FCC to HCP transformation on the mechanical properties of Co-No-Cr-Mo alloys, *Mater. Sci. Eng.* 26 (1976) 123–132.
- [260] L. Remy, Kinetics of F.C.C. deformation twinning and its relationship to stress-strain behaviour, *Acta Metall.* 26 (1978) 443–451, doi:10.1016/0001-6160(78)90170-0.
- [261] K.S. Raghavan, A.S. Sastri, M.J. Marcinkovski, Nature of the work-hardening behavior in Hadfield's manganese steel, *Trans. Metall. Soc. AIME* 245 (1969) 1569–1576.
- [262] I. Karaman, H. Sehitoglu, A.J. Beaudoev, Y.I. Chumlyakov, H.J. Maier, C.N. Tomé, Modeling the deformation behavior of Hadfield steel single and polycrystals due to twinning and slip, *Acta Mater.* 48 (2000) 2031–2047, doi:10.1016/S1359-6454(00)00051-3.
- [263] O. Bouaziz, N. Gueltol, Modelling of TWIP effect on work-hardening, *Mater. Sci. Eng. A* (2001) 246–249 319–321, doi:10.1016/S0921-5093(00)02019-0.
- [264] Z. Zhang, H. Sheng, Z. Wang, B. Gludovatz, Z. Zhang, E.P. George, Q. Yu, S.X. Mao, R.O. Ritchie, Dislocation mechanisms and 3D twin architectures generate exceptional strength-ductility-toughness combination in CrCoNi medium-entropy alloy, *Nat. Commun.* 8 (2017), doi:10.1038/ncomms14390.
- [265] M.A. Meyers, O. Vöhringer, V.A. Lubarda, The onset of twinning in metals: A constitutive description, *Acta Mater.* 49 (2001) 4025–4039, doi:10.1016/S1359-6454(01)00300-7.
- [266] N. Stepanov, M. Tikhonovsky, N. Yurchenko, D. Zyabkin, M. Klimova, S. Zherebtsov, A. Efimov, G. Salishchev, Effect of cryo-deformation on structure and properties of CoCrFeNiMn high-entropy alloy, *Intermetallics* 59 (2015) 8–17, doi:10.1016/j.intermet.2014.12.004.
- [267] E. El-Danaf, S.R. Kalidindi, R.D. Doherty, Influence of grain size and stacking-fault energy on deformation twinning in fcc metals, *Metall. Mater. Trans. A Phys. Metall. Mater. Sci.* 30 (1999) 1223–1233, doi:10.1007/s11661-999-0272-9.
- [268] S.J. Sun, Y.Z. Tian, H.R. Lin, H.J. Yang, X.G. Dong, Y.H. Wang, Z.F. Zhang, Transition of twinning behavior in CoCrFeMnNi high entropy alloy with grain refinement, *Mater. Sci. Eng. A* 712 (2018) 603–607, doi:10.1016/j.msea.2017.12.022.
- [269] I.V. Kireeva, Y.I. Chumlyakov, Z.V. Pobedennaya, Y.N. Platonova, I.V. Kuksaguzen, D.A. Kuksaguzen, V.V. Poklonov, I. Karaman, H. Sehitoglu, Slip and twinning in the [1–49]-oriented single crystals of a high-entropy alloy, *Russ. Phys. J.* 59 (2016) 1242–1250, doi:10.1007/s11182-016-0898-1.
- [270] Y. Deng, C.C. Tasan, K.G. Pradeep, H. Springer, A. Kostka, D. Raabe, Design of a twinning-induced plasticity high entropy alloy, *Acta Mater.* 94 (2015) 124–133, doi:10.1016/j.actamat.2015.04.014.
- [271] L. Qi, D.C. Chrzan, Tuning ideal tensile strengths and intrinsic ductility of BCC refractory alloys, *Phys. Rev. Lett.* 115503 (2014) 1–5, doi:10.1103/PhysRevLett.112.115503.
- [272] J.W. Morris, Z. Guo, C.R. Krenn, Y. Kim, The limits of strength and toughness in steel, *ISIJ Int.* 41 (2001) 599–611.
- [273] P.K. Senkov, Wilks O.N., Miracle G.B., Chuang D.B., Liaw C.P., Refractory high-entropy alloys, *Intermetallics* 18 (2010) 1758–1765.
- [274] Y.D. Wu, Y.H. Cai, T. Wang, J.J. Si, J. Zhu, Y.D. Wang, X.D. Hui, A refractory Hf 25 Nb 25 Ti 25 Zr 25 high-entropy alloy with excellent structural stability and tensile properties, *Mater. Lett.* 130 (2014) 277–280.
- [275] S. Sheikh, S. Shafei, Q. Hu, J. Ahlström, C. Persson, J. Veselý, J. Zyka, U. Klement, S. Guo, Alloy design for intrinsically ductile refractory high-entropy alloys, *J. Appl. Phys.* (2016) 164902, doi:10.1063/1.4966659.
- [276] E. Fazakas, V. Zadorozhny, L.K. Varga, A. Inoue, D.V. Louzguine-Luzgin, F. Tian, L. Vitos, Experimental and theoretical study of Ti20Zr20Hf20Nb20X0 (X = v or Cr) refractory high-entropy alloys, *Int. J. Refract. Met. Hard Mater.* 47 (2014) 131–138, doi:10.1016/j.ijrmhm.2014.07.009.
- [277] O.N. Senkov, J.M. Scott, S.V. Senkova, D.B. Miracle, C.F. Woodward, Microstructure and room temperature properties of a high-entropy TaNbHfZrTi alloy, *J. Alloys Compd.* 509 (2011) 6043–6048, doi:10.1016/j.jallcom.2011.02.171.
- [278] O.N. Senkov, S.L. Semiatin, Microstructure and properties of a refractory high-entropy alloy after cold working, *J. Alloys Compd.* 649 (2015) 1110–1123, doi:10.1016/j.jallcom.2015.07.209.
- [279] J.P. Couziné, G. Dirras, L. Perrière, T. Chauveau, E. Leroy, Y. Champion, I. Guillot, Microstructure of a near-equitmolar refractory high-entropy alloy, *Mater. Lett.* 126 (2014) 285–287, doi:10.1016/j.matlet.2014.04.062.
- [280] N.D. Stepanov, N.Y. Yurchenko, S.V. Zherebtsov, M.A. Tikhonovsky, G.A. Salishchev, Aging behavior of the HfNbTaTiZr high entropy alloy, *Mater. Lett.* 211 (2018) 87–90, doi:10.1016/j.matlet.2017.09.094.
- [281] M. Semchyshen, R.Q. Barr, Research on new methods for improving the ductility of molybdenum, *J. Less Common Metals* 11 (1966) 1–13.
- [282] A. Kumar, B.L. Eyre, Grain-boundary segregation and intergranular fracture in molybdenum, *Proc. R. Soc. Lond. A* 370 (1980) 431–458.
- [283] O.N. Senkov, J.M. Scott, S.V. Senkova, F. Meisenkothen, D.B. Miracle, C.F. Woodward, Microstructure and elevated temperature properties of a refractory TaNbHfZrTi alloy, *J. Mater. Sci.* 47 (2012) 4062–4074, doi:10.1007/s10853-012-6260-2.
- [284] G.P.M. Leyson, W.A. Curtin, L.G. Hector, C.F. Woodward, Quantitative prediction of solute strengthening in aluminium alloys, *Nat. Mater.* 9 (2010) 750–755, doi:10.1038/978-3-642-37484-5\_29.
- [285] U.F. Kocks, A.S. Argon, M.F. Ashby, Models for macroscopic slip, *Prog. Mater. Sci.* 19 (1975).
- [286] H. Mecking, U.F. Kocks, Kinetics of flow and strain hardening, *Acta Metall.* 29 (1981) 1865–1875, doi:10.1016/0001-6160(81)90112-7.
- [287] E. Voce, The relationship between stress and strain for homogeneous deformation, *J. Inst. Met.* 74 (1948) 537–562.
- [288] P. Haasen, *Physical Metallurgy*, 3rd ed., Cambridge University Press, Cambridge, 1996.
- [289] M. Beyramli Kiviy, M. Asle Zaeem, Generalized stacking fault energies, ductilities, and twinnabilities of CoCrFeNi-based face-centered cubic high entropy alloys, *Scr. Mater.* 139 (2017) 83–86, doi:10.1016/j.scriptamat.2017.06.014.
- [290] I. Bleskov, T. Hickel, J. Neugebauer, A. Ruban, Impact of local magnetism on stacking fault energies: a first-principles investigation for FCC iron, *Phys. Rev. B* 93 (2016), doi:10.1103/PhysRevB.93.214115.

- [291] S.I. Rao, C. Woodward, T.A. Parthasarathy, O. Senkov, Atomistic simulations of dislocation behavior in a model FCC multicomponent concentrated solid solution alloy, *Acta Mater.* 134 (2017) 188–194, doi:10.1016/j.actamat.2017.05.071.
- [292] X.W. Zhou, H.N.G. Wadley, R.A. Johnson, D.J. Larson, N. Tabat, A. Cerezo, A.K. Petford-Long, G.D.W. Smith, P.H. Clifton, R.L. Martens, T.F. Kelly, Atomic scale structure of sputtered metal multilayers, *Acta Mater.* (2001), doi:10.1016/S1359-6454(01)00287-7.
- [293] S.I. Rao, B. Akdim, E. Antillon, C. Woodward, T.A. Parthasarathy, O.N. Senkov, Modeling solution hardening in BCC refractory complex concentrated alloys: NbTiZr, Nb<sub>1.5</sub>TiZr<sub>0.5</sub> and Nb<sub>0.5</sub>TiZr<sub>1.5</sub>, *Acta Mater.* 168 (2019), doi:10.1016/j.actamat.2019.02.013.
- [294] M.E. Ford, R. Drautz, T. Hammerschmidt, D.G. Pettifor, Convergence of an analytic bond-order potential for collinear magnetism in Fe, *Model. Simul. Mater. Sci. Eng.* 22 (2014), doi:10.1088/0965-0393/22/3/034005.
- [295] C. Teijeiro, T. Hammerschmidt, B. Seiser, R. Drautz, G. Sutmann, Complexity analysis of simulations with analytic bond-order potentials, *Model. Simul. Mater. Sci. Eng.* 24 (2016), doi:10.1088/0965-0393/24/2/025008.
- [296] D. Perez, B.P. Uberuaga, A.F. Voter, The parallel replica dynamics method - coming of age, *Comput. Mater. Sci.* 100 (2015) 90–103, doi:10.1016/j.commatsci.2014.12.011.
- [297] R.J. Zamora, B.P. Uberuaga, D. Perez, A.F. Voter, The modern temperature-accelerated dynamics approach, *Annu. Rev. Chem. Biomol. Eng.* 7 (2016) 87–110, doi:10.1146/annurev-chembioeng-080615-033608.
- [298] G. Henkelman, B.P. Uberuaga, H. Jónsson, Climbing image nudged elastic band method for finding saddle points and minimum energy paths, *J. Chem. Phys.* (2000), doi:10.1063/1.1329672.
- [299] A. Samanta, E. Weinan, Optimization-based string method for finding minimum energy path, *Commun. Comput. Phys.* (2013), doi:10.4208/cicp.220212\_030812a.
- [300] S. Saroukhani, D.H. Warner, Investigating dislocation motion through a field of solutes with atomistic simulations and reaction rate theory, *Acta Mater.* 128 (2017) 77–86, doi:10.1016/j.actamat.2017.02.001.
- [301] G. Esteban-Manzanares, E. Martínez, J. Segurado, L. Capolungo, J. LLorca, An atomistic investigation of the interaction of dislocations with Guinier-Preston zones in Al-Cu alloys, *Acta Mater.* 162 (2019) 189–201, doi:10.1016/j.actamat.2018.09.052.
- [302] C. Varvenne, A. Luque, W.G. Nöhring, W.A. Curtin, Average-atom interatomic potential for random alloys, *Phys. Rev. B* 93 (2016), doi:10.1103/PhysRevB.93.104201.
- [303] S.S. Sohn, A. Kwiatkowski da Silva, Y. Ikeda, F. Körmann, W. Lu, W.S. Choi, B. Gault, D. Ponge, J. Neugebauer, D. Raabe, Ultrastrong medium-entropy single-phase alloys designed via severe lattice distortion, *Adv. Mater.* 31 (2019), doi:10.1002/adma.201807142.
- [304] G.P.M. Leyson, L.G. Hector, W.A. Curtin, Solute strengthening from first principles and application to aluminum alloys, *Acta Mater.* 60 (2012) 3873–3884, doi:10.1016/j.actamat.2012.03.037.
- [305] T. Uesugi, K. Higashi, First-principles studies on lattice constants and local lattice distortions in solid solution aluminum alloys, *Comput. Mater. Sci.* (2013), doi:10.1016/j.commatsci.2012.08.037.
- [306] I. Toda-Caraballo, P.E.J. Rivera-Díaz-Del-Castillo, Modelling solid solution hardening in high entropy alloys, *Acta Mater.* (2015), doi:10.1016/j.actamat.2014.11.014.
- [307] B. Yin, W.A. Curtin, First-principles-based prediction of yield strength in the RhIrPdPtNiCu high-entropy alloy, *NPJ Comput. Mater.* 5 (2019), doi:10.1038/s41524-019-0151-x.
- [308] N.A. Sakhovova, J.V. Fernandes, J.M. Antunes, M.C. Oliveira, Comparison between Berkovich, Vickers and conical indentation tests: a three-dimensional numerical simulation study, *Int. J. Solids Struct.* (2009), doi:10.1016/j.ijsolstr.2008.10.032.
- [309] Z.C. Cordero, B.E. Knight, C.A. Schuh, Six decades of the Hall-Petch effect – a survey of grain-size strengthening studies on pure metals, *Int. Mater. Rev.* 61 (2016) 495–512, doi:10.1080/09506608.2016.1191808.
- [310] R.L. Fleischer, Substitutional solution hardening, *Acta Metall.* 11 (1963) 1867–1868, doi:10.1016/0001-6160(66)90045-9.
- [311] A. Argon, Strengthening mechanisms in crystal plasticity, Oxford University Press, Oxford, 2008, doi:10.1093/acprof:oso/9780198516002.001.0001.
- [312] G.P.M. Leyson, L.G. Hector, W.A. Curtin, First-principles prediction of yield stress for basal slip in Mg-Al alloys, *Acta Mater.* 60 (2012) 5197–5203, doi:10.1016/j.actamat.2012.06.020.
- [313] C. Varvenne, G.P.M. Leyson, M. Ghazisaeidi, W.A. Curtin, Solute strengthening in random alloys, *Acta Mater.* 124 (2017) 660–683, doi:10.1016/j.actamat.2016.09.046.
- [314] C. Varvenne, W.A. Curtin, Strengthening of high entropy alloys by dilute solute additions: CoCrFeNiAlx and CoCrFeNiMnAlx alloys, *Scr. Mater.* 138 (2017) 92–95, doi:10.1016/j.scriptamat.2017.05.035.
- [315] S. Sohn, Y. Liu, J. Liu, P. Gong, S. Prades-Rodel, A. Blatter, B.E. Scanley, C.C. Broadbridge, J. Schroers, Noble metal high entropy alloys, *Scr. Mater.* 126 (2017) 29–32, doi:10.1016/j.scriptamat.2016.08.017.
- [316] M. Laurent-Brocq, L. Perrière, R. Pirès, F. Prima, P. Vermaut, Y. Champion, From diluted solid solutions to high entropy alloys: on the evolution of properties with composition of multi-components alloys, *Mater. Sci. Eng. A* (2017), doi:10.1016/j.msea.2017.04.079.
- [317] G. Bracc, M. Laurent-Brocq, C. Varvenne, L. Perriere, W.A. Curtin, J.-M. Joubert, Combining experiments and modeling to explore solid-solution strengthening of high and medium entropy alloys, *Acta Mater.* 177 (2019) 266–279, doi:10.1016/j.actamat.2019.06.050.
- [318] G.P.M. Leyson, W.A. Curtin, Solute strengthening at high temperatures, *Model. Simul. Mater. Sci. Eng.* (2016), doi:10.1088/0965-0393/24/6/065005.
- [319] N.L. Okamoto, K. Yuge, K. Tanaka, H. Inui, E.P. George, Atomic displacement in the CrMnFeCoNi high-entropy alloy - A scaling factor to predict solid solution strengthening, *AlP Adv.* 6 (2016), doi:10.1063/1.4971371.
- [320] H.S. Oh, D. Ma, G.P. Leyson, B. Grabowski, E.S. Park, F. Kormann, D. Raabe, Lattice distortions in the FeCoNiCrMn high entropy alloy studied by theory and experiment, *Entropy* (2016), doi:10.3390/e18090321.
- [321] W.G. Noehring, W.A. Curtin, Correlation of microdistortions with misfit volumes in High Entropy Alloys, *Scr. Mater.* 168 (2019) 119–123, doi:10.1016/j.scriptamat.2019.04.012.
- [322] H. Yao, J.W. Qiao, M.C. Gao, J.A. Hawk, S.G. Ma, H. Zhou, MoNbTaV medium-entropy alloy, *Entropy* (2016), doi:10.3390/e18050189.
- [323] H.W. Yao, J.W. Qiao, M.C. Gao, J.A. Hawk, S.G. Ma, H.F. Zhou, Y. Zhang, NbTaV-(Ti,W) refractory high-entropy alloys: experiments and modeling, *Mater. Sci. Eng. A* (2016), doi:10.1016/j.msea.2016.07.102.
- [324] H. Suzuki, *Dislocations in Solids*, 4, North-Holland Publishing Company, Amsterdam, 1979.
- [325] A. Hattendorf, H. Buechner, *Plastic behaviour of FeP single crystals*, *Z. Fuer Met.* 81 (1990) 739–748.
- [326] D.R. Trinkle, C. Woodward, The chemistry of deformation: how solutes soften pure metals, *Science* 310 (2005) 1665–1667, doi:10.1126/science.1118616.
- [327] S.I. Rao, C. Varvenne, C. Woodward, T.A. Parthasarathy, D. Miracle, Acta materialia atomistic simulations of dislocations in a model BCC multicomponent concentrated solid solution alloy, *Acta Mater.* 125 (2017) 311–320, doi:10.1016/j.actamat.2016.12.011.
- [328] F.G. Courty, M. Kaufman, A.J. Clarke, Solid-solution strengthening in refractory high entropy alloys, *Acta Mater.* 175 (2019) 66–81, doi:10.1016/j.actamat.2019.06.006.
- [329] S.I. Rao, E. Antillon, C. Woodward, B. Akdim, T.A. Parthasarathy, O.N. Senkov, Solution hardening in body-centered cubic quaternary alloys interpreted using Suzuki's kink-solute interaction model, *Scr. Mater.* 165 (2019) 103–106, doi:10.1016/j.scriptamat.2019.02.012.
- [330] F. Maresca, W.A. Curtin, Theory of screw dislocation strengthening in random BCC alloys from dilute to High-Entropy alloys, *Acta Mater.* 182 (2020) 144–162, doi:10.1016/j.actamat.2019.10.007.
- [331] S.I. Rao, C. Woodward, R. Akdim, E. Antillon, T.A. Parthasarathy, O.N. Senkov, Estimation of diffusional effects on solution hardening at high temperatures in single phase compositionally complex body centered cubic alloys, *Scr. Mater.* 172 (2019) 135–137, doi:10.1016/j.scriptamat.2019.07.025.
- [332] F. Maresca, W.A. Curtin, Mechanistic origin of high strength in refractory BCC high entropy alloys up to 1900K, *Acta Mater.* 182 (2020) 235–249, doi:10.1016/j.actamat.2019.10.015.
- [333] Y. Zeng, X. Cai, M. Koslowski, Effects of the stacking fault energy fluctuations on the strengthening of alloys, *Acta Mater.* 164 (2019) 1–11, doi:10.1016/j.actamat.2018.09.066.
- [334] L. Zhang, Y. Xiang, J. Han, D.J. Srolovitz, The effect of randomness on the strength of high-entropy alloys, *Acta Mater.* 166 (2019) 424–434, doi:10.1016/j.actamat.2018.12.032.
- [335] W.G. Noehring, W.A. Curtin, Cross-slip of long dislocations in FCC solid solutions, *Acta Mater.* 158 (2018) 95–117, doi:10.1016/j.actamat.2018.05.027.
- [336] E. Rodary, D. Rodney, L. Provile, Y. Brechet, G. Martin, Dislocation glide in model Ni(Al) solid solutions by molecular dynamics, *Phys. Rev. B* 70 (2004) 054111, doi:10.1103/PhysRevB.70.054111.
- [337] L. Provile, D. Rodney, Y. Brechet, G. Martin, Atomic-scale study of dislocation glide in a model solid solution, *Philos. Mag.* 86 (2006) 3893–3920, doi:10.1080/14786430600567721.
- [338] E. Antillon, C. Woodward, S.I. Rao, B. Akdim, T.A. Parthasarathy, A molecular dynamics technique for determining energy landscapes as a dislocation percolates through a field of solutes, *Acta Mater.* 166 (2019) 658–676, doi:10.1016/j.actamat.2018.12.037.
- [339] Y. Ikeda, B. Grabowski, F. Körmann, Ab initio phase stabilities and mechanical properties of multicomponent alloys: A comprehensive review for high entropy alloys and compositionally complex alloys, *Mater. Charact.* 147 (2019) 464–511, doi:10.1016/j.matchar.2018.06.019.
- [340] F. Kormann, A.V. Ruban, M.H.F. Sluiter, *Mater. Res. Lett.* 5 (2017) 35–40.
- [341] C. Niu, W. Windl, M. Ghazisaeidi, Multi-cell Monte Carlo relaxation method for predicting phase stability of alloys, *Scr. Mater.* 132 (2017) 9–12, doi:10.1016/j.scriptamat.2017.01.001.
- [342] J. Ding, Q. Yu, M. Asta, R.O. Ritchie, *Proc. Natl. Acad. Sci.* 115 (2018) 8919–8924.
- [343] Q.J. Li, H. Sheng, E. Ma, arXiv:1904.07681v1 (2019).
- [344] S. Mahajan, G.Y. Chin, Formation of deformation twins in FCC crystals, *Acta Metall.* (1973), doi:10.1016/0001-6160(73)90085-0.
- [345] S. Kibey, J.B. Liu, D.D. Johnson, H. Sehitoglu, Predicting twinning stress in FCC metals: Linking twin-energy pathways to twin nucleation, *Acta Mater.* 55 (2007) 6843–6851, doi:10.1016/j.actamat.2007.08.042.
- [346] M. Ghazisaeidi, L.G. Hector, W.A. Curtin, Solute strengthening of twinning dislocations in Mg alloys, *Acta Mater.* 80 (2014) 278–287, doi:10.1016/j.actamat.2014.07.045.
- [347] C. Niu, C.R. LaRosa, J. Miao, M.J. Mills, M. Ghazisaeidi, Magnetically-driven phase transformation strengthening in high entropy alloys, *Nat. Commun.* 9 (2018), doi:10.1038/s41467-018-03846-0.

- [348] J.C. Crone, P.W. Chung, K.W. Leiter, J. Knap, S. Aubry, G. Hommes, A. Arsenlis, A multiply parallel implementation of finite element-based discrete dislocation dynamics for arbitrary geometries, *Model. Simul. Mater. Sci. Eng.* 22 (2014), doi:[10.1088/0965-0393/22/3/035014](https://doi.org/10.1088/0965-0393/22/3/035014).
- [349] C. Shin, M. Fivel, W.W. Kim, Three-dimensional computation of the interaction between a straight dislocation line and a particle, *Model. Simul. Mater. Sci. Eng.* (2005), doi:[10.1088/0965-0393/13/7/011](https://doi.org/10.1088/0965-0393/13/7/011).
- [350] Y. Zhao, J. Marian, Direct prediction of the solute softening-to-hardening transition in W-Re alloys using stochastic simulations of screw dislocation motion, *Model. Simul. Mater. Sci. Eng.* (2018), doi:[10.1088/1361-651X/aaaecf](https://doi.org/10.1088/1361-651X/aaaecf).
- [351] W.G. Nöhring, W.A. Curtin, Dislocation cross-slip in FCC solid solution alloys, *Acta Mater.* 128 (2017) 135–148, doi:[10.1016/j.actamat.2017.02.027](https://doi.org/10.1016/j.actamat.2017.02.027).
- [352] F. Appel, J.D.H. Paul, M. Oehring, *Gamma Titanium Aluminide Alloys* (2011).
- [353] M. Peters, C. Leyens, *Titanium and Titanium Alloys*, Wiley, 2003.
- [354] B. Yin, F. Maresca, W.A. Curtin, Vanadium is an optimal element for strengthening in both fcc and bcc high-entropy alloys (2020) Under review.
- [355] G. Bonny, D. Terentyev, R.C. Pasianot, S. Ponce, S. Bakaev, Interatomic potential to study plasticity in stainless steels: the fenir model alloy, *Model. Simul. Mater. Sci. Eng.* 19, doi:[10.1088/0965-0393/19/8/085008](https://doi.org/10.1088/0965-0393/19/8/085008).